Microfluidic Approaches to the Synthesis of Complex Polymeric Particles

by

Dhananjay Dendukuri

B.Tech Chemical Engineering, Indian Institute of Technology, Madras (1999),
M.A.Sc. Chemical Engineering, University of Toronto (2001),
M.Eng. Chemical Engineering Practice, Massachusetts Institute of Technology (2004).

Submitted to the Department of Chemical Engineering
in partial fulfillment of the requirements for the degree of

Doctor of Philosophy in Chemical Engineering

at the

MASSACHUSETTS INSTITUTE OF TECHNOLOGY

June 2007

Author _____
Department of Chemical Engineering
May 21, 2007

Certified by _____
Patrick S. Doyle
Doherty Associate Professor of Chemical Engineering
Thesis Supervisor

Certified by _____
T. Alan Hatton
Ralph Landau Professor of Chemical Engineering
Thesis Supervisor

Accepted by _____
William M. Deen
Chairman, Department Committee on Graduate Students

Microfluidic Approaches to the Synthesis of Complex Polymeric Particles

by
Dhananjay Dendukuri

Submitted to the Department of Chemical Engineering
on May 21, 2007, in partial fulfillment of the
requirements for the degree of
Doctor of Philosophy in Chemical Engineering

Abstract

The synthesis of micron-sized polymeric particles with precise control over shape, monodispersity and chemistry is a technologically important objective. Varied applications including medical diagnostics, designer fabrics and optical devices could benefit from the availability of geometrically complex and chemically inhomogeneous particles. Microfluidics has recently emerged as an important alternative route to the synthesis of such complex particles. This thesis presents three new approaches to complex particle and structure synthesis in microfluidic devices.

In the first approach, droplets formed by shearing a curable photopolymer, using a continuous water phase at a T-junction, were constrained to adopt non-spherical shapes by confining them using appropriate microchannel geometries. The non-spherical shapes formed were permanently preserved by photopolymerizing the constrained droplets *in situ* using focused ultraviolet (UV) light from an inverted microscope.

The second and more general method called Continuous Flow Lithography (CFL) is a one-phase, projection photolithography based process to continuously synthesize polymeric microparticles in any 2-D extruded shape down to the colloidal length scale. Polymerization was also performed across laminar, co-flowing streams to generate Janus particles containing different chemistries, whose relative proportions could be tuned easily. CFL was also used to synthesize 'particle surfactants' that assembled at the interface of oil-water emulsions or formed micelle-like structures in water. While CFL was able to synthesize particles in non-spherical shapes with chemical anisotropy, particle throughput and resolution was a concern. To mitigate these problems, a new setup called Stop Flow Lithography (SFL) was devised. In SFL, a flowing stream of oligomer is stopped before polymerizing an array of particles into it, providing for much improved resolution over particles synthesized in flow. The formed particles are then flushed out at high flow rates before the cycle of stop-polymerize-flow is repeated. The high flow rates enable orders-of-magnitude improvements in particle throughput over CFL. However, the deformation of the PDMS elastomer due to the imposed pressure restricts how quickly the flow can be stopped before each polymerization event. We have developed a simple model that captures the dependence of the time required to stop the flow on geometric parameters such as the height, length and width of the microchannel, as well as on the externally imposed pressure.

A third approach to synthesizing particles uses elastomeric phase masks to build all-PDMS devices. Coherent laser light passing through a phase mask generates a complex 3D distribution of intensity that selectively exposes certain regions while leaving out others. This results in the formation of 3-D structures whose features can be tuned at the micron scale and below. We

have attempted the formation of 3-D structures in hydrogel polymers which could have important implications in the field of tissue engineering.

Finally, we have developed a simple model of the oxygen inhibited polymerization that occurs in flow lithography. This model is able to qualitatively predict the presence of a thin, uncrosslinked layer of oligomer close to the walls of the PDMS device. This layer is critical to our ability to flow out particles in flow lithography. This thesis demonstrates that microfluidics is indeed a viable and promising route to the synthesis of complex polymeric particles and structures.

Thesis Supervisor: Patrick S. Doyle
Title: Doherty Associate Professor of Chemical Engineering

Thesis Supervisor: T.Alan Hatton
Title: Ralph Landau Professor of Chemical Engineering

Acknowledgements

My very sincere thanks to Pat Doyle and Alan Hatton for negotiating me most ably through my PhD. Pat - you have been an advisor in the true sense of the word. I am extremely grateful for your scientific vision, for always 'being there' and for making me think more deeply about varied scientific issues through the course of my thesis. I am positive my PhD experience will last me in good stead for the future. Alan - thanks for the tremendous support and the ever cheerful smile with which you have welcomed me to your office. You were very positive and encouraging when things weren't going well. Your scientific input at various points was always useful. I am grateful to my committee members - Gareth McKinley, Paula Hammond and Alice Gast for insightful comments and suggestions. The Doyle and Hatton groups have constantly supported and entertained me as required - the latter being as important as the former when you spend five years doing your PhD. Greg Randall - thank you for helping me get started in the lab and for interesting discussions on science and sandwiches. Thierry Savin - thanks for help with several microscopy and software issues over the years. Pat Underhill - I will always cherish the long discussions on various aspects of physics that you so cheerfully had with me. The gain was all mine. Ramin Haghgooie- your support on so many issues ranging from Latex to PDMS is much appreciated. I know you lent me a helpful ear innumerable times even though you were busy with your own work. Dan Pregibon - its been a true pleasure working together on so many projects together. Your creativity and engineering skills will always inspire me. Anthony Balducci - thanks for entertaining several of my questions over the years and never once being annoyed. Ju Min - thanks for the help with modeling,

introduction to Korean food and always providing us with something to talk about. There was not a boring moment with you around. Aruna - my gratitude for several illuminating discussions over the years. Brad Cicciarelli was an excellent companion when we travelled to several conferences together and helped me with surface energy measurements. Harpreet Singh initiated me into the experimental side of magnetic fluids for which I am grateful. Lev Bromberg also helped out in the initial search for suitable photosensitive polymers. Ji-hyun Jang, Yuhua Hu, Mats Cooper and Steve Kooi provided technical support at different points during my work. I also had the great pleasure of working with three very talented UROPS - Kim Tsoi, Jesse Collins and Shelley Gu. They were all efficient and productive and I hope it was a gainful learning experience for them. Outside the lab, my life at MIT was enriched by several people among whom I must mention my classmates and friends-in-arms Neil Kumar and Brian Stephenson. Thanks guys for all the endlessly interesting lunch discussions and movie outings together. I will definitely miss the good times. Mithila was an unflinching source of support, advice and good food when required. Others who have made my life at MIT easier include Vikram Sivakumar. Outside MIT my thanks go to my violin *guru* KVS Vinay and house-mates Maggie Benthall and Itamar Shtull-Trauring for putting up with me. Amma, Nanna, Akka and Harold - you have always been there for me and constantly encouraged me to aim high. For this, I cannot thank you enough.

Table of Contents

List of Figures

List of Tables

CHAPTER 1

Introduction

1.1 Microfluidics

Research in microfluidics and microfluidic technologies has grown exponentially over the past decade (Figure 1.1). So what is microfluidics and why is it useful? Simply put, microfluidics refers to the devices and plumbing that enable the precise manipulation and flow of small volumes of fluid [1,2]. Given this rather loose definition, microfluidics has a long history that pre-dates the current spotlight the field enjoys. However, the impetus for rapid growth in the field has been provided by the pressing need to automate biology and chemistry. While automation and miniaturization applications have received wide attention, there have been several tangential benefits to microfluidics research that have come to the fore more recently. This thesis deals with one such topic - the use of microfluidics to synthesize complex polymeric particles and structures. While methods for the synthesis of inorganic particles and structures using microfluidics [3] have also received wide attention in the literature, such methods are not alluded to as they fall out of the scope of this thesis.

1.2 Polymeric Particles

Polymeric particles (Figure 1.2b), as referred to in this thesis, are solid, polymolecular objects that vary in size from 10 nm to 1mm. Such particles are dispersed in solvent and have a number of important uses.

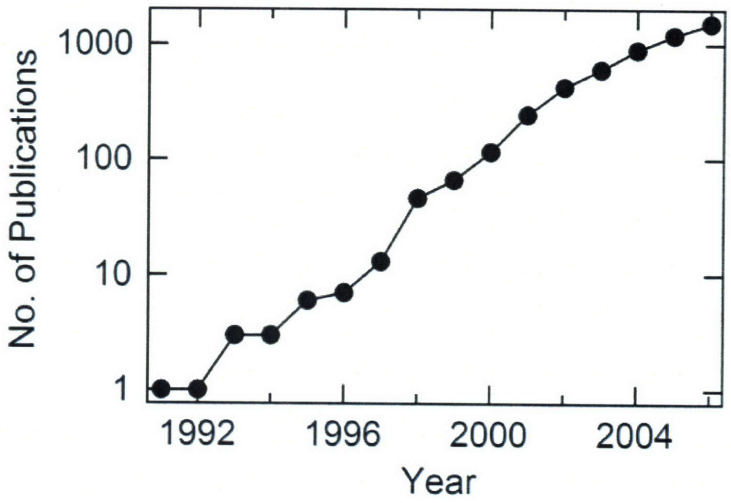

Fig. 1.1: *Plot showing the growth of work in the area of microfluidics as measured by the number of publications using the key work search 'microfluidic*' in ISI Web of Science.*

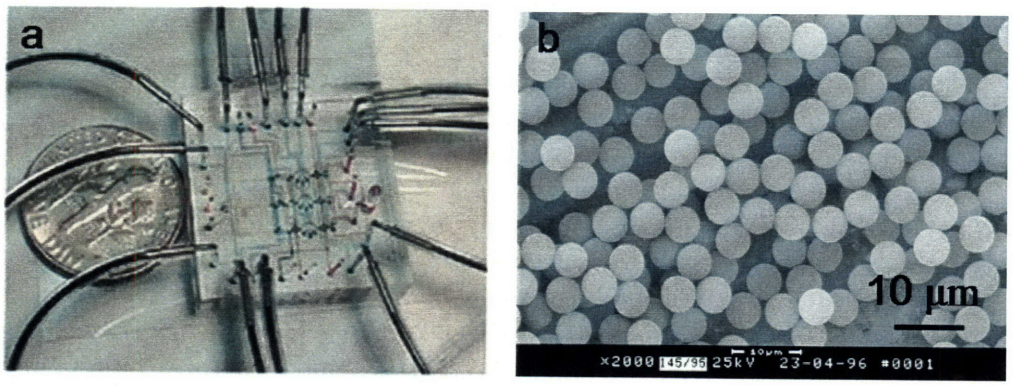

Fig. 1.2: *The two themes that run through this thesis. a)An example of a PDMS microfluidic device (reproduced from [4]). A dime is shown to convey the small scale of the device. b)SEM image of a collection of micron sized polymeric particles (reproduced from http://www.microparticles.de).*

1.2.1 Industrial Applications

Polymeric particles find application in protecting metal, wood and leather against water and microorganisms, are used as binders for pigments, fillers and fibers and to finish the surfaces of metal, wood or paper [5]. In most such applications, an aqueous suspension of polymeric particles is applied on a surface and left to dry creating a coating of functional polymer. In the area of solid plastic materials, dispersions of particles are used as impact modifiers while such materials as gloves and latex foams for mattresses are derived directly from the dispersions. Besides their bulk uses, a variety of niche biotechnological applications are proving to be an important driver for the growth of polymeric particles. In such applications, small volumes of particles that have been functionalized with a specific biomolecule have been used for applications in drug delivery and medical diagnostics [6]. More recently, the self-organization with three-dimensional (3D) periodicity of particles on the scale of optical wavelengths has attracted attention as a promising route to 3D photonic band gap (PBG) materials [7]. PBG materials are opaque to specific wavelengths of light and could prove to be extremely useful in the construction of optical devices and circuits.

1.2.2 Fundamental Research

In physics, colloidal dispersions of polymeric particles function as a model system for atoms [8]. Many of the fundamental forces that govern the assembly and structure of materials from their atomic or molecular building blocks are important at the colloidal length scale ($\leq 1\mu m$) also. Studying these forces at the colloidal length scale permits the visualization of phenomena such as phase transitions using optical microscopy. Further, these experiments can be performed at practically accessible timescales [9].

The rheology of particle suspensions is of great importance to many industrial applications [10]. Rheology is the study of how materials flow and the characterizing the flow of suspensions is essential to the processing of foods, the smooth running of automotive equipment, flow of paints and many others applications. The first step towards characterizing complex industrial suspensions is to develop theories for model suspensions of particles whose morphology and properties are well known. In such studies, it would be therefore be extremely useful to be able to access polymeric particles whose shape, size and chemistry can be finely controlled.

1.2.3 Need for Complex Particles

Most of the applications outlined so far - whether industrial or fundamental - have made use of spherical polymeric particles. The primary reason being that such particles are easy to make because the minimization of surface energy during most syntheses leads to the formation of spheres. In a variety of industrial applications, spherical particles are in fact desirable and necessary besides the fact that they are available cheaply and are easy to make.

However, for a growing number of applications, control over particle morphology and chemical anisotropy is becoming necessary. In fundamental studies, for example, non-spherical or 'patchy particles' can assemble into a much richer variety (Figure 1.3) of structures than spherical particles [7, 11, 12]. In the bottom-up approach envisioned to build materials and devices of the future efficiently, [12] one would like to pre-program the structure or bulk properties of supra-particular assemblies through precisely designed building blocks. The specific interactions caused by the geometrical anisotropy and chemical inhomogeneity of the building blocks are then vital to their

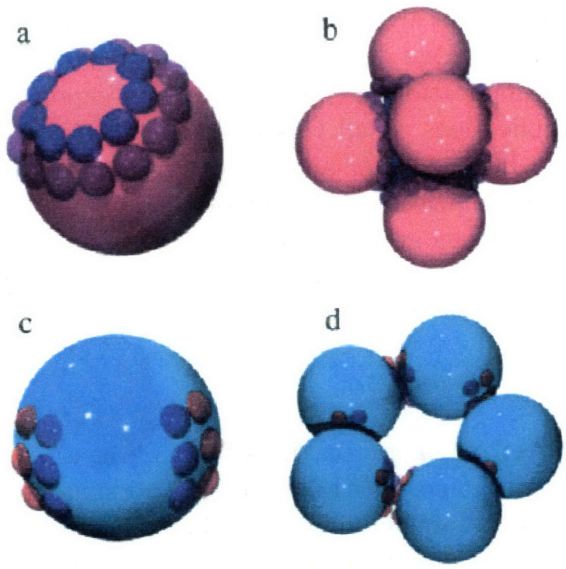

Fig. 1.3: *Anisotropically interacting particles and their assembly predicted by computer simulations (reproduced from [11]). a)Spherical particles with two rings of sticky patches that interact attractively with like patches on other particles. Here, blue patches interact via a LJ potential, red patches interact via a LJ potential, and red patches interact with blue patches via a soft-sphere excluded volume repulsive interaction. b)Square pyramid structure assembled on cooling from six particles as in a). Structure shown is taken from a larger simulation that includes many such structures formed from hundreds of particles. By changing the angle of the patches below the equatorial plane, other polyhedra, such as tetrahedra and icosahedra are obtained. c)Spherical particle with sticky patches that interact attractively with like patches on other particles. The interactions are the same as in a). d)Ring assembled on cooling from five particles as in c). Structure shown is taken from a larger simulation that includes many such structures formed from hundreds of particles. By changing the angle between the patches, rings of larger and smaller diameter may be obtained via self-assembly.*

assembly and the macroscopic properties of the superstructures formed. In suspension rheology, the effect of particle shape on rheological behavior is very important. The existence of model suspensions of non-spherical colloids would greatly assist such studies [10].

From a technological standpoint, particles with custom designed shapes and chemical anisotropy could pave the way for new, hitherto unexplored applications. For instance, our group has developed a disruptive new technology for the multiplexed sensing of DNA using a particle based assay [13]. By using the flow lithography technique discussed later in this thesis (Chapter 3), particles with up to a million unique graphical signatures and two or more distinct sections were created to accomplish the multiplexed sensing of DNA oligonucleotides in solution. Others have shown that the shape of polymeric particles determines the efficiency of their uptake in phagocytosis [14]. This could have important implications in both immunology and the field of drug delivery where efficient uptake of the particle carrier is an important concern.

1.3 Standard Methods to Make Polymeric Particles

Most of the applications detailed thus far require particles with well-defined particle characteristics such as particle size, porosity and surface charge. To achieve reproducible results, uniform particle size and shape are required to provide consistent and uniform physical and chemical properties. A very narrow distribution in particle size and shape results in constant and predictable responses to external electromagnetic fields or constant reaction kinetics between functionalized particles and the desired molecules in solution. The most popular approach to making polymer particles are suspension and emulsion polymerization.

1.3.1 Suspension Polymerization

In suspension polymerization,the initiator is soluble in the monomer, and these two are insoluble in the polymerization medium. The monomer phase is suspended in the medium in the form of small droplets using a suspension stabilizer. The polymerization is then initiated at the desired temperature (20-100 °C). Under these conditions, the monomer microdroplets are converted directly to the corresponding polymer microspheres of approximately the same size. As shown later in this thesis (Chapter 2), the controllable break-off of droplets in a microfluidic device can be used to create very monodisperse droplets of monomers.

1.3.2 Emulsion Polymerization

Unlike suspension polymerization, in an emulsion polymerization process, the initiator is insoluble in the monomer but soluble in the polymerization medium. The monomer is present in the form of droplets and emulsified by surfactant. Since the initiator is present only in the medium, the initial nucleus of polymerization is also in the medium (i.e. outside the droplets). These loci are then gradually surrounded by monomer from the emulsion droplets to form stabilized nuclei. Subsequently, emulsifier-stabilized polymer nuclei become the main loci of polymerization by absorbing further monomer molecules from the medium. In this way, the particles grow gradually until the monomer is completely consumed. The size of particles produced is usually in the range 50-300 nm.

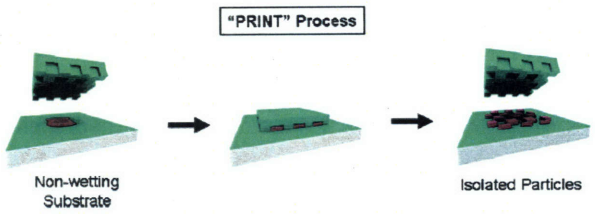

Fig. 1.4: *The PRINT method for particle formation. Particles are formed in a non-stick mold before being released by peeling off the mold from a non-stick surface.*

1.4 Specialized Methods for Complex Particles

While suspension and emulsion polymerization are convenient for the production of spherical particles and some limited classes of non-spherical shapes [15], they do not offer the control required to synthesize particles with custom-designed shapes or tunable chemical anisotropy. As a result, several other approaches have been proposed for such specialized particle syntheses.

1.4.1 Template-Based Methods for Non-Spherical Particles

A general approach to the synthesis of complex shapes is to first create an appropriate mold that serves as a template for particle formation. The mold is then filled with a monomeric liquid before particles are solidified and then released. An example is the versatile PRINT© process [16] which involves the use of a 'non-stick' fluoropolymer mold (Figure 1.4). Oligomeric liquid enclosed within the mold is cured using UV light before the mold is peeled off to release the individual particles. Several classes of non-spherical shapes down to 200 nm have been successfully created using this method. The authors have also demonstrated that the particles can be loaded with various biomolecules for applications in drug delivery. Another example of such a process is the 'lost wax' method [17] that has been used to create a variety of non-spherical particles using macroporous polymer templates constructed from a silica colloidal crystal.

1.4.2 Interfacial Methods for Anisotropic Particles

While non-spherical particles have been created using some of the template-based methods described so far, chemical anisotropy is not trivially achieved. As discussed earlier, particles with controlled chemical anisotropy are particularly interesting as building blocks for more complex structures. Such work has attracted a lot of attention for the past two decades and a large body of work on making 'patchy' particles now exists [18]. Most such methods start with pre-made particles that are then treated to controlled surface patchiness. The most common method that is used to obtain patchiness is by first absorbing particles at the interface of an emulsion droplet [19] and then selectively modifying the surface of the particle. While shape selectivity of particles is not obtained, some control over 'patchiness' is possible by altering the interfacial properties of the phase involved. However it is not easy to tune chemical anisotropy in these processes nor can more

than two functionalities be added easily.

1.4.3 Miscellaneous Techniques for Complex Particles

Besides the methods mentioned, others have used the anisotropic deformation of some substances under the presence of external radiation to create ellipsoidal particles [20]. Among other methods used for the synthesis of complex particles are electrical [21, 22] or surface-force driven [23] microdroplet manipulation techniques to synthesize topologically complex spherical droplets. Recently, interference lithography, has also been proposed as a route to the synthesis of 3-d, non-spherical structures at the sub-micron scale [24]. It is still not clear exactly what shapes or what classes of shapes are possible using such techniques. While non-spherical shapes have also been synthesized using multi-layer photolithography [25] and manual fabrication [26], it is difficult to use these methods to synthesize particles with more than two chemistries or finely tune the extent of each chemistry in the particle. There is therefore a distinct need for a single-step particle synthesis method to form different non-spherical shapes with tunable anisotropy and with the ability to incorporate more than two chemical functionalities.

1.5 Microfluidic Techniques for Particle Synthesis

Despite the existence of several successful methods to make polymeric particles as detailed thus far, there still exists a significant lack of capability to make large numbers of generalized complex particles. In the past few years, several new microfluidic approaches have been proposed to address the challenge of synthesizing complex particles [27]. While the particle throughput that can be achieved using microfluidics is still not comparable to techniques like emulsion polymerization, it is expected that such methods will well serve niche, value-added applications in the coming years.

1.5.1 Device Construction using Soft Lithography

The common thread that binds disparate microfluidic technologies is the ability to use microfabrication techniques to build devices at the millimeter scale and below. A variety of fabrication techniques have been borrowed directly from the IC industry but the widespread use of microfluidics in academic laboratories can be attributed to the invention of soft lithography [28]. While 'hard' devices built out of silicon must be microfabricated sequentially using expensive fabrication facilities, soft lithography has enabled the rapid and cheap production of devices using elastomeric materials. The Whitesides group at Harvard University has popularized the use of poly(dimethylsiloxane), commonly known by the abbreviation PDMS, as the material of choice for microfluidic applications. PDMS soft lithography (Figure 1.5) is ideally suited for the rapid and cheap production of microfluidic devices.

1.5.2 Suitability for Particle Synthesis

Microfluidics offers a convenient and finely controllable route to synthesizing non-spherical microparticles with the twin advantages of using soft lithography to design geometries at the micron length scale and of having the ability to exploit fluid mechanics to tune particle morphology. Geometric confinement at the micron length scale can allow for the synthesis of micron sized particles using microfluidics as seen in our own work (Chapter 2). The complex patterns obtained as a result

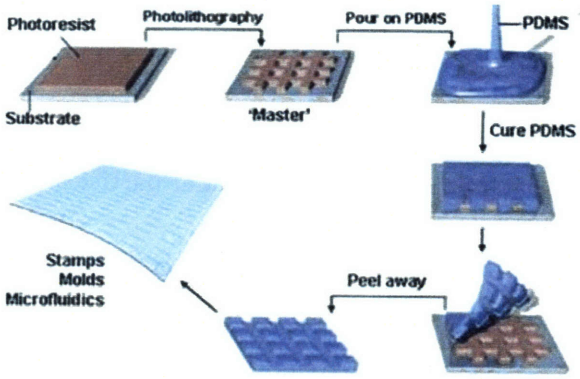

Fig. 1.5: *Schematic showing the soft lithography process. A silicon master is first created using a suitable photoresist. Liquid PDMS is poured on the master, cured at high temperature and then peeled off to repeatedly form microfluidic devices.*

of the instability and non-linearity in two-phase flow [29] are an example of how fluid mechanics can be exploited to create novel shapes that are very difficult to create using the methods described so far. When using microfluidic synthesis, particle size can be tuned continuously by modifying the flow parameters in the microfluidic channel. Furthermore, the particle surface properties can be modified after formation by using the layer-by-layer technique [30].

In addition, PDMS itself has many properties that lend themselves to the synthesis of particles. PDMS is cheap, transparent, conductive, has a low surface energy and is porous. The last mentioned advantage has been exploited for biological applications where the transport of oxygen through PDMS is essential to keep cells alive. We have exploited this property of PDMS to synthesize particles in a continuous fashion in a microfluidic device (Chapter 3).

1.6 Previous Microfluidics Work

Over the past five years, several microfluidic approaches to particle synthesis have been proposed [31–39].They can be broadly classified into multi-phase approaches that involve the formation of droplets [31, 34–36] and one-phase approaches [33, 38].

1.6.1 Droplet Based Particle Synthesis

The subject of droplet formation in microfluidics has received a tremendous amount of attention recently [40]. Briefly, large numbers of monodisperse droplets on the micron scale are created by breaking off droplets of a dispersed phase using the confining effects of a T-junction geometry [41] or the extensional flow created in a flow focusing device [42]. In addition to being a route to introducing non-linearity into microflows [29], droplets are being used to perform combinatorial screens to optimize conditions for protein crystallization [43], and for a variety of other applications in high throughput biology [44].

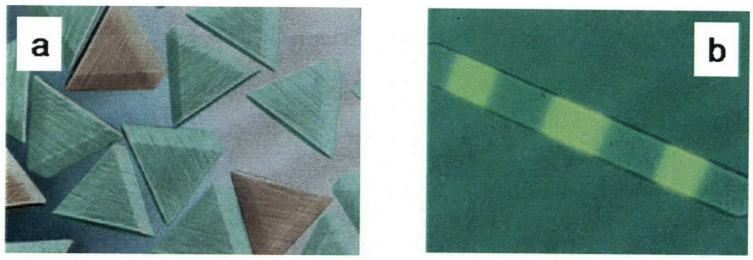

Fig. 1.6: *Complex particles synthesized using methods described in this thesis. a)Artificially colored triangles synthesized using Continuous Flow Lithography (CFL). This is an example of complexity in particle shape. b)Chemically inhomogeneous particles synthesized using CFL. Image courtesy Daniel Pregibon.*

Droplet formation has also been used as a means to create polymeric microspheres with a narrow size distribution [31,45,46]. Droplets of a dispersed phase that is either a low-melting point lipid [45] or a UV curable polymer [46, 47] are pinched off into a continuous aqueous phase and are then either frozen or polymerized to create solid spheres. Precisely sized solid spheres can be obtained by tuning the flow of the dispersed and continuous phases to form colloids of a desired size. In other work including our own, droplets of polymer precursors have been confined geometrically to form non-spherical shapes [34, 35] Others have reported the microfluidic synthesis of spherical particles with multiple chemistries [39] by coflowing multiple laminar streams before breaking them off and crosslinking the resulting multifunctional droplets.

Droplet based synthesis in microfluidic devices has introduced a new paradigm and grown into a field on its own, as witnessed by the spurt in publications in this area. However, there are significant limitations in the morphologies and sizes that can be created. The shapes formed are limited to being deformations of spheres (rods, ellipsoids etc.) because they start from a precursor spherical droplet. Further the size of the droplets is dependent on the device geometry which limits the smallest size of particles to around 10 μm using currently available soft lithographic techniques.

1.6.2 Continuous Flow Methods for Structure Synthesis

The other category of particle synthesis using microfluidics involves the polymerization of one-phase flows. In such a process, light is shone directly on laminar flowing streams of photosensitive oligomer to create strips [33] or arrays of photomask-define individual particles [38].

The mask-based flow lithography approach [38] that we have proposed marks a break with the literature in this area as it allows for particle shape to be conveniently defined using a photomask [48] while allowing for a high degree of chemical anisotropy by polymerizing across multiple laminar streams (Figure 1.6). By using specific polymer chemistries or by loading the polymeric precursors used with liquid crystals, magnetic materials, quantum dots, dyes etc., we can synthesize particles that bear both complex shapes and a specific chemical or physical functionality. This enables the creation of chemically diverse sets of non-spherical particles in an extruded 2D shape [13, 38, 49]. Unlike any of the methods described so far, it also allows for the much more challenging task of

synthesizing chemically inhomogeneous polymeric particles with non-spherical shapes.

1.7 Thesis Organization

This thesis is organized as follows :

1. Chapter 2 describes the use of a two phase approach to synthesize polymeric plugs and disks by geometrically confining droplets of oligomer in a microfluidic channel.
2. Chapter 3 describes the Continuous Flow Lithography (CFL) technique to synthesize complex polymeric particles in any extruded 2-D shape and with tunable chemical anisotropy.
3. Chapter 4 describes how CFL can be used to synthesize amphiphilic particles and also shows the assembly of such particles at interfaces and in bulk.
4. Chapter 5 describes a phase-mask based approach to the continuous synthesis of 3-dimensional structures using microfluidic devices.
5. Chapter 6 details the Stop Flow Lithography (SFL) approach to particle synthesis where particle throughput and resolution are considerably improved over CFL. A model to predict the dynamic response of PDMS to changes in external pressure is also described.
6. Chapter 7 is involved with modeling the oxygen inhibition effect that permits flow lithography to work.
7. Chapter 8 talks about the conclusions from this work and the outlook for the future.
8. Appendix A lists some useful laboratory practices and unreported experiments that have been gleaned from this work.

CHAPTER 2

Two-phase Approach to Non-spherical Particles

2.1 Introduction

As mentioned in Chapter 1, the droplet-based approach to particle synthesis has attracted much attention recently. While previous authors had successfully demonstrated the synthesis of polymeric microspheres [31, 45] with finely controlled sizes, we show, in this chapter, that microfluidics can also be used to controllably synthesize non-spherical particles [34].

Droplets of a UV curable polymer were first formed at a T-junction [41] by shearing the dispersed polymer phase using a continuous, surfactant-containing aqueous phase (Figure 2.1). The droplets formed were confined into plug and disk-like shapes by utilizing suitable microchannel geometries, before the polymer was cured *in situ* using UV light from the objective of the microscope to preserve the non-spherical shapes. Both plugs and disks were created using the basic microchannel geometry illustrated in Figure 2.1a, the only difference between the two channels used being their height, which was 38 μm to form plugs and 16 μm to form disks.

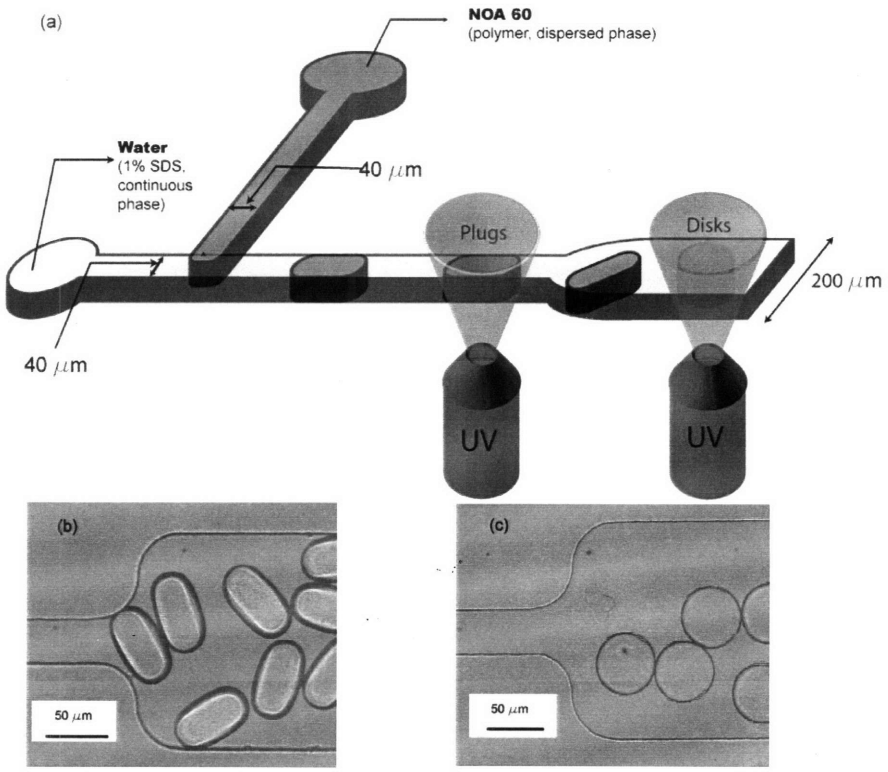

Fig. 2.1: *Microchannel geometry used to create plugs and disks. a) schematic of channel with plug and disk creation zones marked. b) polymerized plugs in the 200 μm section of the channel, 38 μm height. c) polymerized disks in the 200 μm section of the channel, 16 μm height.*

2.2 Experimental Methods

2.2.1 Microfluidic Devices

Microfluidic channels were fabricated by pouring polydimethoxysilane (PDMS, Sylgard 184, Dow Corning) on a silicon wafer containing positive-relief channels patterned in SU-8 photoresist (Microchem). The channel dimensions are shown in Figure 2.1a. Channels of two different heights were used - 38 μm to create plugs and 16 μm to create disks. The microdevices were sealed to glass slides using a PDC-32G plasma sterilizer (Harrick).

2.2.2 Flow and Photopolymerization

Syringe pumps (KDS 100, KD Scientific) were used to adjust the flow rates of the two phases. Both aqueous and polymer solutions were infused into the channels using 50 or 100 μl Hamilton Gastight syringes (1700 series, TLL). The continuous phase was a 1% SDS solution that had been pre-filtered using a 0.2 μm filter. The viscosity of the SDS solution (μ = 1.08 mPa s) was measured using a glass capillary viscometer (Technical Glass Products). Norland Optical Adhesive 60 (NOA 60, Norland Products, μ = 300 mPa s) a UV-sensitive liquid photopolymer that cures when exposed to UV light was used as the dispersed phase. An energy flux of 3 J/cm2 was required for a full cure. The formation of the microparticles was visualized using a CCD camera (KPM1A, Hitachi) mounted on an inverted microscope (Axiovert 200, Zeiss). Images were captured and processed using NIH Image software. Plug length calculations were performed in NIH Image by measuring the longest observable dimension of the plug. A 100W HBO mercury lamp served as the energy source. A UV filter set that provides wide UV excitation (11000v2: UV, Chroma) was used to generate light of the desired wavelength. The interfacial tension between the SDS solution and the polymer was measured to be 6.64 mN/m by the pendant drop method using a DSA10 Tensiometer (Kruss).

2.3 Results

The break-off of droplets at a T-junction is governed by the competition between viscous stress and surface tension. The Capillary number $Ca = \mu v_c w/\gamma$, is a measure of the relative importance of these two effects where μ is the viscosity of the continuous phase, v_c is the superficial velocity of the continuous phase and γ is the interfacial tension between the continuous and the dispersed phases. The droplet size obtained at the T-junction can be tuned by modifying Ca [29].

2.3.1 Phase Diagram for Droplet Breakoff

In our system, Ca can be modified by changing Qc, the flow rate of the continuous phase, which leads to a change in v_c through $v_c = Q_c/A$, where A is the area of cross-section of the microchannel. As Ca increases, the shear forces increase in comparison to the surface tension forces, leading to the formation of smaller droplets.

In addition to Ca, the flow rate of the dispersed phase Q_d (and hence the velocity of the dispersed phase, $v_d = Q_d/A$), can also be used to tune droplet size for droplet break-off at a T-junction. As Q_d increases at a constant value of Ca, droplets of larger size are formed. Previous work on droplet breakoff in microfluidics has used a phase diagram to represent the different regimes observed, as

a function of experimental parameters [29, 42]. Using a similar approach, we plotted the phase behavior of our system in $Ca - Q_d$ coordinates. As shown in Figure 2.2, we have classified the system into three phases - the wetting phase (I), the plug phase (II) and the droplet (III) phase.

The wetting phase is characterized by the polymer flowing as one phase through the channel and occurs at very low Ca when the shear forces are not sufficiently large to cause the polymer phase to pinch off at the T-junction. As Ca is gradually increased at a constant Q_d, a critical capillary number (Ca_{w-p}) is reached where plugs of polymer begin to pinch-off at the T-junction. This represents the transition from the wetting phase to the plug phase. For $Ca > Ca_{w-p}$, the dispersed phase starts breaking off at the T-junction and at these still relatively low values of Ca, the diameter of the resulting droplets is larger than the width of the channels leading to plugs rather than droplets being cleaved off. As Ca is further increased, plugs of progressively decreasing length are formed, leading eventually to the formation of droplets ($L < 38\mu m$). The droplet phase is thus an extension of the plug phase, but is classified separately because we are interested in the formation of non-spherical shapes. This transition to the droplet phase (Ca_{p-d}) occurs at values of Ca that are one or two orders of magnitude larger than the Ca_{w-p} at the same Q_d. As is intuitively expected, both Ca_{w-p} and Ca_{p-d} increase with increasing Q_d. The phase plot shown in Figure 2.2 is a useful engineering tool to define the operating regimes of the microfluidic device.

2.3.2 Plug Length

Plug length, L_p, was controlled by changing Ca and Q_d. Plug lengths are non-dimensionalized using the width of the channel and are given by $\tilde{L_p} = L_p/40\mu m$. As Ca is increased within the plug phase at a given Q_d, plugs of decreasing length, L_p, are observed (Figure 2.3) until the length of the plugs equals the width of the channel, signaling the onset of the droplet phase. The plug length drops very gradually at $Ca > 0.001$ and thus only the range of Ca where a significant drop in plug length is seen has been shown in Figure 2.3. Plug length can also be modified by changing Q_d. For a given value of Ca, a higher Q_d leads to a larger plug length. In all cases, the plug lengths obtained had a standard deviation of less than 5%.

For a given Q_d, the plugs of the greatest length were observed at low values of Ca just when the transition from wetting to the plug phase occurs. Due to the non-steady motion of the syringe pump at low flow rates, the region where extremely long plugs are obtained could not be probed in depth.

2.3.3 New Plug Length Analysis

Since the publishing of our paper [34], the problem of droplet formation in T-junctions has been studied in more detail [50]. The authors find that in conditions where $Ca \ll 1$, droplets pinch off mainly because of pressure gradients created across their length due to the confinement of the continuous phase to a thin film surrounding the droplet. Thus droplet breakoff under these conditions is governed by geometric confinement and not by shear forces imposed at the T-junction. The length of plugs formed at a T-junction is only dependent on the ratio of the flow rates of the two phases and is given by

$$\frac{L_p}{w} = 1 + \frac{Q_d}{Q_c} \tag{2.1}$$

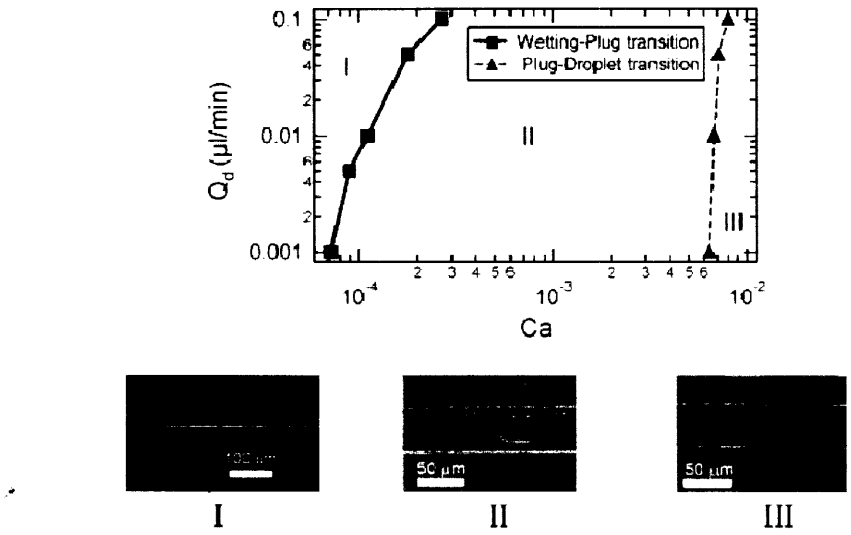

Fig. 2.2: *Phase plot of the system with the three labeled phases shown: (I) wetting phase (II) plug phase and (III) droplet phase. The wetting-plug transition, which is abrupt, is shown as a solid line. The plug-drop transition, which is more gradual, is shown as a dashed line. The symbols shown on these lines were experimentally obtained by fixing Q_d and gradually increasing Ca until a change of phase was observed. The lines that connect these symbols are drawn to guide the eye. The uncertainty in the location of the transition is comparable to the size of the symbol. Furthermore, the transitions are independent of the experimental path taken (i.e. increasing or decreasing Ca).*

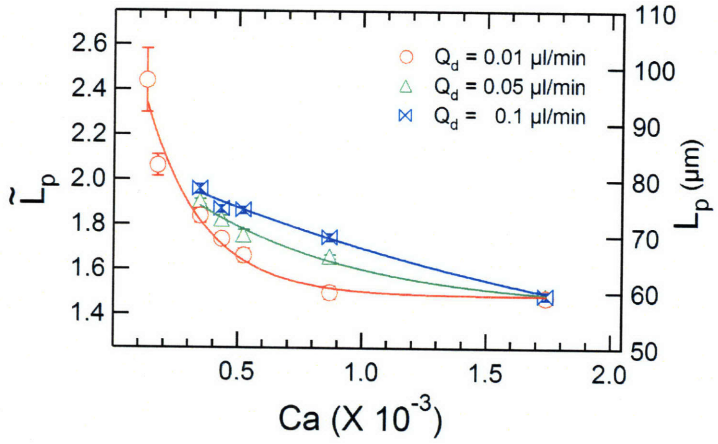

Fig. 2.3: *Plug length plotted as a function of Ca for different values of Q_d. All data were collected from a 38 µm tall channel. On the left axis is plotted the plug length non-dimensionalized using channel width(Lp /40 µm). On the right axis is plotted, the measured plug length, Lp (µm).*

We plotted our data to see if it obeys Equation 2.1 and found modest agreement as seen in Figure 2.4. The model from Equation 2.1 is drawn through the data points.

2.3.4 Polymerization of Plugs

After the plugs were formed, they had to be polymerized before they reached the 200 μm section where they would otherwise relax into a disk like shape. Plugs were polymerized just before they entered the 200 μm section (Figure 2.1a) so that there was the least chance of their blocking the channels. A small layer of lubricating water film around the plug rendered the plug mobile even after it was polymerized [51]. Two of the three dimensions of the plug are dictated by channel geometry - namely the height (38 μm) and the width (40 μm) of the channel. Thus, two of the dimensions of the plug were fixed at 38 μm and 40 μm while the plug length was a function of Ca and Q_d. By choosing an appropriate combination of Ca and Q_d, plugs of a desired length were obtained. The plug seen in Figure 2.5a was obtained at $Q_d = 0.05\ \mu l/\text{min}$ and $Ca = 1.6 \times 10^{-3}$. A collection of plugs is shown in Figure 2.5c. The cured polymer is stable indefinitely [52] and we expect no change in the structure of the plugs obtained after they are formed.

The high energy flux provided from the 20X objective ($\sim 1W/cm^2$) meant that even a small exposure time ($2ms$) was sufficient to polymerize the plugs, given that an energy input of only $3J/cm^2$ is required for a full cure. On the other hand, very long exposure times led to plugs sticking to the PDMS or the glass slide resulting in blockages. The area of focus of the UV lamp and its intensity were progressively reduced from their maximum possible values until polymerized plugs could be obtained steadily in the channel. It was verified that the polymerization of the plugs did not lead to any modification in the dynamics of the system by measuring plug lengths before and after polymerization was initiated. This is most likely due to the fact that the flow rates of

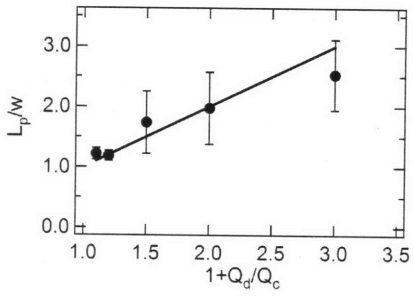

Fig. 2.4: *Plot showing the dependence of plug length on the ratio of flow rates of the dispersed phase and the continuous phase. The data shown were collected for a channel with $h = 38$ μm. Plug length was non-dimensionlized using the width of the channel ($w = 40$ μm). The line drawn through the points is calculated using Equation 2.1.*

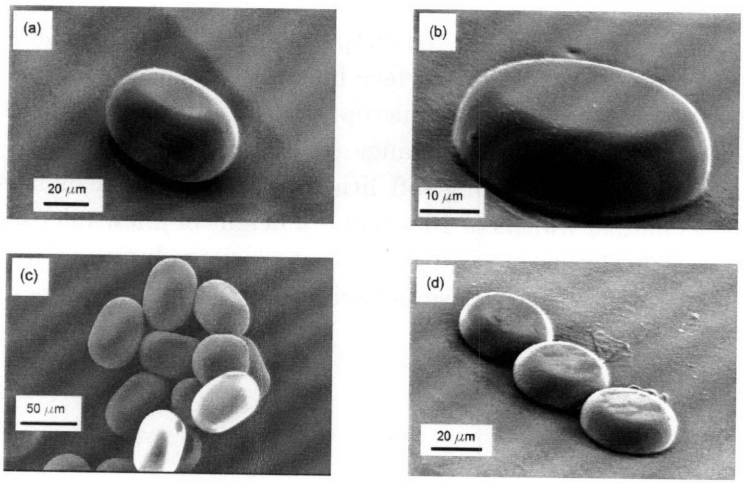

Fig. 2.5: *SEM images of non-spherical particles. a) Plug formed at $Q_d = 0.05$ $\mu l/min$ and $Ca = 1.6 \times 10^{-3}$. b) Disk formed at $Q_d = 0.05$ $\mu l/min$ and $Ca = 4.8 \times 10^{-3}$. c) collection of plugs formed at $Q_d = 0.05$ $\mu l/min$ and $Ca = 1.6 \times 10^{-3}$. d) collection of disks formed at $Q_d = 0.05$ $\mu l/min$ and $Ca = 9.6 \times 10^{-3}$.*

the streams are imposed by the syringe pump, which compensates for pressure variations within the system that may be caused upon curing of the polymer.

Other authors have reported the formation of pear-shaped [53], pearl-necklace [29, 53] and ribbon-shaped [53] objects that could also then be polymerized to synthesize different non-spherical shapes. To show that this method can be extended to create other shapes, we obtained disks by using a channel identical to that used to create plugs, changing only the height of the channel to 16 μm. As shown in Figure 2.5c, disks were obtained by polymerizing plugs that had relaxed into a disk-like configuration in the 200 μm section of the channel. One of these disks is shown in Figure 2.5b while a collection of them is shown in Figure 2.5d. It is noteworthy that there is no visible curvature on the disk surface, leading to microparticles that have a flat surface. The height of the disk seen in Figure 2.5b is 16 μm while the diameter is 40 μm.

2.4 Conclusion

In this chapter, a microfluidic two-phase approach has been demonstrated that offers a convenient route to generate one class of non-spherical microparticles. This process also has the potential to continuously synthesize monodisperse non-spherical particles in a limited class of shapes using a combination of soft lithography and complex pattern formation seen in two-phase flows. As a proof of principle, monodisperse polymeric plugs and disks of different sizes were fabricated. The operational phase space of the microfluidic device was also characterized. Using this method, the material properties of the colloids can be altered by using different photopolymers (e.g. photopolymerizable PEG gels) while size and/or morphology can be adjusted by tuning fluid flow properties or the microchannel geometry. The creation of faceted shapes could allow for surface features that may be useful for fundamental studies on particle-surface interactions and also allow for the creation of designer colloids for special applications. The microparticles synthesized in this study were larger than 10 μm but particles in the colloidal size range ($< 10\mu$m) may be formed by further scaling down the device. For example, using existing soft lithography methods it is feasible to scale down the current device to have channel widths of 10 μm and a height of a few microns. Additional work on scaling up the process will also be needed to generate large volumes of non-spherical colloids that will be needed to characterize their phase behavior and rheological properties.

CHAPTER 3

Continuous Flow Lithography

3.1 Introduction

In the previous chapter, a two-phase approach to the synthesis of non-spherical particles using microfluidics was described. While such a process marks a first step towards achieving complex shapes using microfluidics, it is limited to forming shapes that are either spherical or are elementary deformations of spheres - ellipsoids, rods etc. In this chapter, a much more general approach to particle synthesis called Continuous Flow Lithography (CFL) is described. CFL combines the advantages of microscope projection photolithography [48] and microfluidics to continuously form morphologically complex or multifunctional particles down to the colloidal length scale. Polymerization can also be performed across laminar, co-flowing streams to generate Janus particles containing different chemistries, whose relative proportions are tuned easily. It is a high-throughput technique that offers unprecedented control over particle size, shape and anisotropy.

3.1.1 Limitations of Earlier Methods

In the industrial domain, emulsion polymerization works excellently for the synthesis of spherical particles at the sub-micron scale [5]. However, this process cannot enable precise shape control or enable the tuning of chemical anisotropy of particles. This has led to the development of alternative approaches to particle synthesis. Broadly speaking, such methods have been either template-based batch processes [16, 17, 25, 48, 54] or flow-through microfluidic schemes [31, 33–35, 37, 45] that are

based on two-phase systems. Although, a variety of useful techniques have been developed, all the methods referred to so far have some deficiencies limiting the throughput, shape or functionality of the particles formed.

Work on making particles in microfluidic devices including our own [31,33–35,45] was based on the breakoff of droplets in two phase flows at a T-junction [29,41,47] or in flow-focusing geometries [42]. Due to surface tension effects, such techniques have been restricted to generating particles that are spheres, deformations of spheres [34,35], (rods, ellipsoids or disks) or cylinders [33]. Additionally, these techniques are limited to making one particle at a time and require phase separating chemistries (immiscible fluids) that are also surface compatible with the microfluidic devices used.

Photolithography offers a much more general route to the synthesis of non-spherical particles because of the ability to use photomasks to precisely define shape. However, photolithography has not been used in particle synthesis applications because of the essential batch nature of the process which leads to low particle throughput. In addition, photoresist materials that are used in photolithography are not ideal for applications where biocompatibility or functionalization of the particles is essential. Further, creating chemically anisotropic particles using photolithography requires cumbersome multi-step alignment and protection techniques that are difficult to perform controllably and in a high-throughput fashion.

CFL combines the distinct advantages of microfluidics and projection-photolithography to enable the synthesis of complex polymeric particles [38]. By taking advantage of the higher resolution synthesis and precise shape control intrinsic to photolithography along with the continuous processing capabilities and laminar co-flow properties seen in microfluidic devices, large numbers of monodisperse particles bearing complex shapes and tunable chemical anisotropy were synthesized. In its simplest form, the process requires the use of only one phase, dispensing with the challenge of optimizing device surface chemistry in two-phase flows. Further, by using polymeric precursors with varying chemical properties, one can conveniently functionalize distinct sections of the particles with different chemical properties [13,49].

3.2 Experimental Methods

3.2.1 Materials

All particles shown in this chapter were made using 5% (v/v) solutions of the photoinitiator Darocur 1173 (Sigma Aldrich) initiator in poly(ethylene glycol)(400) diacrylate (PEG-DA, Polysciences). The viscosity of PEG-DA (400) is reported by the supplier to be 57 centipoise at 25°C. We have also made particles composed of trimethylpropane triacrylate, 1,6-hexanediol diacrylate and tri(propylene glycol) diacrylate (all from Polysciences). All these materials belong to the class of multifunctional acrylate molecules that are known to be highly reactive and form tightly cross-linked networks upon radical induced polymerization. The method should work for other radical induced polymerizations since they are in general inhibited by oxygen [55]. 0.005 wt.% solutions of the fluorescent Methacryloxyethyl thiocarbamoyl rhodamine B (Polysciences) in PEG-DA were used to fluorescently label the polymer.

3.2.2 Microfluidic Devices

Devices were fabricated by pouring polydimethylsiloxane (PDMS, Sylgard 184, Dow Corning) on a silicon wafer containing positive-relief channels patterned in SU-8 photoresist (Microchem). The

devices were rectangular channels of varying widths (200, 600 or 1000 μm) and heights (9.6, 20 or 38 μm). These devices were placed on glass slides spin-coated with PDMS to ensure that the oligomer was exposed only to PDMS surfaces. Devices were mounted on an inverted microscope (Axiovert 200, Zeiss) and the formation of the microparticles was visualized using a CCD camera (KPM1A, Hitachi). Images were captured and processed using NIH Image software.

3.2.3 Photopolymerization Setup

Photomasks were designed in AUTOCAD 2005 and printed using a high resolution printer at CAD Art Services (Poway, CA). The mask was then inserted into the field-stop of the microscope. A 100W HBO mercury lamp served as the source of UV light. A filter set that provides wide UV excitation (11000v2: UV, Chroma) was used to select light of the desired wavelength and a VS25 shutter system (Uniblitz) driven by a computer controlled VMM-D1 shutter driver provided specified pulses of UV light. Oligomer solutions were driven through the microfluidic device using a KDS 100 syringe pump (KD Scientific).

3.2.4 Particle Recovery and Characterization

The particles were collected, washed and then re-suspended thrice in ethanol to dissolve the unpolymerized PEG-DA. They were then washed thrice in water and finally suspended in water. The particle size distribution and extent of polymerization were quantified using standard methods

3.3 Description of CFL

In a representative experiment, an acrylate oligomer stream (typically poly(ethylene glycol) diacrylate) containing a photosensitive initiator was passed through a rectangular, all-PDMS microfluidic device as shown in Figure 3.1a. Particle arrays of mask-defined shapes (see squares in Figure 3.1b) were formed by exposing the flowing oligomer to controlled pulses of UV light using an inverted microscope and collected in the device reservoir (Figure 3.1c). Rapid polymerization kinetics permitted the particles to form quickly (< 0.1s) while oxygen-aided inhibition [55] near the PDMS surfaces allowed for particle flow within the unpolymerized oligomer stream.

3.3.1 Movie of Particle Formation

A movie showing the formation of particles is available on the Internet at http://web.mit.edu/ doylegroup/links/ringsmovie.avi. The movie is a real-time video of rows of ring-shaped PEG-DA particles forming and then advecting through unpolymerized PEG-DA in an all-PDMS microfluidic device. The scalebar in the movie is 50 μm.

3.3.2 Particle Morphologies

The shape of the particles in the x-y plane (Figure 3.1) is determined by the shape of the feature used on the transparency mask (Figure 3.1a) while the z-plane projection (shown in Figure 3.1c) is dependent on the height of the channel used and the thickness of the oxygen inhibition layer. Using our microscope projection setup, the transparency feature sizes were reduced by a factor dictated by the objective used, ranging from 7.8 times using a 20$\times$ objective to 39 times using a

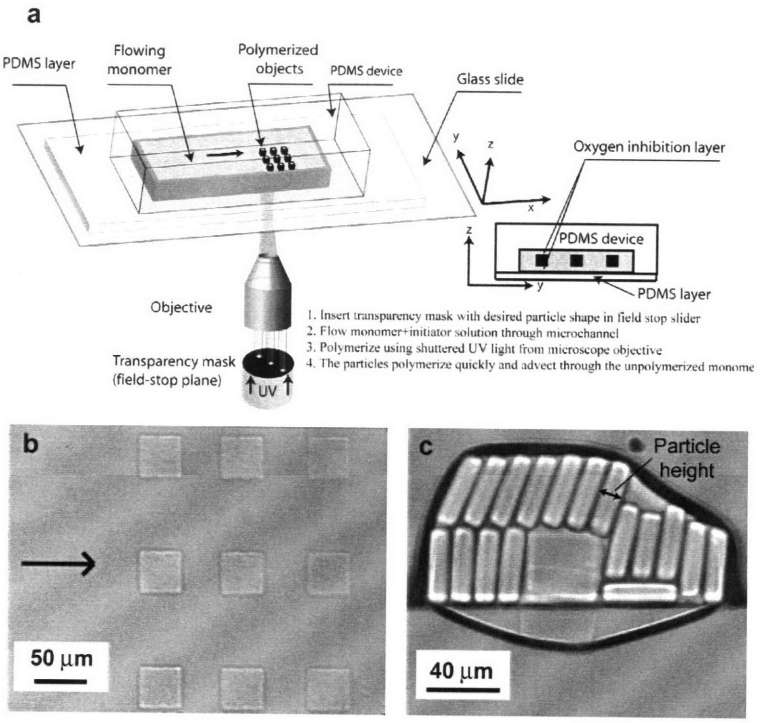

Fig. 3.1: *Experimental setup. a)Schematic depicting the experimental setup used in the study. A mask containing the desired features is inserted in the field-stop plane of the microscope. The monomer stream flows through the all-PDMS device in the direction of the horizontal arrow. Particles are polymerized, by a mask-defined UV light beam emanating from the objective, and then advect within the unpolymerized monomer stream. The side-view of the polymerized particles can be seen in the inset shown on the right. Also shown is the unpolymerized oxygen inhibition layer that allows the particles to flow easily after being formed. b)A bright field microscopy image (xy plane) of an array of cuboids moving through the unpolymerized monomer. c)A cross-sectional view of the cuboids seen in b) upon collection in a droplet that has turned most particles on their sides.*

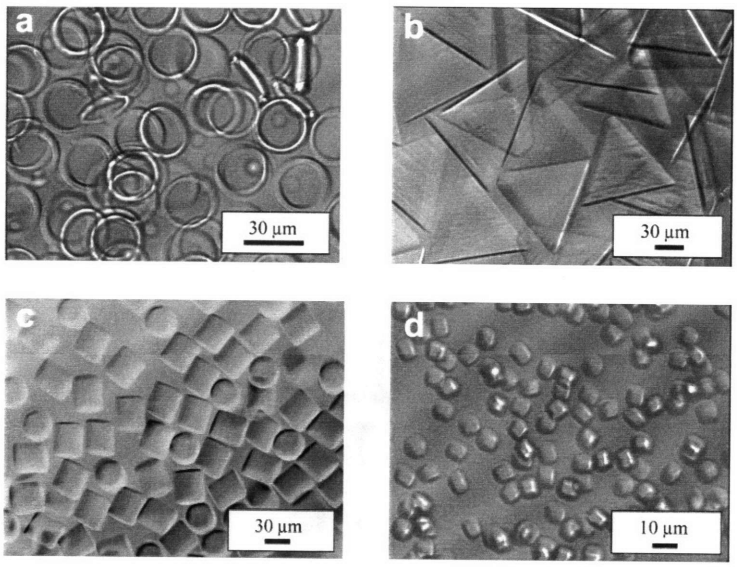

Fig. 3.2: *Differential interference contrast images of collections of particles. Particles were generated in a high-throughput fashion and collected in a reservoir. a)Rings formed using a 9.6 μm high channel and the 20 objective. b)Triangles formed in a 38 μm high channel using a triangular mask and the 20X objective. c) Cylinders were synthesized using circular masks in 38 μm high channels using the 20X objective. d) Colloidal cuboids synthesized using a square mask and the 20X objective in a 9.6 μm high channel. All of the particles were synthesized using exposure times obtained from the data shown in Table 3.2.*

100× objective. For example, using the 20× objective, a 350 μm square mask feature was used to synthesize cuboids (rectangular parallelepiped objects) that had 45 μm sides (350 μm/7.8 = 45 μm) in the x-y plane (Figure 3.1b). The height of the particles was equal to the height of the channel minus the thickness of the inhibition layers.

Cuboids with a height of 15 μm (Figure 3.1c) were synthesized in a 20 μm high channel because of the 2.5 μm thick oxygen inhibition layer at both the top and bottom walls of the device. By designing masks with varied features and selecting channels of differing heights, we synthesized particles of several distinctive shapes, sizes and aspect ratios (Figures 3.2,3.3).

We have synthesized various polygonal shapes such as triangles, squares and hexagons (Figures 3.3a,b,c); colloidal entities (Figure 3.3d); high aspect ratio objects such as posts with circular, triangular and square cross-sections (Figures 3.3e,f); and non-symmetric or curved objects (Figures 3.3g,h,i). All the particles showed good fidelity to the original mask features and had straight sidewalls.

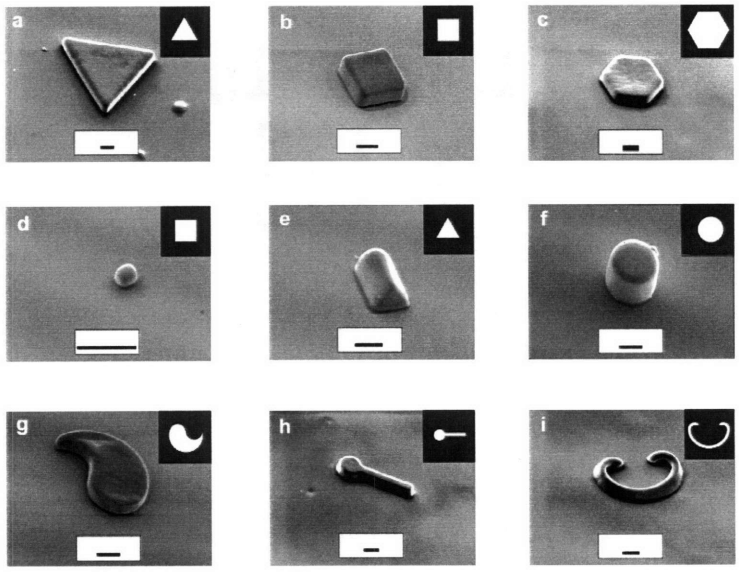

Fig. 3.3: *SEM images of particles. Microparticles formed using a 20X objective (except d) which was formed using a 40X objective) were washed before being observed using SEM. The scale bar in all of the figures is 10 μm. ac) Flat polygonal structures that were formed in a 20 μm high channel. d)A colloidal cuboid that was formed in a 9.6-m-high channel. ef)High-aspect-ratio structures with different cross-sections that were formed in a 38 μm high channel. gi) Curved particles that were all formed in a 20 μm high channel. The inset in the figure shows the transparency mask feature that was used to make the corresponding particle. All of the particles were synthesized using exposure times obtained from the data in Table 3.2.*

3.3.3 Limitations of CFL

The fundamental limitations of a projection photolithography technique, such as ours, are mainly governed by the optical resolution and the depth of field of the microscope objective used. The resolution of an objective is the smallest distinguishable feature that can be discerned and the depth of field is the length over which the beam of light emanating from the objective can be considered to have a constant diameter. In our case, the resolution limits the size of the smallest particle that can be made while the depth of field restricts the length over which the sidewalls will be straight. Better resolution comes at the cost of decreased depth of field. Additionally, practical constraints on particle synthesis are imposed by finite polymerization times and the minimum feature size currently printable on a transparency mask ($\sim$10 μm).

The exposure time required to polymerize particles was inversely proportional to both the height of the channels used and the size of the transparency mask feature; particles required longer polymerization doses when either of these two parameters was decreased. The oxygen inhibition layer thickness is independent of channel height, leading to more pronounced effects in low-height channels, where the layer occupies a larger fraction of the channel height. Smaller transparency feature sizes require increased polymerization doses as a result of diffraction induced limitations in the internal microscope optics. Longer polymerization times lead to constraints on the maximum velocity of the oligomer stream, in order to avoid shape deformation of the particles. Although we have only generated particles greater than 3 μm using continuous flow, preliminary experiments showed that we could synthesize even smaller objects ($\sim$1 μm) in a stop-polymerize-flow mode. In addition to controlling particle size and shape, our approach allows for the selection of various particle chemistries. The oligomer streams used in this process can incorporate diverse functional moieties in order to synthesize particles that are field-responsive [56], pH and temperature responsive, [57], or protein-loaded [54] for applications in self-assembly, rheology, biosensing and drug-delivery.

3.3.4 Janus Particles

Entities with multiple chemistries [22,23,57] are proving to be important in sorting and targeting applications [58] or in self-assembly studies [12]. Using our technique, particles with two or more functionalities may be easily and controllably synthesized. Exploiting the diffusion limited mixing seen in laminar flow(Figure 3.4a,b), we have synthesized bi-functional Janus particles(Figure 3.4c,d,e) by polymerizing rectangular particles across the interface of co-flowing oligomer and rhodamine-labelled oligomer streams. By controlling the location of the interface using the flow rates of the streams or the location of the projected light by moving the microscope stage, we can synthesize particles that contain variable proportions of different chemistries. By simply flowing multiple, concurrent, laminar streams through a microfluidic device and polymerizing particles across these streams, our approach may be used to generate particles with several adjacent chemistries. The ability to tune the proportion of so many chemistries allows for great flexibility in the design of barcoded particles.

3.4 Characterization of CFL

In this section, we characterize the CFL process in greater detail. Specifically, we talk about the oxygen inhibition effect that enables CFL, the effect of using different microscope objectives on the process and also about the properties of the particles formed.

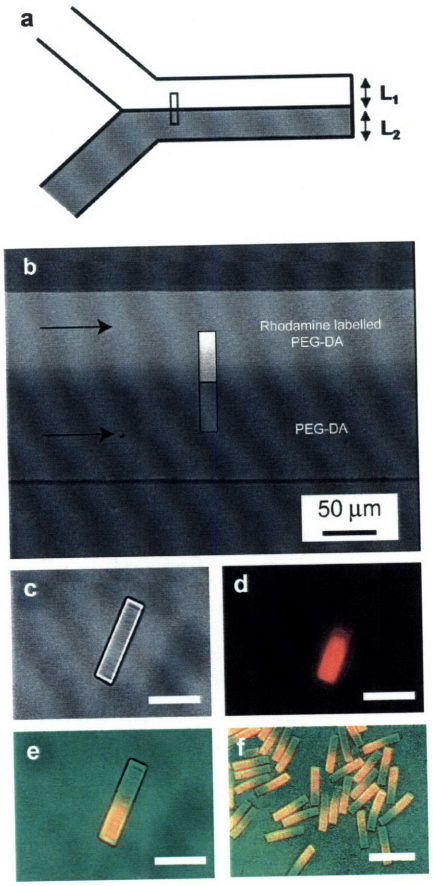

Fig. 3.4: *Synthesis of Janus particles. a)A schematic diagram showing the synthesis of Janus (two-faced) particles. The widths of the streams, L_1 and L_2 can be altered by changing the flow rates of the streams. b)Two streams containing PEG-DA (grey) and PEG-DA with rhodamine-labelled cross-linker (white) are coflowed through a channel. A schematic representing the formation of a bar-shaped particle 130 µm in length and 20 µm width is overlaid on the picture. Diffusion limited mixing seen in laminar flow is exploited to ensure the streams flow distinctly. c)DIC image of a Janus particle. d)Fluorescence microscopy image of the particle in c). The rhodamine-labelled portion is seen in red. e)An overlaid image of the entire particle showing both the fluorescently-labelled (orange) and the non-labelled (green) sections. The scalebar in Figures ce) is 50 µm. f)Multiple Janus particles with the fluorescent portion shown in orange. The scalebar is 100 µm.*

3.4.1 Oxygen Inhibition Effect

The serendipitous ability of the particles to flow in CFL is because molecular oxygen diffusing through the PDMS surfaces reacts with initiator species to form chain-terminating peroxide radicals [55], leaving a non-polymerized lubricating layer near the PDMS walls(inset of Figure 3.1a). The phenomenon of oxygen inhibition at the PDMS walls is applicable to any free-radical polymerization, rendering our approach suitable for a broad range of polymer chemistries.

The height of the inhibition layer was inferred by subtracting the particle height from the channel height and dividing this value by two. Experiments revealed that the height of the inhibition layer was ~ 2.5 μm for channels of different heights - 9.6, 20, 38 and 75 μm when an exposure time of 0.1s was used.

Symmetry of the Inhibition Effect

Replacement of either the top or the bottom PDMS surface with glass caused the sticking of particles to the top or bottom wall respectively. This is due to the absence of the oxygen inhibition effect, allowing the particles to polymerize all the way up to the glass surface. To quantify the height of the inhibition layer at the top and bottom walls, an experiment was performed by replacing the PDMS-coated glass slide used as the bottom wall with a bare glass slide. Under similar experimental conditions ($t_{exp} = 0.1$s and a 360 μm square mask using a 20$\times$ objective), objects of height 35.5 μm were formed in a 38 μm high channel when a plain glass slide was used for the bottom wall while objects of height 33 μm were formed in an all-PDMS device, demonstrating that the inhibition layer was 2.5 μm at both the bottom and top walls of the device.

Effect of PDMS Properties

We also found that varying the thickness of the PDMS device and crosslinking density (by varying the relative proportions of the Sylgard PDMS components) did not lead to any detectable change in the height of the polymerized particles. The geometry of the problem is such that the channel appears as a thin line when viewed at the length scale of the PDMS block. In previous work [59] we have shown that this leads to a weak (logarithmic) dependence on the PDMS thickness for the steady-state mass transfer problem in the PDMS due to the roughly cylindrical symmetry of the problem at this length scale. Furthermore, in the current problem for typical exposure times (~ 0.1 s) the oxygen diffusion penetration length scale in the PDMS is only ~ 25 μm (using [60] $D = 3.4 \times 10^{-9} m^2/s$). Thus the thickness of the PDMS device does not play a strong role in controlling the oxygen mass transfer in this problem.

3.4.2 Effect of Microscope Objective

Polymerization of particles can be achieved using microscope objectives with different magnifications. The larger the magnification of the objective, the smaller the spot size is and the smaller the size of individual particles are when using the same mask. The actual magnification factor of an objective is the ratio by which the mask size is reduced when projected. This is different from the magnification of the objective because of an additional lens (2.57$\times$) in the optical path between the field-stop slider and the objective.

Two key properties of a microscope objective that are important to consider in photolithography applications are resolution and depth of field (Table 3.1). The resolution of an objective is the

smallest feature size that can be discerned using it. The depth of field is the region of the light beam which can be considered straight leading to the formation of structures with straight sidewalls. The theoretical resolution of different objectives was calculated using Rayleigh's formula ($=\frac{0.5\lambda}{NA}$), where λ is the wavelength of light used (365nm) and NA is the numerical aperture of the objective. The practical resolution shown is the size to which a 10 μm feature on a transparency mask would be reduced using different objectives. The depth of field was calculated using an equation provided by the lens manufacturer (Zeiss). DOF (μm) = $\frac{1000}{7\times NA\times M} + \frac{\lambda}{2NA^2}$ where M is the magnification of the objective and NA its numerical aperture. Higher magnification objectives provide greater resolution at the cost of lower depth of field.

Objective	Actual Magnification	Theoretical Resolution (μm)	Practical Resolution (μm)	Depth of Field (μm)
20×	7.8	0.37	1.29	15.69
40×	15.6	0.24	0.64	5.38
63×	24.5	0.15	0.41	2.13
100×	38.9	0.13	0.26	1.2

Table 3.1: *The properties of different objectives lenses used in the study.*

3.4.3 Effect of Channel Height and Mask Size

The effect of channel height and mask size on the particles formed was characterized. The data shown in Figure 4.4 were obtained by polymerizing square particles using several mask feature sizes ranging from 10 μm to 500 μm in dimension. The projected sizes of these squares are shown on the y-axis. The mask was used to expose a stationary layer of PEG-DA in a microchannel, containing all-PDMS walls. The exposure time was varied and the minimum exposure time required to polymerize a square within a tolerance of 10% in feature size was noted.

Below a critical mask feature size, it was found that the intensity of the UV light emanating from the microscope objective was dependent on the size of the transparency mask used. Above this critical feature size (~250 μm in the field-stop plane), the light intensity was equal through any aperture dimension and led to the polymerization of all such features in equal times. Below this critical size, the beam intensity was found to decrease with the size of the feature. This variation in intensity is caused by clipping of the light passing through the mask, which is a result of the increasing divergence of the light beam as the aperture size is decreased [61]. This decrease in intensity was verified in an experiment that measured the intensity of light in a fluorescein solution confined between two glass slides. Masks containing square features ranging in size from 10 μm to 500 μm were used to change the aperture size.

In addition, it was found that decreasing channel height caused the exposure time to polymerize the same mask features to be increased. As channel height is decreased, the oxygen inhibition effect plays a more pronounced effect because oxygen now has to diffuse a shorter distance to reach the center of the channel causing longer lag times. These effects are further investigated in Chapter 7.

3.4.4 Effect of Flow Rate on Particle Features

As the flow rate was increased, particles were increasingly smeared upon formation. There exists a maximum velocity for each feature size above which particle smearing is unacceptably large. Data were obtained using the 20× objective and 9.6, 20 and 38μm high channels. This plot may be used as a guide to find the maximum velocity that can be used to make a certain feature size. Particle throughput decreases with size in CFL.

3.4.5 Polydispersity of Particles

To quantify polydispersity, we measured (using bright-field microscopy) the in-plane (xy) and out-of-plane (z) dimensions of cylindrical particles synthesized under the same conditions as those shown in Figure 3.7c. The particles were polymerized with the 20× objective in a 38μm tall channel for 100ms using a mask with 250μm circular features. For these cylindrical particles, we found the mean particle diameter to be 29.6μm and the mean height to be 32.8μm (distributions are shown in Figure 3.7). The coefficient of variation (COV) of a feature is calculated as the standard deviation divided by the mean. For these data the COV for the diameter and height are 0.64% and 1.19%, respectively. For comparison, particles polymerized with the same mask but a 40× objective and 50ms UV exposure had COV for the diameter and height of 1.29% and 1.07%, respectively. For all conditions we studied, the COV of each particle feature was less than 2%.

3.4.6 Extent of Double Bond Conversion in Particles

We used FTIR spectroscopy to quantify the conversion of acrylate groups in the particles as done previously [62]. Specifically, we monitored IR transmission at 1635cm^{-1}, which corresponds to the terminal C=C stretch in the acrylate end groups. We synthesized large, flat disks with UV exposure

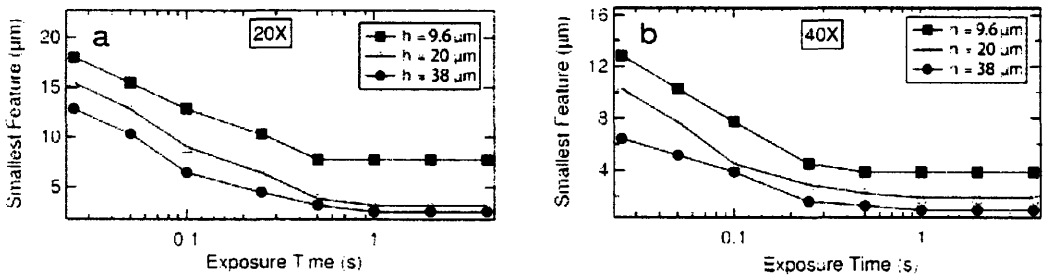

Fig. 3.5: *Exposure time characterization. Plots showing the smallest feature that can be polymerized at a given exposure time in channels of varying height. Within each plot are three curves representing the variation in feature size vs. exposure time in channels of three different heights, 9.6 μm, 20 μm and 38 μm. Data are shown for two objectives. a) 20X. b)40X. As feature size or channel height were decreased, longer exposure times were required to polymerize particles.*

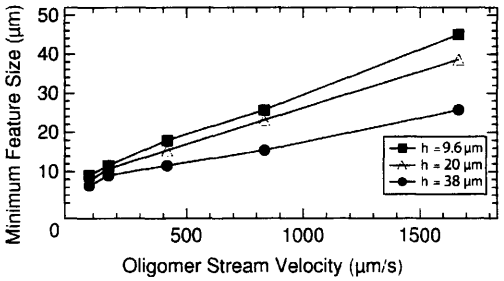

Fig. 3.6: *Limits on flow rate for particle synthesis. The plot shows the experimentally determined minimum feature size that can be formed without deformation (using a tolerance factor of 10% in length scale) at a given velocity of PEG-DA oligomer solution.*

doses of 50 and 100ms in channels 9.6um, 20um, and 38um tall. These parameters correspond to those used to generate the particles shown in Figures 1-4 of the main text. The disks were collected, separated from residual monomer using a gentle argon flow, and clustered on CaF_2 FTIR crystals. Spectrum backgrounds along with monomer and fully crosslinked standards were collected for each crystal. Conversions calculated from FTIR data are shown in Table 3.2.

The critical double bond conversion for gelation in concentrated, multifunctional homopolymer systems such as ours has been predicted to be very low (< 1%) [63]. Our conversions range from 15% to greater than 75%, well beyond the predicted gel point. For comparison, PEG particles synthesized for protein release by another group had similar conversions (20 - 70%) [64]. Our conversion calculations are conservative estimates due to the nature of the experiment. Thinner particles (polymerized in low-height channels) were more difficult to dry of residual monomer (that clings to the outside of the particle) without losing the particles in even the gentlest argon flow.

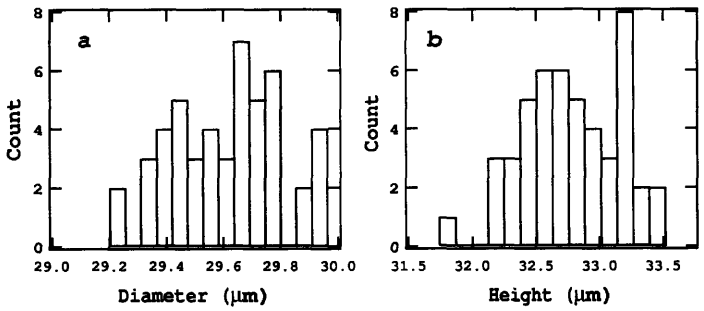

Fig. 3.7: *Typical histograms of particle dimensions. These particles were polymerized with a* 20× *objective. a)In-plane measurements (circular face diameter) and b) out-of-plane measurements (height).*

Objective	Channel Height (μm)	Exposure (ms)	Conversion	Figure Reference
20×	38	50	69%	3.2b
20×	38	100	77%	3.2c,3.3e,f
20×	20	50	20%	3.3a,g,h,i, 3.4c,d,e,f
20×	20	100	70%	3.1b,c, 3.3b,c
20×	9.6	100	15%	3.2a,d
40×	9.6	100	42%	3.3d

Table 3.2: *Conversion of acrylate groups in PEG-DA particles polymerized for 50 or 100ms in varying channel heights. The last column refers to figures in the main text that show particles generated under the specified conditions.*

Therefore, these reported conversions are to be considered lower bounds.

As expected, both increase in channel height and exposure dose resulted in more fully-crosslinked particles. Beyond FTIR data, all particles shown in this study were stable under flow, pipetting, centrifugation, and vigorous rinsing, further demonstrating the mechanical integrity of particles generated using our approach.

3.5 Conclusion

In this chapter, we have demonstrated that CFL can be used to continuously synthesize polymeric particles of varied complex shapes and multiple chemistries. The advantage over traditional lithography techniques [25, 48] is the continuous nature of the process, permitting the high-throughput generation of polymeric particles. The morphology and the chemistry of the particles can be independently chosen to form large numbers of uniquely-shaped, functionalized particles for applications including drug delivery, biosensors, microactuators and fundamental studies on self-assembly and rheology. Greater control of particle morphology could potentially be achieved using gray-scale photomasks, multiphoton illumination or multiple beam lithography [65].

CHAPTER 4

Amphiphilic Polymeric Particles

4.1 Introduction

Thus far, we have mainly described processes that result in the creation of non-spherical but chemically homogeneous particles. In Chapter 3, we talked about how CFL can be used to synthesize even chemically inhomogeneous Janus particles. In this chapter, we extend this concept to synthesizing amphiphilic particles with distinct hydrophilic and hydrophobic sections.

Wedge-shaped amphiphilic particles bearing segregated hydrophilic and hydrophobic sections were synthesized in a microfludic channel by polymerizing across laminar coflowing streams of hydrophilic and hydrophobic polymers using CFL. The amphiphilic particles were allowed to self-assemble in water or at water-oil interfaces. In water, the geometry of the particles enabled the formation of micelle-like structures while in emulsions the particles migrated to the oil-water interface and oriented themselves to minimize their surface energy. The motivation for these amphiphilic particles came from particle surfactants.

4.1.1 Particle Surfactants

Amphiphilic molecules are often represented by objects in the spectrum of shapes between a cone and a cylinder, where the body of the object represents the hydrophobic tail and the hydrophilic head is represented by one of the circular faces [66]. This spectrum of shapes is used to show the effect of geometry on packing. Changing the geometry of the molecules results in different

aggregated structures such as micelles, bilayers and reversed micelles being formed. The two-dimensional analogs of such objects are wedge-shapes that fall in the spectrum between triangles and rectangles. We therefore chose to synthesize amphiphilic wedge-shaped particles - both to illustrate the power of CFL to synthesize any extruded 2-D shape, and to allow for geometry-induced aggregation later in our study. Analogous to the molecular scale, amphiphilic particles synthesized in our study have a hydrophilic head and a hydrophobic tail, whose relative proportions can be easily changed.

4.1.2 Immiscible Interfaces in Microfluidics

Previously, we demonstrated that CFL can be used to fabricate 'barcoded' particles by polymerizing across miscible, chemically similar coflowing streams [38]. In this case, the interface between the different regions in a particle is not sharp due to molecular diffusion. Furthermore, the miscible nature of the fluids means that the different regions of the particle will typically have similar surface energies. In this paper, we use CFL to synthesize particles with specific shapes that bear spatially segregated chemistries with contrasting properties and different surface energies. To accomplish this, we use parallel streams of immiscible polymer coflowing through a microfluidic device.

The use of immiscible fluids in microfluidic devices has been explored extensively [67] to study, for example, drug partitioning behavior [68], to achieve tunable liquid microlenses [69], to perform interfacial reactions [70] or for accomplishing separations [71]. Others have probed the experimental phase space of device operation using immiscible fluids to determine conditions when different regimes such as droplet breakoff [29, 42] and parallel coflow [53, 72, 73] are observed. In our study, coflowing immiscible photopolymeric materials are used to synthesize particles with a sharp interface separating hydrophilic and hydrophobic sections. After synthesizing the particles, we exploit their 'amphiphilic' nature by allowing them to self-assemble in water and at oil-water interfaces. Like their molecular analogs, the particles assemble differently in water, o/w or w/o emulsions in order to minimize their surface energy.

4.2 Experimental Methods

4.2.1 Materials.

The hydrophobic phase consisted of a 5% (v/v) solution of Darocur 1173 (Sigma Aldrich) initiator in tri(methylpropane) triacrylate (TMPTA, Polysciences). The hydrophilic phase consisted of 5% (v/v) solutions of Darocur 1173 (Sigma Aldrich) initiator in a 65% aqueous solution of poly(ethylene glycol)(600) diacrylate (PEG-DA, Sigma Aldrich). Since TMPTA is insoluble in water, the two phases were immiscible. PEG-DA and TMPTA are reported by the manufacturer to have viscosities of 90 centipoise and 106 centipoise at 25°C.

4.2.2 Microfluidic Devices

Devices were fabricated by pouring polydimethylsiloxane (PDMS, Sylgard 184, Dow Corning) on a silicon wafer containing positive-relief channels patterned in SU-8 photoresist (Microchem). The devices were Y-shaped rectangular channels of width 200 or 300 μm and height 30 μm. These devices were placed on glass slides spin-coated with PDMS to ensure that the oligomer was exposed only to PDMS surfaces. Devices were mounted on an inverted microscope (Axiovert 200, Zeiss)

and the formation of the microparticles was visualized using a CCD camera (KPM1A, Hitachi). Images were captured and processed using NIH Image software or a Nikon D200 camera and Nikon Capture software.

4.2.3 Photopolymerization Setup

Photomasks were designed in AUTOCAD 2005 and printed using a high resolution printer at CAD Art Services (Poway, CA). The mask was then inserted into the field-stop of the microscope. A 100W HBO mercury lamp served as the source of UV light. A filter set that provides wide UV excitation (11000v2: UV, Chroma) was used to select light of the desired wavelength and a VS25 shutter system (Uniblitz) driven by a computer controlled VMM-D1 shutter driver provided specified pulses of UV light. Oligomer solutions were driven through the microfluidic device using a KDS 100 syringe pump (KD Scientific). Particles were formed across the interface of the two streams after aligning the mask shapes to be parallel to the interface. Typical exposure times used were 0.03-0.05s and flow velocities used varied between 100-300 μm/sec. All particles shown in this study were made using exposure times of 0.03s. A reservoir was cut in the PDMS to collect the particles.

4.2.4 Particle Characterization and Emulsion Formation

The sizes of the particles were estimated as they were being formed by capturing images of the flowing particles using low camera exposure times (1/10000s). Statistics were estimated on a 100 consecutive particles formed at an exposure time of 0.03s. Conversion of double bonds was estimated using FTIR spectroscopy performed on a Nikolet spectrometer (Thermo Corp.), by measuring the decrease in terminal C=C stretch at 1635 cm^{-1} in a thin film of cross-linked polymer [74]. To perform FTIR, individual samples of either the hydrophilic or the hydrophobic monomer were prepared by loading the respective oligomer into a channel with the same dimensions as the device used and then given exposure doses of 0.03s (same as the formed particles) and 120s (fully cross-linked). Strips of polymer film were formed that were used for FTIR measurements. Contact angle measurements were performed using the sessile drop method and a DSA 10 tensiometer (Kruss). Advancing contact angle measurements were made on a drop of the required polymer placed on a clean PDMS surface.

To make w/o type emulsions, 20 μl of toluene was added to 10 μl of a water-in-monomer emulsion, containing the particles isolated from the reservoir, and then agitated using a vortex mixer. Both monomers are soluble in toluene resulting in the formation of water in toluene droplets. To make o/w type emulsions, 5 μl of a water-in-monomer emulsion, containing the particles isolated from the reservoir, along with 5 μl of toluene was added to 20 μl of DI water and then agitated using a vortex mixer. This resulted in the formation of toluene-in-water droplets. 20 μl of either emulsion are then sandwiched between two PDMS coated glass slides in order to create two-dimensional structures for observation on the microscope.

4.3 Results and Discussion

An all-PDMS, Y-shaped, microfluidic device containing two ports, one to introduce each phase, is used in the synthesis of the particles (Figure 4.1a). The device is placed on a movable microscope stage and UV light is provided from a mercury lamp attached to the microscope. A

hydrophilic phase consisting of an aqueous solution of poly(ethyleneglycol) diacrylate (PEG-DA) and a hydrophobic phase consisting of tri(methylpropane) triacrylate (TMPTA) flow parallel to each other through the rectangular channel, with stream widths controlled by their relative flow rates and viscosities. The flow rates for the two streams are constrained to be in a regime where parallel coflow is observed [73]. As illustrated in Figures 4.1a and 4.1b, wedge-shaped particles are polymerized, five at a time, across the coflowing streams using projection lithography and a 20X microscope objective. Copolymerization of the two acrylates used leads to a chemical linkage of the hydrophilic and hydrophobic sections at the interface, lending stability to the particles formed. The particles synthesized are approximately 1/8th of their mask size and are able to form and flow continuously because of the oxygen-induced inhibition [55] of polymerization at PDMS surfaces. During the polymerization process, oxygen diffusing in through the PDMS reacts with the initiator species, converting them to chain-terminating peroxide radicals. This results in the formation of a thin uncrosslinked, lubricating layer of oligomer near the PDMS walls that enables the particles to flow [38]. A reservoir used to collect the particles is positioned immediately downstream of the polymerization zone so that the particles formed exit the microchannel and do not alter the flow profile upstream. In our setup, the proportions of the hydrophilic and hydrophobic sections could be conveniently altered by moving the microscope stage, which alters the position of the interface, changing the fractional amount of each chemistry in the particle.

When two immiscible fluids flow through a Y-junction, either droplet breakoff or coflow of the two streams can be observed, depending upon the flow rates used [73, 75]. We have chosen to operate in a regime where coflow is observed in order to make amphiphilic particles in a controllable fashion. Because the fluids used are immiscible, they coflow all the way to the exit of the microfluidic device. This leads to a segregation of the two phases all along the interface and is convenient for the formation of large numbers of particles where diffusive mixing [2] might otherwise constrain the region available for polymerization. Channels with high-aspect ratios (width/height $\gg 1$) are known to increase the operational phase space for the coflow of streams [73]. The channels we have used have aspect ratios ranging between 7-10 leading to stable flow rates with velocities as low as 100 μm/s for both phases. The particles shown in Figure 4.1b were formed using an exposure time of 0.03s and a flow rate of 0.1 μl/min for both phases. A pause of 5s was used between successive exposures.

4.4 Particle Characterization

4.4.1 Monodispersity

A comprehensive analysis of particle monodispersity was performed by measuring the distribution of the five different length variables, w_1, w_2, w_3, h_1 and h_2 indicated in Figure 4.1b. In addition to the mask-defined edges of the particles (w_1, w_3 and (h_1+h_2)), the lengths of their hydrophilic (h_1) and hydrophobic (h_2) portions are dictated by the precise position of the interface when polymerization occurs. These lengths are all measured as the particles formed in the microfluidic device. Their distributions are shown in the histogram plots in Figures 4.1c-g. In all five dimensions that were measured, the coefficient of variation (COV) in size is less than 2.5% so that the particles can be classified as monodisperse [76]. Furthermore, by changing the length of the hydrophilic (h_1) and hydrophobic (h_2) sections, the extent of their amphiphilicity could also be tightly controlled. The thickness of the particles (y-direction in Figure 4.1b) is measured to be 25 μm which corresponds

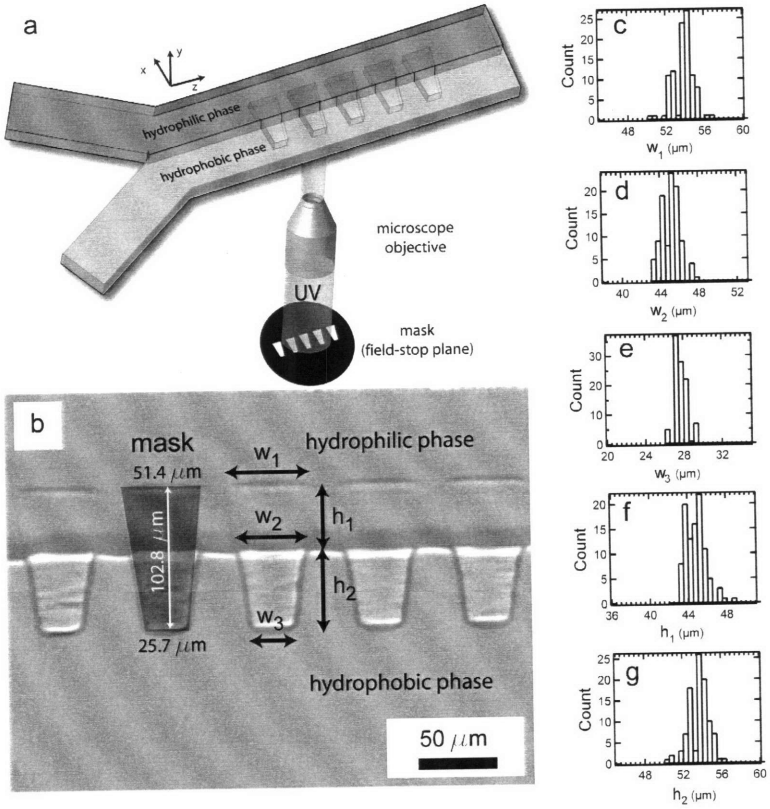

Fig. 4.1: *Synthesis of biphasic particles containing hydrophilic and hydrophobic chemistries. a)Schematic depicting the formation of biphasic particles. Mask-defined wedge shapes are polymerized, five at a time, across two parallel coflowing streams containing hydrophilic and hydrophobic chemistries using continuous flow lithography. b) Brightfield image of five particles simultaneously being polymerized across co-flowing immiscible streams - one containing an aqueous solution of a hydrophilic oligomer (PEG-DA) and the other containing a hydrophobic oligomer (TMPTA). The expected dimensions of the particle are overlaid on the second particle from the left. The dimensions of interest are labelled on the third particle from the left. c-g)Histograms showing the distribution of sizes in the dimensions of interest. These were measured as the particles were being made in the device. The mean values obtained are $w_1 = 53.7\ \mu m$, $w_2 = 45.1\ \mu m$, $w_3 = 27.7\ \mu m$, $h_1 = 44.8\ \mu m$ and $h_2 = 53.6\ \mu m$. In all five dimensions, the COV is less than 2.5%. In addition the thickness of the particles (in the y-dimension) is measured to be 25 μm.*

to a lubrication layer of thickness 2.5 μm at the top and bottom walls [38].

The synthesized particles are allowed to collect in a reservoir, where they are pictured in Figures 4.2a and Figure 4.2b. The particles shown are dispersed in ethanol in order to avoid clustering. As both the hydrophilic and hydrophobic polymeric precursors are completely soluble in ethanol, there is no preferential alignment of the particles. As seen in the figures, the hydrophilic and hydrophobic sections of the particles are clearly distinguishable because of the difference in the refractive indices of the two sections. The hydrophilic section swells to a greater extent in ethanol, leading to a slight distortion in the original shape. The particles seen in Figure 4.2b are formed by inverting the mask so that the hydrophilic head is now smaller and the hydrophobic tail is the broader section. SEM images of individual particles from Figures 4.2a and 4.2b are seen in Figures 4.2c and 4.2d respectively - their two distinct sections are again clearly visible. As seen in the images, when dry, the hydrophilic phase shrinks in comparison to the hydrophobic phase. To show that the method is general enough to synthesize different kinds of non-spherical particles with chemical anisotropy, we have also synthesized amphiphilic particles with a rod-like hydrophobic tail and a disk-shaped hydrophilic head (Figure 4.2e). Such a library of particles could be very useful when studying the effect of geometry and chemical anisotropy on meso-scale self assembly [12] and rheology.

4.4.2 Interfacial Curvature

As seen in Figure 4.2b, a cross-sectional (x-y plane in Figure 4.1) view of these particles shows that the interface between the two sections has a finite curvature. This is caused by the immiscibility of the two flowing streams, leading to a sharp, curved interface (Figure 4.3b). As depicted in the schematic (Figure 4.3a), the hydrophobic ('o') phase preferentially wets the PDMS over the hydrophilic ('w') phase. The contact angle at the interface between the two phases and the PDMS wall, β, is dictated by the interfacial tension between the hydrophilic phase and the hydrophobic phase as well as by the solid-liquid interfacial tension between the PDMS and the two phases. When the imposed flow rates are changed, we observe that the widths of the streams are altered to minimize the pressure drop across the interface to a value that can be sustained by the equilibrium curvature of the interface. The interface is then observed to translate but it then reaches an equilibrium state where its curvature and contact angle at the solid surface are not affected by the flow rates [73]. Since the interface formed is orthogonal to the direction of flow and does not move after reaching steady state, we believe that the interfacial properties measured for a stationery droplet can be used in the following analysis. Using simple geometry, we predict the radius of curvature of the interface to be

$$R = \frac{H}{2cos\beta} \tag{4.1}$$

where H is the height of the channel. A simple force balance at the contact line (point C in Figure 4.3a) gives

$$\gamma_{ow}cos\beta = \gamma_{ws} - \gamma_{os} \tag{4.2}$$

where γ_{ow} is the interfacial tension between phase 'o' and phase 'w', and γ_{os} and γ_{ws} are the solid-liquid interfacial tensions between PDMS('s'), and phase 'o' and 'w' respectively. The right-hand-side of Equation 7.2 can be represented in terms of conveniently measurable properties like the contact angle of phase 'o' and phase 'w' on a PDMS surface surrounded by air and the surface

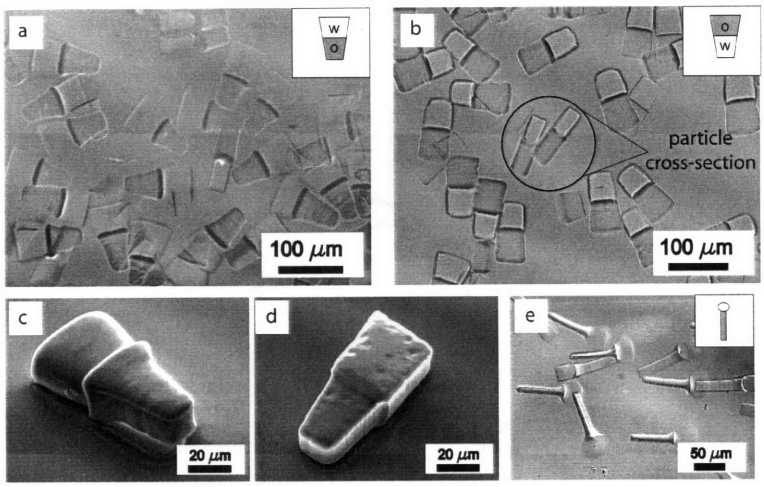

Fig. 4.2: *Biphasic particles synthesized using CFL. The inset in a), b) and e) shows the type of particle in each figure. The hydrophilic head is represented in white and indicated by the letter* 'w' *while the hydrophobic tail is represented in grey and indicated by the letter* 'o'. *a)Differential Interference Contrast (DIC) images of particles with a large hydrophilic head and a smaller hydrophobic tail in ethanol. The particles were made at exposure times of 0.03s and flow rates of 0.1 μl/min for each stream, collected in a reservoir and washed in ethanol. The ethanol swells the large hydrophilic head resulting in a slight distortion from the original shape. b)DIC images of particles with a small hydrophilic head and a larger hydrophobic tail in ethanol. Particles were made at exposure times of 0.03s and flow rates of 0.05 μl/min for each stream. The ethanol now swells the small hydrophilic head. c)SEM image of one of the particles in a). The hydrophilic head has shrunk on drying. d)SEM image of one of the particles in b). The hydrophilic portion has shrunk on drying. e)DIC images of ball-and-stick model biphasic particles with a hydrophilic disk-shaped head and a long hydrophobic tail.*

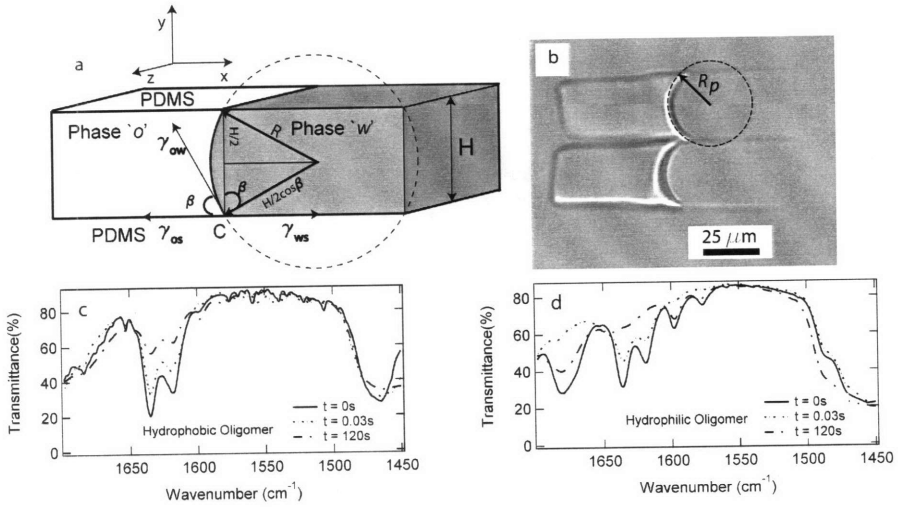

Fig. 4.3: *Characterization of particles. a)A schematic showing the cross-section of the microfluidic device - the x-y dimensions in Figure 4.1a are now visible. The interface between the hydrophilic and hydrophobic sections has a radius of curvature that is a function of the interfacial tensions between the two streams and the solid-liquid interfacial tension between the PDMS and the two streams. b)A cross-sectional view of two particles lying on their sides. The curved interface between the hydrophilic and the hydrophobic portions depicted in a) is clearly seen. The predicted radius of curvature of the interface, R_p = 17.4 μm, is overlaid on one of the particles as a guide to the eye. The measured radius of curvature using 10 particles is, R_m = 16 μm ± 1.5 μm. c)FTIR data showing conversion of double bonds in the hydrophobic oligomer at t = 0s, 0.03s and t = 120s (fully cross-linked). At t = 0.03s, 35% of all double bonds are converted. d)FTIR data showing conversion of double bonds in the hydrophilic oligomer at t = 0s, 0.03s and t = 120s (fully cross-linked). At t = 0.03s, 47% of all double bonds are converted.*

tensions of phase 'o' and phase 'w'.

$$\gamma_{ws} = \gamma_{sa} - \gamma_{wa}cos\theta_w \tag{4.3a}$$

$$\gamma_{os} = \gamma_{sa} - \gamma_{oa}cos\theta_o \tag{4.3b}$$

where γ_{sa} is the surface tension of a native PDMS surface, γ_{oa} and γ_{wa} are the surface tensions of phases 'o' and 'w' respectively. θ_o and θ_w are the contact angles of phases 'o' and 'w' on a native PDMS surface respectively. Subtracting Equation 4.3b from 4.3a, we eliminate γ_{sa} to get

$$\gamma_{ws} - \gamma_{os} = \gamma_{oa}cos\theta_o - \gamma_{wa}cos\theta_w \tag{4.4}$$

Using Equations 6.3, 7.2 and 7.4 we now have

$$R = \frac{H\gamma_{ow}}{2(\gamma_{oa}cos\theta_o - \gamma_{wa}cos\theta_w)} \tag{4.5}$$

Using experimentally measured values of $\gamma_{ow}(7.35 \pm 0.12\text{mN/m})$, $\gamma_{wa}(40.49 \pm 0.24\text{mN/m})$, $\gamma_{oa}(32.59 \pm 0.26\text{mN/m})$, $\theta_o(51°)$ and $\theta_w(69.5°)$ and using H = 30 μm, we predict R = 17.4 μm (Figure 4.3b). This matches well with the experimentally determined value of 16 $\pm$ 1.5 μm. The interfacial properties of the streams can therefore be used to tune the curvature of the interface between the two sections. We also see that the radius of curvature of the interface is proportional to the channel height.

4.4.3 Particle Crosslinking

The extent of cross-linking of the particles in the two different phases was characterized by measuring the percentage of double bonds converted using FTIR spectroscopy (Figures 4.3c & d). All particles in this study are made using 0.03s of exposure to UV light. In this time, the conversion of double bonds was found to be 47% in the hydrophilic phase and 35% in the hydrophobic phase. Since the conversion of double bonds required to cross-link multifunctional acrylates successfully is typically less than 5%, [63]we conclude that the exposure dose received is sufficient to cross-link the particles.

4.5 Particle Assembly

Like amphiphilic molecules, particles possessing both hydrophilic and hydrophobic sections exhibit a tendency to orient themselves in order to minimize their surface energy [25, 26]. While thermal energy alone is insufficient to enable these particles to explore their energy landscape, providing external energy through agitation helps these particles find their energy minima and self-assemble. In a series of experiments we isolated the amphiphilic particles that we formed and induced them, using agitation, to assemble either in a pure aqueous phase or at the interface of w/o or o/w emulsions. The results show that the particles have a strong tendency to orient themselves in order to minimize their surface energy. In the upper right corner of each picture in Figure 4.4, we have drawn cartoons of the particle to clarify what particles have been used in each experiment. In these cartoons, the symbol 'w' refers to the hydrophilic section of the particles and 'o' to their hydrophobic sections. Particle assembly was restricted to two dimensions by performing experiments in a film

of fluid that is sandwiched in between two PDMS-coated glass slides.

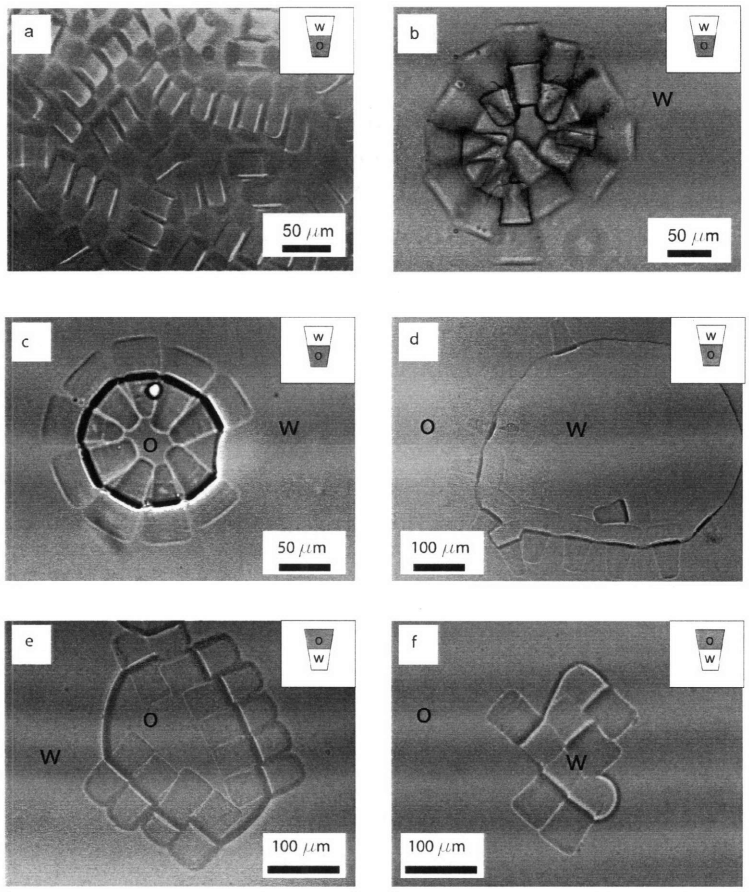

Fig. 4.4: *Self-assembled structures formed using biphasic hydrophilic-hydrophobic particles. In a-f, the cartoon in the inset shows an individual particle with its hydrophilic portion labelled, 'w' and its hydrophobic portion labelled, 'o'. a)Particles with a large hydrophilic head and a small hydrophobic tail cluster in a bath of TMPTA. Their hydrophobic tails are all uniformly pointed out of the page while their hydrophilic heads point into the page. b) Particles seen in a) form a micelle-like structure in water. The geometry of the particles enables them to form a circular structure to shield the inner hydrophobic sections. c&d)Particles with a large hydrophilic head and a small hydrophobic tail assemble at the interface of an oil-in-water and a water-in-oil emulsion respectively. The hydrophilic section preferentially stays in the water while the hydrophobic section stays in the oil. e&f)Particles with a small hydrophilic head and a large hydrophobic tail at the interface of an oil-in-water and a water-in-oil emulsion respectively. The hydrophilic head swells in water leading to deformation of the particles from their original shape.*

4.5.1 'Micelle' Formation

We first looked at particles in a single external phase. Even when clustered in the reservoir in a phase containing only monomer, the particles showed a tendency to keep their like sections close to each other(Figure 4.4a). As seen, all the particles have their hydrophilic heads pointing into the page and their hydrophobic tails pointing out of the page. Further when the particles with a large hydrophilic head and a smaller hydrophobic tail were agitated, they clustered to form micelle-like structures (Figure 4.4b) when dispersed in water. As seen in the figure, the particles form a closed structure in order to shield the hydrophobic tails from the external aqueous phase. The tapering wedge-shaped geometry of the particles induced the curvature of the micelles.

4.5.2 Particles in Emulsions

We also found that when a particle-loaded 2-phase system containing water and toluene is agitated to form emulsion droplets, the particles preferentially migrated to the interface between the two phases as expected [32, 37, 77, 78]. Such particles are strongly adsorbed at interfaces because of the energetic gains caused by both the decrease in '*o-w*' interfacial area and the partitioning of the solid phases into the preferred liquid phase (PEG-DA in water and TMPTA in toluene). Particles with a large hydrophilic head and a small hydrophobic tail orient themselves at the interface of an oil-in-water emulsion such that the entire hydrophilic portion is in the water while the hydrophobic section is confined to the oil (Figure 4.4c). The interface between oil and water is clearly seen where there is a gap between particles. When the same particles are introduced into a two-phase system that is prone to forming water-in-oil type emulsions, the particles now change their orientation so that their hydrophobic tails are in the oil while their hydrophilic heads are confined to the water droplet (Figure 4.4d). Particles with a small hydrophilic head and a large hydrophobic tail assemble at the interface of o/w or w/o emulsions such that their surface energy was minimized (Figures 4.4e and 4.4f). The particles also deform the emulsion droplets in order for the interface between the two particle sections to coincide with the emulsion droplet interface (Figures 4.4d and f)

4.6 Conclusion

In this chapter, we have described a microfluidic method that allows for the synthesis of generic 2-D extruded shapes that also contain spatially segregated chemical functionality. By polymerizing across laminar coflowing streams containing different chemistries, we have shown the synthesis of particles bearing both hydrophilic and hydrophobic chemistries. Using flowing streams of polymer in a microfluidic device we are able to provide much higher particle throughput than polymerization performed across static fluids. Also, by using a fluid-fluid interface that is parallel to the path of propagation of light, we are able to make different sections of the particle such that they bear different geometries. The method is equally applicable to synthesizing particles containing magnetic, pH responsive or other kinds of chemistries. Particle shape may be conveniently defined using a mask and the extent of each chemistry can be tuned simply by moving the microscope stage or by altering the widths of the streams (when more than two streams are present). This method possesses the unique advantage of being able to generate particles containing more than two chemistries in any extruded 2-D shape. For example, we can go beyond the Janus '*o-w*' motif presented here and create '*o-w-o*' bar-shaped particles. The interface between the independent sections of the particles may be tuned by changing the surface properties of the streams, while the mechanical properties of

the particles can be altered by varying exposure time and hence cross-linking density. The length scale of the particles synthesized in this study is on the order of 100 μm but we believe that such amphiphilic particles can easily be made down to lengths of 10 μm. However, further adjustments to the technique will be required to synthesize colloidal, amphiphilic particles because of the finite curvature of the interface.

Furthermore, we have demonstrated that the chemical anisotropy of the particles may be used to aggregate the particles into structures reminiscent of their molecular analogs. This method can enable the synthesis of particles that are synthetic in design or inspired by nature (like surfactants). The particles can then serve as 'coded' building blocks that assemble to build superstructures useful both for fundamental studies and in the synthesis of new materials and devices. The method would be extremely useful to test the effect of particle geometry and chemical anisotropy on self-assembly at the micron scale. Barcoded particles [58] with multiple chemistries may also find applications in diagnostics and medicine where the detection of multiple analyte species simultaneously is of great importance.

CHAPTER 5

Stop Flow Interference Lithography in a Microfluidic Device

5.1 Introduction

5.1.1 Limitations of CFL

The flow lithography techniques that we have described in Chapters 3 and 4 are convenient for synthesizing large numbers of polymeric particles at the micron scale. However, the particle morphologies are limited to being extrusions of two-dimensional mask-defined shapes. In this chapter, we present a Stop Flow Interference Lithography (SFIL) method to synthesize three dimensional structures using a PDMS phase mask. While the method is not general enough to synthesize any 3-D shape, interesting open structures with very well defined porosity can be made in a variety of polymers.

5.1.2 Need for 3-d Structures

Polymeric structures with repeating 2-D and 3-D motifs at the micron scale and below have a variety of uses. Patterned 2-D structures have been shown to have myriad applications in biosensors [79], tissue engineering [80] and in diagnostic assay systems [13]. The use of more sophisticated 3-D structures offers tremendous possibilities in photonics [7], tissue engineering [81,82] and information

storage [83]. The synthesis of structures that possess controllable material properties and texturing across multiple length scales is important for a variety of applications. In tissue engineering, for instance, creating a gradient of molecules on the surface of a biocompatible scaffold or localizing growth factors to a specific region can influence cell adhesion and migration, providing functional cues to cells [80]. It would also be convenient to combine the control over spatial chemistry that microfluidics offers [84] with the ability to controllably texture materials at the micron scale. SFIL may provide a convenient route to tune the mechanical and transport properties of such structures in order to provide optimal conditions for cell growth and viability. Further, SFIL provides for the high throughput generation of 3-dimensionally patterned 2-D structures that could be useful to conduct cell-material assays in a mulitplexed fashion or to fabricate large numbers of microtissue templates. In particle-based biosensors [13], the sensitivity of detection is dependent on the number of probe molecules that can be functionalized on the surface of a particle. We show that patterned structures formed using SFIL can greatly increase the sensitivity of such schemes by providing large surface areas and a greater spatial density of probe molecules.

5.1.3 Other Approaches to 3-d Structures

Many attempts have been made to fabricate complex 3D structures at the micron scale and below using either top-down approaches or bottom-up techniques. Bottom-up approaches like polymer phase separation [85], molecular self-assembly [86] or colloidal assembly [87] are cheap and can cover large areas but face problems of defects and limitations in the type and geometry of structures that can be formed. While top-down methods offer precise shape control, the need to construct the 3-D structures using either a point by point or layer by layer process makes such methods as gray-scale photolithography [88], direct 3-D writing [89], 2-photon lithography [90] and confocal microscopy [91] time consuming. On the other hand, phase mask based IL is a rapid and convenient way to synthesize 3-D structures over a large area. While it is still not clear how general the 3-D structures that can be formed using IL are [92], the method offers for the synthesis of several different open structures by tuning the properties of the phase mask used.

Previously, PMIL has been used to synthesize 3-D structures mainly by flood exposing through a patterned mask, a think film of spin-coated photoresist [92, 93]. This limits the method to using standard photoresist materials and reduces throughput because of the serial nature of the processing. Further, such processes are not easily amenable to the synthesis of structures that possess gradients or chemical anisotropy. Chemical anisotropy refers to the presence of multiple segregated chemical functionalities or gradients of one chemical functionality in a structure and is particularly desirable in applications such as tissue engineering [80] or particle diagnostics [13]. On the other hand, microfluidic lithographic techniques [84] like SFL [38,94] allow for a wider range of materials including hydrogels to be used, while synthesizing large numbers of mask-defined particles and providing the ability to finely and conveniently tune the chemical anisotropy of the structures formed. However, these techniques have been restricted to the formation of particles with 2-D extruded shapes because of the use of traditional transparency masks [38,95]. Using PDMS phase masks [92] in conjunction with a PDMS microfluidic device allows for the convenient integration of IL with SFL and allows the two processes to complement each other's capabilities.

SFIL results in the high throughput synthesis of transparency mask-delimited, phase mask-defined, patterned polymeric structures. Advantages in throughput result from the ability to repeatedly form and flow out arrays of mask defined particles and structures in under a second. This

is because of the oxygen-induced inhibition [55] of free radical polymerization reactions at PDMS surfaces. During the polymerization process, oxygen diffuses in through the porous PDMS walls and reacts with free radicals, converting them to chain-terminating peroxide species. This results in the formation of a thin, uncrosslinked lubricating layer of oligomer near the PDMS walls that enables the particles to flow without sticking to the walls of the device. Chemical anisotropy can be introduced by exploiting the laminar coflow of liquids in a microfluidic device, which results from the dominance of diffusive over convective transport [2]. Material advantages result from the simple fact that even freely flowing oligomer liquids of low viscosity can be patterned in a continuous fashion without the requirement that they be spin-coated, exposed and developed in a step-wise, serial fashion.

5.2 Experimental Methods

5.2.1 Fabrication of Silicon Mold

Standard contact photo lithography was used to fabricate square grid in Si with periods ranging 2 μm and etch depths 1 μm. The tetra-layer resist stack consisted of an evaporated silica interlayer, an anti-reflection coating (ARC) layer, an evaporated silica interlayer and a photoresist layer, with the layers deposited sequentially onto silicon or thermally oxidized silicon wafers. The function of the ARC is to minimize the reflection at the bottom interface of the photoresist layer. The silica inter layer is an optically thin pattern transfer layer that is placed between the ARC and the photoresist layers in order to improve the fidelity with which the pattern is transferred into the substrate. SU-8 photoresist patteming was done using a Karl Suss MJB 3 mask aligner (Zeiss) in contact mode with power of 350-W mercury UV light source. After exposure and development of the resist, the pattern was transferred through the silica interlayer and ARC layer and SiO_2 and into the Si via reactive ion etching. After removal of the residual resist stack by cleaning in 5:1:1 H_2O:H_2O_2:NH_4OH at 80 °C for 10 min, a square-grid topography remained in the Si.

5.2.2 Fabrication of PDMS Phase Mask

Patterned Si or SiO_2 wafer served as template for generating the phase mask. After exposing the wafer to perfluorinated trichlorosilane (Sigma Aldrich) vapor in a vacuum chamber for 1 hour, poly(dimethylsiloxane) (PDMS) (Sylgard 184, Dow-Corning) prepolymer was poured on top of the patterned Si wafer. Curing (75 °C for 2 h) the PDMS and peeling it away from the master yielded a conformable phase mask. The layout of Si wafer and the relief features on the mask are shown in the inset of Figure 5.2a. In order to prevent structure formation from stamping of liquid monomer and retain the refractive index contrast between air and phase mask, a thin PDMS layer is applied on top of the phase mask. The detailed process is as follows: a 3 μm thin film of PDMS was prepared by spin-coating diluted PDMS prepolymer (prepolymer:hexane=1:4) on the pre-treated glass slide with Victawet®(SPI supplies, 5w% Victawet soln in water) and curing at 75 °C for 2 hr. After Oxygen plasma treatment for 1 min on both sides of phase mask and PDMS thin layer, the PDMS thin layer is carefully laminated on top of the phase mask. Phasemask/PDMS thin layer composite is released in 5 w% NaOH solution in a day.

5.2.3 *Microfluidic Device*

As shown in Figure 5.1, the PDMS phase mask comprises the bottom wall of the microfluidic device. A microfluidic device whose height is 50-75 μm and width 1-5 mm comprises the top of the device. Devices were fabricated by cutting out the PDMS channel using a scalpel, punching a hole at one end to make an inlet for the entering fluid and carving out a reservoir at the other end to collect the 3-d structures. The PDMS devices were then plasma sealed to the phase mask after placing thin sacrificial layers of PDMS on the channel alone and on the region of the phase mask which sits right under the channel. This is to ensure that the oligomer was exposed only to non-plasma treated PDMS surfaces while ensuring that the device is still effectively sealed.

5.2.4 *Stop-Flow-Lithography Setup*

Devices were mounted on an inverted microscope (Axiovert 200, Zeiss) and the formation of the structures was visualized using a CCD camera (KP-M1A, Hitachi). Flows in the microfluidic device are driven using a controlled pressure source. To generate controlled pressure in the range of 0-15 psi, a compressed air source (~40 psi) in the laboratory was first connected to a Type 100 LR manual pressure regulator (Control Air). Downstream of the regulator, a 3-way solenoid valve (Burkert) was used to switch rapidly between atmospheric pressure (stop) and the input pressure (flow). The output from the 3-way valve was connected to the microfluidic device using Tygon tubing connected to a 10 μl pipette tip (Biosciences). The pipette tip was filled with the desired fluid and inserted into the inlet hole punched in the microfluidic device. The transducer, 3-way valve and shutter were all controlled using VIs written in Labview 8.1 (National Instruments). The 3-way valve was controlled using a 1024-HLS digital I/O board (Measurement Computing) and a relay. The transducer and the shutter were controlled using serial connections.

5.2.5 *Photopolymerization Setup - Hg lamp*

A 100W HBO mercury lamp served as the source of UV light. An i-line filter (Omega Optical) was used to provide 365.5 nm UV light. Light was collimated by passing the unfocused beam (no objective in place) from the microscope through a 30 cm long, 1 cm diameter, hollow metallic tube that was blackened on the insides. Light intensity was measured to be 5 mW/cm^2. A VS25 shutter system (Uniblitz) driven by a computer controlled VMM-D1 shutter driver provided specified pulses of UV light. Typical exposure times used were 10-40s. If required, photomasks designed in AUTOCAD 2005 and printed using a high resolution printer at CAD Art Services (Bandor, OR) were inserted into the field-stop of the microscope.

5.2.6 *Photopolymerization Setup - 390 nm Laser*

Pulses of 60 fs from the frequency doubled output of a Ti:sapphire laser operating at 390 nm and a repetition rate of 250 kHz were used.

5.2.7 *Oligonucleotide Incorporation*

For hybridization experiments, we used monomer solutions of 2:1 PEGDA:TE Buffer (10mMTris pH 8.0 (Rockland), 1mMEDTA (OmniPur)) with 1 % initiator and a DNA oligomer probe at a concentration of 50 μM. Oligomer probes (IDT) came modified with a reactive Acrydite group

and 18-carbon spacer (Probe ♯1: 5Acrydite-C18ATA GCA GAT CAG CAG CCA GA-3, Probe ♯2: 5Acrydite-C18CAC TAT GCG CAG GTT CTC AT-3).

5.2.8 Oligonucleotide Detection

Particles were pipetted into separate PDMS reservoirs for each hybridization experiment. Complementary target DNA oligomers modified with a Cy3 fluorophore (IDT) were suspended at a concentration of 1 μM in hybridization buffer (TE buffer with 0.2M NaCl (Mallinckrodt) and 0.5% sodium dodecyl sulfate (SDS, Invitrogen)). Solutions of target oligomer were pipetted into the appropriate reservoirs and the particles were incubated for 10 min at room temperature. The particles were then rinsed several times with TE buffer and visualized using an orange longpass filter set (XF101-2, Omega), which is compatible with both rhodamine B and Cy3 fluorophores. Still images were captured using a Nikon D200 digital camera.

5.3 Results

5.3.1 Device Construction

The setup used for SFIL is shown in Figure 5.1. The microfluidic device and the phase mask, both molded in PDMS, are sealed to each other as shown in the cross-sectional view in Figure 5.1a. A protective layer of PDMS is spin-coated on the phase mask in order to prevent the liquid oligomer from filling up the interstitial spaces in the phase mask. When this protective layer is absent, the interference pattern from the diffraction is not formed. This is because of the absence of air in the interstitial spaces, which provides the refractive index difference required for the interference pattern formation when light traverses through the phase mask. We have used microfluidic devices with a lateral dimension of 1mm-5mm to synthesize both larger millimeter sized structures as well as arrays of micron-sized particles.

The integrated device is placed on a microscope stage and collimated light is provided either from a laser or by the passage of unfocussed UV light through a blackened, hollow metallic tube. A mask containing the shape of the desired structure is placed in the field stop of the microscope or in the path of the laser to form defined 2-D structures (Figure 5.1b). Liquid PEG-DA oligomer containing photoinitiator flows through the microfluidic device as described in the Experimental Section. PEG based hydrogel polymers, with their porous properties and the minimization of non-specific binding, are well suited for use in biological applications. Here we illustrate the method by forming equilateral PEG triangles with a side of 120 μm. The particles are formed in a stationery layer of oligomer film using an exposure dose of 300 ms and then flushed out into a reservoir. DIC images of the structures formed are shown in Figure 5.1c. The square 2 μm phase-mask induced pattern is clearly visible on the faces of the triangular particles.

5.3.2 Structural Characterization

SEM images of the structures formed are shown in Figure 5.2. The top view of the structure shows a repeating array of posts. The cross-sectional view shows elements of a 3-D structure (Figure 5.2b). Because the registry of the interference pattern occurs simultaneously with photocrosslinking [96], we find that the structures do not show full 3-dimensionality. We believe that the hydrogel materials

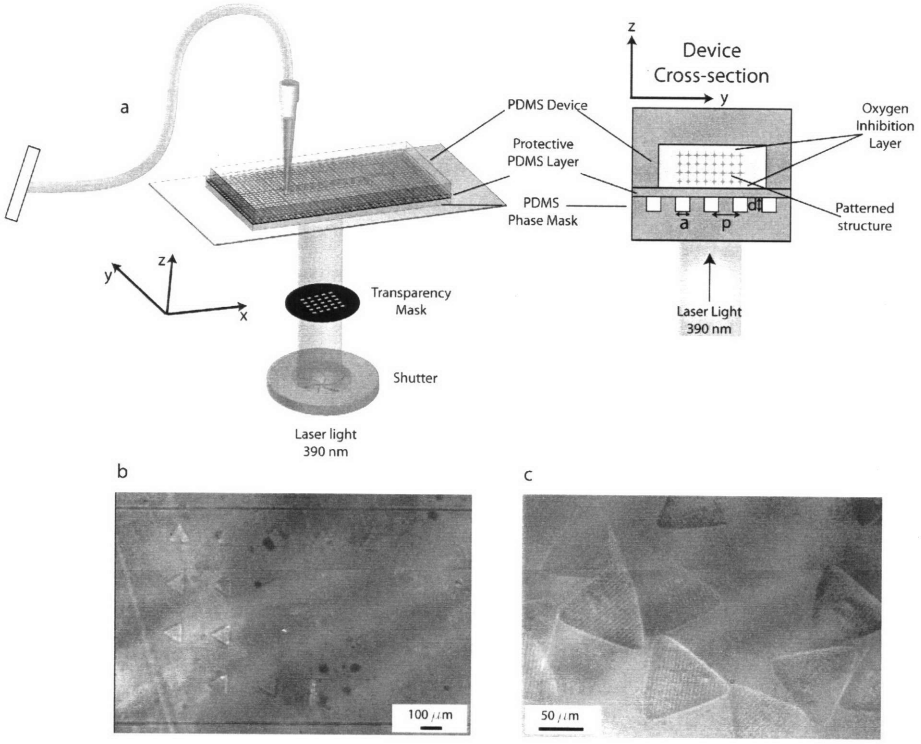

Fig. 5.1: *SFIL Experimental setup. a)Schematic figure showing the PDMS microfluidic device attached to a PDMS phase mask. Shuttered and transparency mask defined light from a pulsed laser or from a Hg lamp enters through the phase mask and into the stationary oligomer film that is contained in the microfluidic device. This results in the formation of an array of transparency mask-defined structures each of which contains a 3-d pattern defined by the phase mask. The 3-d structure is shown in the cross-sectional view on the right hand side. The patterned particles are flushed out and the flow is stopped before another array of particles is formed. [94] In our setup, the phase mask is protected from the liquid oligomer by a thin spin-coated layer of PDMS. The size of the posts in the phase mask used in our work is d = 1 μm, a = 2 μm and p = 2 μm. b)Brightfield image of an array of patterned triangles of side 120 μm formed in a 1000 μm wide and 30 μm tall microfluidic device. The granularity in the background is caused by the phase mask.c)DIC image of the triangles shown in b) after they have been developed in ethanol. The patterned grid-like structure formed by the phase mask is visible on the surface of the particles.*

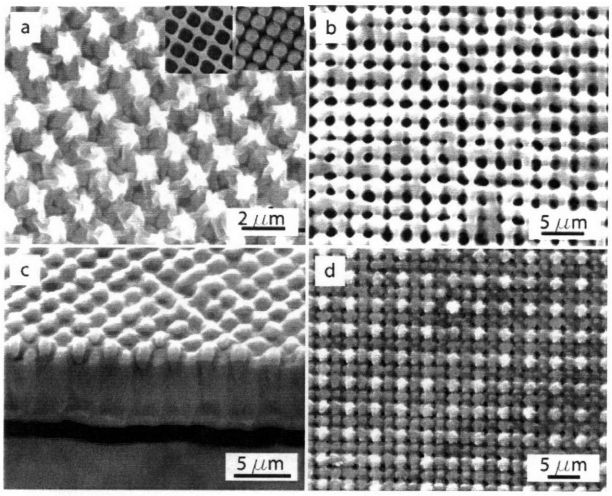

Fig. 5.2: *SEM Images of the patterned particles. All structures were formed using the phase mask shown in the inset of a). a)Image of a shrunk PEG-DA structure. Such structures are typically formed at low exposure times when cross-linking is not sufficient to form posts. b)Image of a membrane like structure. c)Cross-sectional view of the structure. d)Image of a 3-d structure*

used need to be further optimized to achieve full 3-dimensionality. Images of the phase mask used to synthesize the structures are shown in the inset.

5.3.3 Gradient Structure

One of the important advantages of laminar flow in microfluidic devices is that it permits the creation of chemical anisotropy in flowing liquids. The flow can be homogenized only by the slow process of diffusive mixing since convective mixing is negligible at these length scales. Several applications of this chemical confinement phenomena have been reported including the synthesis of chemically inhomogeneous particles. [38,49]One unique advantage of combining IL with micofluidics is the synthesis of such chemically inhomogeneous 3-D structures. We show the synthesis of a structure with a simple chemical gradient created by coflowing parallel streams of water and PEG-DA.

5.3.4 Increase in Signal Intensity

One of the most promising uses of polymeric particles is for sensing and diagnostic applications. [13] In such applications, a probe molecule on the surface of the particle first binds to a target fluorophore molecule in solution. The particles are then washed to remove unbound fluorescent target molecules. The concentration of the target in solution can be inferred by reading the intensity of the fluorescent signal on the surface of the particle. The sensitivity of such particle detection

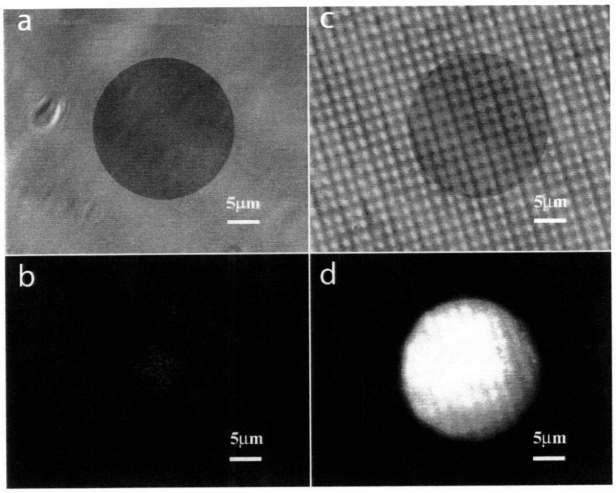

Fig. 5.3: *Increased detection sensitivity provided by patterned structures over unpatterned structures. a)Brightfield optical image of a flat hydrogel structure formed without IL b)Image of the region shown in a)taken using a fluorescence microscope. The signal shown is very weak because of the low density of probe molecules on the surface of the particle c)Brightfield image of a patterned structured formed using IL d)Fluorescent image of the structure seen in c) shows a high signal at the same conditions seen in b) because of the high density of probe molecules on the surface. In b) and d), the field stop aperture has been closed down to collect signal from a small circular portion of the structure.*

assays is critically dependent on the number of probe molecules that are present on the surface of the particle. Increasing the surface area of the particles by creating intricate patterned networks on the surface enables the synthesis of particles with extremely high surface area to volume ratios.

We first formed probe DNA molecules containing 500 μm diameter, 50 μm tall disk shaped hydrogel particles (Figure 5.3) using both IL and regular SFL. The particles were hybridized with target DNA molecules and then washed to remove unbound target. We find that the use of IL permits a multi-fold increase in intensity compared to the control particle. This would be very helpful in greatly increasing the sensitivity of particle assays.

5.4 Conclusion

In this work we have shown that performing interference lithography in a flow through microfluidic device offers several advantages. By synthesizing structures in hydrogel polymers that are not amenable to being spin-coated we are able to expand the range of materials available to interference lithography. The use of stop flow lithography permits the high throughput synthesis of mask-defined structures whose length scales stretch across three orders of magnitude. A wide range of materials such as stimuli-responsive polymers, biocompatible polymers, polymer-nanoparticle composites etc, can now be used for particle structure formation at the micron scale. We show that the high

surface area/volume ratio of the structures formed may be used to generate high fluorescent signal intensity that could benefit a variety of sensing and diagnostic applications. Further, by exploiting the diffusion-limited mixing seen on the micron scale, we can synthesize 3-D structures that possess gradients in their mechanical or chemical properties. Such structures may be especially useful in applications such as tissue engineering where controlled anistropy at multiple length scales is known to have a profound effect on cell growth and viability. Optimizing the materials used could result in the formation of 3-D colloidal particles by disconnecting the structures after formation. [97]

CHAPTER 6

Stop Flow Lithography

6.1 Introduction

This chapter builds off the continuous flow lithography (CFL) [38],technique described in Chapter 3. We describe a new setup that uses compressed air driven flows in preference to syringe pumps to synthesize particles using a technique that we call stop-flow lithography (SFL). A flowing stream of oligomer is stopped before polymerizing an array of particles into it, providing for much improved resolution (down to 1 μm) over particles synthesized in flow. The formed particles are then flushed out at high flow rates before the cycle of stop-polymerize-flow is repeated. The high flow rates enable orders-of-magnitude improvements in particle throughput over CFL. However, the deformation of the PDMS elastomer due to the imposed pressure restricts how quickly the flow can be stopped before each polymerization event. We have developed a simple model that captures the dependence of the time required to stop the flow on geometric parameters such as the height, length and width of the microchannel, as well as on the externally imposed pressure. Further, we show that SFL proves to be superior to CFL even for the synthesis of chemically anisotropic particles with sharp interfaces between distinct sections.

6.1.1 Limitations of CFL

In CFL, shuttered pulses(30-100ms) of mask-defined UV light are flashed into a stream of oligomer flowing through a PDMS microchannel. The exposed portions of the oligomer are crosslinked

by exposure to this light, leading to the formation of solid structures almost instantaneously. The structures formed are then able to advect through the continuously flowing polymer precursor liquid that surrounds them. This is because of the oxygen-induced inhibition [55] of polymerization at PDMS surfaces. During the polymerization process, oxygen diffuses in through the porous PDMS walls and reacts with free radicals, converting them to chain-terminating peroxide species. This results in the formation of a thin uncrosslinked, lubricating layer of oligomer near the PDMS walls that enables the particles to flow without sticking to the walls of the device.

However, because particles are synthesized in flow and exposed to finite pulses of UV light, they are smeared when high oligomer flow rates are used. In order to achieve a given particle resolution, there is therefore a limit to the maximum flow rate that can be used. This imposes restrictions on the particle throughput that can be achieved, a problem that is accentuated as particle size is decreased. There is a great need for the synthesis of complex particles at the colloidal length scale for applications such as drug delivery [98] or to achieve self-assembly by exploiting thermal forces [12]. With CFL, it is difficult to form such particles and throughput is a concern even for larger particles. The limitations of CFL arise from the fluidics and not the optics. Using i-line (365nm) photolithography, features down to 400nm can be achieved [99] provided high-quality photomasks and a stationery, non-flowing substrate are available.

In this article, we describe how we have overcome some of the above problems to form high resolution particles in a high throughput manner using a technique we call stop-flow lithography (SFL). Particles are formed in a stationery layer of monomer sandwiched inside a PDMS microchannel before being flushed out, the process being repeated in a cyclical manner.

6.1.2 Deformability of PDMS

In order to perform SFL, it is vital to have a microfluidic system that responds rapidly to changes in pressure in order to switch frequently between stop and flow mode. We have devised a setup that uses compressed-air driven flows in preference to syringe pumps because of their improved dynamic response. However, the flow still takes a finite time to stop and start because of the deformation of the PDMS elastomer due to the imposed pressure. The deformation of PDMS has previously been exploited to design pressure-actuated valves [100], peristaltic pumps [101] and pressure sensors [102] among other applications. However, in several other situations, the deformation of PDMS may be undesirable, causing sagging of channels [103], increasing Taylor dispersion or simply diverging from predictions on flow profiles and mass transfer that have been made for rectangular cross-sections. Being the material of choice for numerous microfluidic applications, it is essential to characterize the effect of the deformation of PDMS on flow properties within microchannels.

The altered flow profile created at steady state by the bulging cross-section of rectangular PDMS devices has been studied in detail [104]. However, the dynamic response of the PDMS to an imposed pressure profile and its dependence on channel geometry and the imposed pressure are yet to be investigated. This dynamic response is of crucial importance in applications where the flow must be stopped and started frequently while also being important to predict when steady state will be achieved in continuous flow applications. In addition to describing the setup that we have devised to perform SFL, we have developed scaling relations to describe the effect of channel geometry on the dynamic response of the PDMS to changes in external pressure. Along with improved resolution, we show that operating the process in a stop-flow mode has the further advantage of increased throughput over CFL. Finally, we describe how SFL is superior to CFL when forming

multifunctional particles with sharp interfaces.

6.2 Theory

The model described in this section involves a coupling between the fluid mechanics of oligomer flow and the elasticity of the PDMS device used. We start with a description of the channel geometry and then proceed to separately model the deformation of the PDMS microchannel and the lubrication flow created by the oligomer flowing through the PDMS device. The elasticity and flow problems are then coupled to provide a description of the squeeze flow that determines how rapidly the PDMS responds to changes in external pressure.

6.2.1 Microchannel Geometry

We use PDMS microchannels bearing rectangular cross-sections that are sealed to a glass slide spin-coated with PDMS (Figure 6.1). In such devices, the top wall is a deformable layer of PDMS (Young's modulus, E $\simeq$ 1 MPa [104]) that is several millimeters thick. Since the bottom wall of the device is a very thin layer of PDMS that is attached to a rigid glass slide (E = 62 GPa), its deformation can be neglected when compared to the top wall.

6.2.2 Modeling Elasticity of PDMS

We start by assuming that Hooke's law can be used to model the stress-strain relationship in PDMS giving $\varepsilon = \sigma/E$, where ε is the strain, σ is the stress and E is the Young's modulus of PDMS. The stress experienced by the PDMS is proportional to the applied external pressure. An appropriate length scale is required to calculate the strain. Because the PDMS device is several millimeters thick and the channel is only a few microns tall, the PDMS can be considered a semi-infinite medium where strain vanishes at large distances from the channel. In such cases, the appropriate length scale for the strain in the z-direction is given by the channel width, W, and not the the thickness of the PDMS device or the channel height [105]. We therefore have the deformation of the channel ceiling, Δh, being proportional to the channel width, local pressure and Young's modulus as given by

$$\varepsilon \sim \frac{\Delta h}{W} \sim \frac{P}{E} \tag{6.1}$$

As discussed in earlier work [104], the deformation of the PDMS channel in the lateral direction (y-direction) can be neglected because it is in turn proportional to the height, H, which is much smaller than the width ($W/H \gg 1$) in all the experiments presented here.

The deformation in the height of the channel at any point is proportional to the local pressure according to Equation 6.1. Since the pressure decreases along the length of the channel, there is a commensurate decrease in PDMS deformation along the length of the device. The maximum deformation is observed at the entrance to the channel and is given by

$$\Delta h_{max} \sim \frac{PW}{E} \tag{6.2}$$

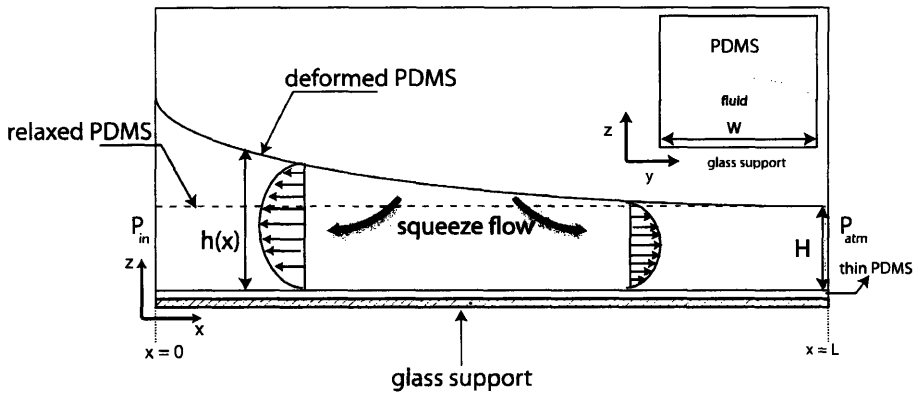

Fig. 6.1: *Schematic showing the deformation of the PDMS microchannel (shown in white). The flow of the monomer (grey) is initially from left to right, the pressure being highest at the entrance and reaching atmospheric pressure at the outlet. The maximum PDMS deformation is thus at the leftmost point of the channel and the minimum deformation is at the rightmost point. The figure is a 2-dimensional representation of the channel where the height shown at any point, $h(x,t)$, has been averaged across the width of the channel (the y-dimension). The variation in height across the width is seen in a cross-sectional view of the channel that is shown in the inset on the top right of the figure. The deformed PDMS channel relaxes back to its original state, shown as a dashed line, when the pressure is turned off. This relaxation causes an asymmetric squeeze flow that drives monomer out to the left and the right. The bottom of the device is undeformed because of the rigid glass slide that supports it.*

6.2.3 Modeling Fluid Flow

The three-dimensional problem of fluid flow through a rectangular cross-section can be reduced to two dimensions by averaging the height of the deformed PDMS channel, $h(x, y)$, across the width of the channel at any cross-sectional interface along the length of the device to get $h(x, t)$ alone as shown in Figure 6.1. For the creeping flow ($Re \ll 1$) of fluid through a thin channel ($H/L \ll 1$), the flow is mainly in the x-direction and the lubrication approximation can then be used to reduce the Navier-Stokes equation to,

$$\frac{\partial P}{\partial x} = \mu \frac{\partial^2 v_x}{\partial z^2} \tag{6.3}$$

Here μ is the viscosity of the oligomer. No-slip boundary conditions are imposed at the top and bottom walls. The continuity equation couples v_x and v_z, enabling us to calculate v_z.

$$\frac{\partial v_x}{\partial x} + \frac{\partial v_z}{\partial z} = 0 \tag{6.4}$$

The boundary conditions for v_z are dictated by the rigid bottom wall and the flexible top wall.

$$v_z(z = 0) = 0 \tag{6.5}$$

$$v_z(z = h(x, t)) = \frac{\partial h}{\partial t} \tag{6.6}$$

Here, we have assumed that the curvature of the PDMS top wall is small in relation to the length of the device ($\Delta h_{max}/L \ll 1$) from which it follows that the velocity of the retracting membrane is only in the negative z-direction. Integrating Equation 6.3 and using the associated boundary conditions, we get

$$v_x = \frac{1}{2\mu} \frac{\partial P}{\partial x} [z^2 - z h(x, t)] \tag{6.7}$$

6.2.4 Coupling of Elasticity and Flow

When an external pressure is first imposed, the rectangular cross-section of the PDMS device bulges as shown in the inset of Figure 6.1. When the pressure is turned off, the elasticity of the PDMS forces the microchannel to retract back to its original rectangular cross-section, setting up a squeeze flow that drives excess fluid out of the device. The squeeze flow is asymmetric, driving more fluid towards the entrance of the channel than out through the exit. The flow continues until all the excess fluid is driven out and therefore has a characteristic timescale, τ_r, associated with it. In this work, we are concerned with how τ_r is affected by the material properties of the PDMS and the oligomer, channel geometry and the imposed pressure.

In elastohydrodynamic problems such as this one, the deformed PDMS exerts a pressure on the fluid confined within the channel [106]. For small deformations, the pressure exerted on the fluid at any point along the channel can be assumed to be proportional to the strain in the PDMS at that point as given by Equation 6.1. The appropriate length scale for the strain is again the width, W. The pressure at any point, x, is then given by

$$P(x, t) = E \frac{\Delta h(x, t)}{W} = E \left(\frac{h(x, t) - H}{W} \right) \tag{6.8}$$

where H is the undeformed height of the channel. Differentiating Equation 7.6, we get

$$\frac{\partial P}{\partial x} = \frac{E}{W}\frac{\partial h}{\partial x} \tag{6.9}$$

Using Equations 7.5 and 7.7, we now have

$$v_x = \frac{E}{2\mu W}\frac{\partial h}{\partial x}(z^2 - zh(x,t)) \tag{6.10}$$

Using Equation 7.3 to evaluate v_z, we get

$$v_z = -\int_0^z \frac{\partial v_x}{\partial x}\, dz \tag{6.11}$$

Using Equation 7.8 and 7.9, we can now evaluate v_z at $z = h(x,t)$ and equate it to the instantaneous velocity of the deforming membrane using Equation 6.6 to get

$$\frac{\partial h}{\partial t} = \frac{h^2 E}{4\mu W}\left[\left(\frac{\partial h}{\partial x}\right)^2 + \frac{h}{3}\frac{\partial^2 h}{\partial x^2}\right] \tag{6.12}$$

We thus have a differential equation that describes $h(x,t)$. While a full solution to Equation 7.12 can be obtained only using numerical techniques, a simple scaling analysis reveals some insights into the problem. In the analysis that follows, we assume that channel deformation is small in comparison with channel height ($H \gg PW/E$). We first note that the scales for the height of the channel, $h(\sim H)$, and the deformation of the channel, $\partial h(\sim PW/E)$, differ from each other. The scales for the other variables are $x(\sim L)$ and $t(\sim \tau_r)$ where the response time, τ_r, remains to be determined. For each of the three partial derivatives in Equation 7.12 we then obtain the following scalings

$$\frac{\partial h}{\partial t} \sim \frac{PW}{E\tau_r} \tag{6.13}$$

$$\left(\frac{\partial h}{\partial x}\right)^2 \sim \left(\frac{PW}{EL}\right)^2 \tag{6.14}$$

$$h\left(\frac{\partial^2 h}{\partial x^2}\right) \sim H\frac{PW}{EL^2} \tag{6.15}$$

Substituting these scalings into Equation 7.12 we get

$$\frac{1}{\tau_r} \sim \frac{H^2 E}{4\mu W L^2}\left[\frac{PW}{E} + \frac{H}{3}\right] \tag{6.16}$$

The first term inside the brackets on the right-hand side of Equation 7.14 can be neglected provided $H \gg PW/E$, which is exactly what we had assumed at the outset. Under these conditions we see that

$$\tau_r \sim \frac{\mu L^2 W}{EH^3} \tag{6.17}$$

We note from Equation 6.17 that the response time is then independent of the imposed pressure. When the pressure is increased to a point that the deformation in channel height, Δh, is comparable to the channel height, H, the scaling for the response time is more complicated because both terms inside the bracket in Equation 7.14 must then be taken into account.

6.2.5 Analytical Solution

An analytical solution to Equation 7.12 can be obtained under certain special conditions. Using again the assumption that the channel deformation is small, we see that the second term in the brackets on the right hand side of Equation 7.12 can be neglected to give,

$$\frac{\partial h}{\partial t} = \frac{h^3 E}{12\mu W}\left(\frac{\partial^2 h}{\partial x^2}\right) \tag{6.18}$$

We now define $\theta = h/H$, $\tau = H^3 Et/12\mu W L^2$ and $\xi = x/L$ to get

$$\frac{\partial \theta}{\partial \tau} = \theta^3 \frac{\partial^2 \theta}{\partial \xi^2} \tag{6.19}$$

We now make the further approximation that for small deformations, $\theta = 1 + \varepsilon$ and use the zeroth order term from Equation 6.19 to get

$$\frac{\partial \theta}{\partial \tau} = \frac{\partial^2 \theta}{\partial \xi^2} \tag{6.20}$$

The initial condition for this problem has been calculated previously [104].

$$\theta(0, \xi) = \theta_0(\xi) \tag{6.21}$$

The boundary conditions for this equation are given by

$$\theta(\tau, 0) = 1 \tag{6.22}$$

$$\theta(\tau, 1) = 1 \tag{6.23}$$

which physically imply that the channel height at either end is the undeformed height H. Equation 6.20 has a similarity solution that can be obtained by defining a new variable $\eta = \xi/\sqrt{2\tau}$. The two boundary conditions and the one initial condition are then modified to yield

$$\eta(0) = 1 \tag{6.24}$$

$$\eta(\infty) = \theta_0(\xi) \tag{6.25}$$

The solution to Equation 6.20 is then given as

$$\theta = (\theta_0(\xi) - 1)\mathrm{erf}\left(\frac{\xi}{\sqrt{2\tau}}\right) + 1 \tag{6.26}$$

For illustration, we consider the simple initial condition

$$\theta_0 = 1 - (\xi - 1)\left(\frac{\Delta h_{max}}{H}\right) \tag{6.27}$$

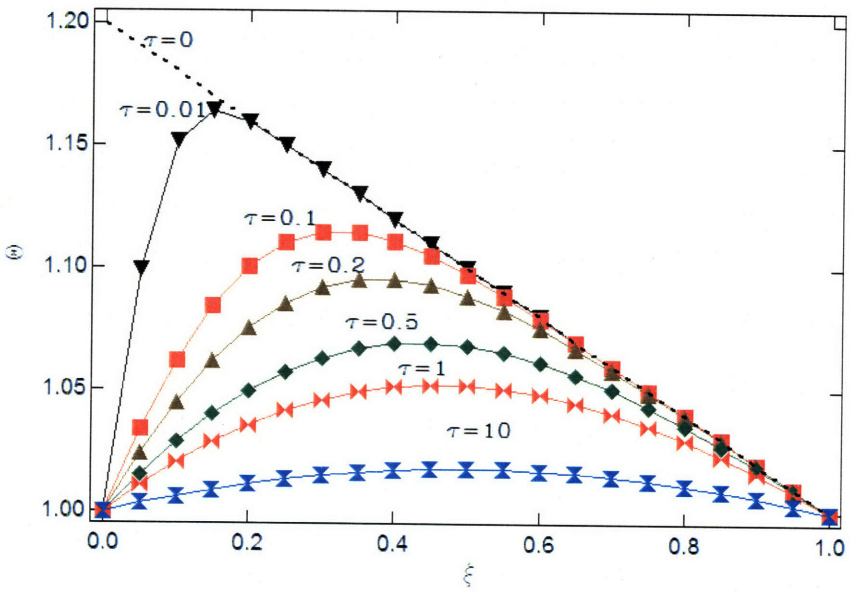

Fig. 6.2: *Position in time of the retracting channel top wall. This plot shows the change in dimensionless channel height with change in dimensionless time. Initially, the channel has been assumed to have a linearly deformed profile with* $\Delta h_{max} = 0.2H$. *Channel height is plotted as a function of channel length for times ranging from 0.01 to 100. As seen, the channel height collapses to 1 at both the entrance and exit of the channel immediately. The maximum channel varies with both channel length and time.*

which indicates a linearly deformed channel. The solution to Equation 6.20 is then

$$\theta = (1-\xi)(\frac{\Delta h_{max}}{H})\text{erf}\left(\frac{\xi}{\sqrt{2\tau}}\right) + 1 \tag{6.28}$$

When plotted as a function of ξ for different values of τ, channel height varies as shown in Figure 6.2.

As seen in Figure 6.2, channel height varies with both position and time. At any given time point, there is a maxima in channel height and the position of this maxima changes with time, moving gradually towards the center of the channel. The squeeze flow in this problem is symmetric about this point resulting in a stagnation point in the middle of the channel where no flow is observed. This result has been verified experimentally as we have observed a moving stagnation point after the pressure input to the channel has been turned off. We also see that the model predicts that the channel height at the entrance drops immediately to the undeformed channel height which is also observed experimentally.

6.3 Experimental Methods

6.3.1 Microfluidic Devices

Devices were fabricated by pouring polydimethylsiloxane (PDMS, Sylgard 184, Dow Corning) on a silicon wafer containing positive-relief channels patterned in SU-8 photoresist (Microchem). The thickness of the PDMS devices was always maintained to be 5mm or greater. For the work shown in Figures 2-6, straight channels with a rectangular cross-section and variable widths, lengths and heights were used as required. For Figure 6.8, trident-shaped rectangular channels that were 300 μm in width and 40 μm in height were used.

Devices were fabricated by cutting out the PDMS channel using a scalpel, punching a hole at one end to make an inlet for the entering fluid and carving out a reservoir at the other end to collect the particles. The PDMS devices were then plasma sealed to glass slides spin-coated with PDMS after placing thin sacrificial layers of PDMS on the channel alone and on the region of the glass slide which sits right under the channel. This is to ensure that the oligomer was exposed only to non-plasma treated PDMS surfaces while ensuring that the device is still effectively sealed. Devices were mounted on an inverted microscope (Axiovert 200, Zeiss) and the formation of the microparticles was visualized using a CCD camera (KP-M1A, Hitachi). Video recordings of bead flow and particle formation were recorded at 30 frames/second onto a video tape recorder (DSR-25, Sony) for processing. Still images were captured and processed using NIH Image software or a digital camera (D200, Nikon) and Nikon Capture software.

6.3.2 Materials

In all experiments, the oligomer used was poly(ethylene glycol)(400) diacrylate (PEG-DA, Sigma Aldrich). For the experiments in Figures. 6.4 and 6.5, a 1% solution of 1.57 μm PMMA beads in PEG-DA was used. For the experiments in Figures. 6.6 and 6.7, the polymer precursor mix used was a 1% (w/v) solutions of the photoinitiator Phosphine oxide phenyl bis (2,4,6-trimethyl benzoyl)(Irgacure 819, Sigma Aldrich) in PEG-DA. For the experiments in Figure 6.8, a 0.005 wt.% solution of the fluorescent monomer Methacryloxyethyl thiocarbamoyl rhodamine B (Polysciences) in PEG-DA was used as the fluorescent stream. PEG-DA is reported by the manufacturer to have a viscosity of 56 centipoise at 25°C.

6.3.3 Stop-Flow-Lithography Setup

The setup for SFL requires the use of pressure provided by a compressed-air source to drive flow inside the microfluidic channels (Figure 6.1). To generate controlled pressure in the range of 0-15 psi, a compressed air source (~70 psi) in the laboratory was first connected to either a T3510 I/P transducer (Marshbellofram) or a Type 100 LR manual pressure regulator (Control Air). Downstream of the transducer/regulator, a 3-way solenoid valve (Burkert) was used to switch rapidly between atmospheric pressure (stop) and the input pressure (flow). The output from the 3-way valve was connected to the microfluidic device using Tygon tubing connected to a 10 μl pipette tip (Biosciences). The pipette tip was filled with the desired fluid and inserted into the inlet hole punched in the microfluidic device. The transducer, 3-way valve and shutter were all controlled using VIs written in Labview 8.1 (National Instruments). The 3-way valve was controlled using a 1024-HLS digital I/O board (Measurement Computing) and a relay. The transducer and the

shutter were controlled using serial connections. A movie showing the formation of particles in real-time is shown in the Supplementary Information (Movie1.mpg). The experiment shown was performed using a channel of width 200 μm, height 20 μm and length 1cm. The input pressure was 6 psi, $t_{stop} = 0.3$s, $t_{polymerize} = 0.1$s and $t_{flow} = 0.2$s.

6.3.4 Bead Tracking

A dilute solution of PMMA beads in PEG-DA (see Materials section) was used to track the squeeze flow. After a given pressure profile was supplied, beads in the mid-plane of the channel (z=H/2 in Figure 6.1) were followed with a 20X or 40X microscope objective (Zeiss) with an optivar setting of 2.5X leading to effective magnifications of 50X or 100X respectively. Movies of translating beads were recorded on to a video tape recorder (DSR-25, Sony) using a CCD camera that captured images at the rate of 30 frames/second using an exposure time of 1/500s. The frame-to-frame position of beads was measured as they moved across the screen using macros written in NIH Image. Bead velocities were calculated from the displacement of the beads using the central difference approximation. Bead tracking was always performed at the exit of the channel to ensure consistency in experiments. Bead tracking was always performed at the exit of the channel to ensure consistency in experiments. Beads that were close to the center of the channel (y = W/2 in Figure 6.1) were chosen to avoid wall effects.

6.3.5 Photopolymerization Setup

Photomasks were designed in AUTOCAD 2005 and printed using a high resolution printer at CAD Art Services (Poway, CA). Each mask was inserted into the field-stop of the microscope to be used for projection photolithography. A 100W HBO mercury lamp served as the source of UV light. A filter set that provides wide UV excitation (11000v2: UV, Chroma) was used to select light of the desired wavelength and a VS25 shutter system (Uniblitz) driven by a computer controlled VMM-D1 shutter driver provided specified pulses of UV light. Typical exposure times used were 30-100ms and pressures ranged from 0.05 to 15 psi. A reservoir was cut in the PDMS to collect the particles.

6.4 Results

In microfluidic devices, fluid flows are commonly driven using syringe pumps. In displacement-driven flows such as these, the compression of the fluid in the tubing external to the microfluidic device causes transients that can be several minutes or longer for micron-scale systems [2]. Due to this effect, compressed-air driven flows are preferable in applications where a rapid dynamic response is desired [2,107]. While they eliminate transients that are associated with the compression of fluid in the tubing outside the microfluidic device, air-driven flows still lead to finite transients associated with the deformation of the PDMS device.

In SFL (Figure 6.3.3), three distinct steps - stop, polymerize and flow - are repeated in a cyclical fashion. In the first step, the pressure-driven oligomer flow through the device is stopped by switching from a specified input pressure to atmospheric pressure using the 3-way solenoid valve. The flow takes a finite time to stop as the PDMS retracts from its bulged state back to its rectangular cross-section (Figure 6.1), squeezing fluid out of the device. In the second step, an array of particles is polymerized into the stationary oligomer using UV light by opening the shutter briefly (0.03-0.1s). In the third step, the particle array is flowed out by switching the 3-way valve

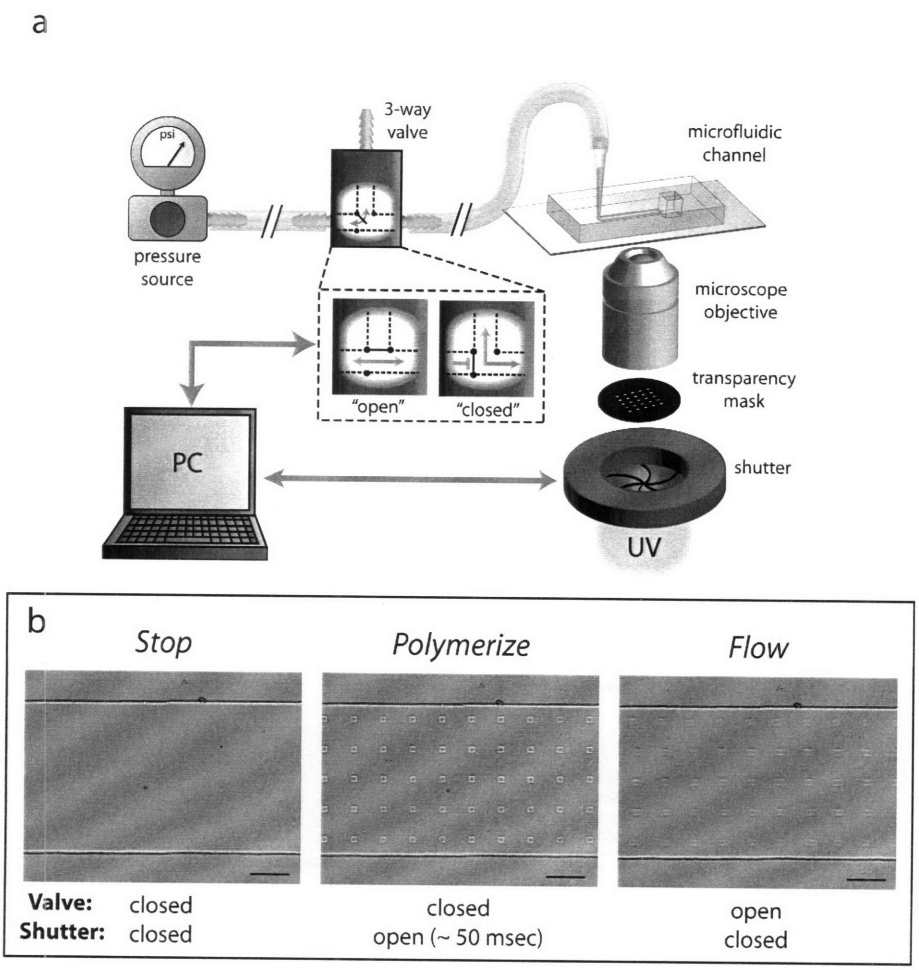

Fig. 6.3: *Stop-flow lithography setup. a)Schematic showing the computer-controlled flow setup. Oligomer flows within a microfluidic channel are driven using a pressure profile provided by a computer controlled 3-way solenoid valve that alternates between atmospheric pressure(closed) and a specified input pressure(open). The computer also controls the exposure time provided by the shutter. b)Microscope images showing the three states of the process. In the first state(stop), the flow is stopped by closing the 3-way valve. In the second state(polymerize), an array of particles is polymerized into the stationery monomer film by opening the shutter for 0.05s while keeping the 3-way valve closed. In the third state(flow), polymerized particles are flushed out of the channel by opening the 3-way valve while keeping the shutter closed. The scalebars shown in b) are 50 μm.*

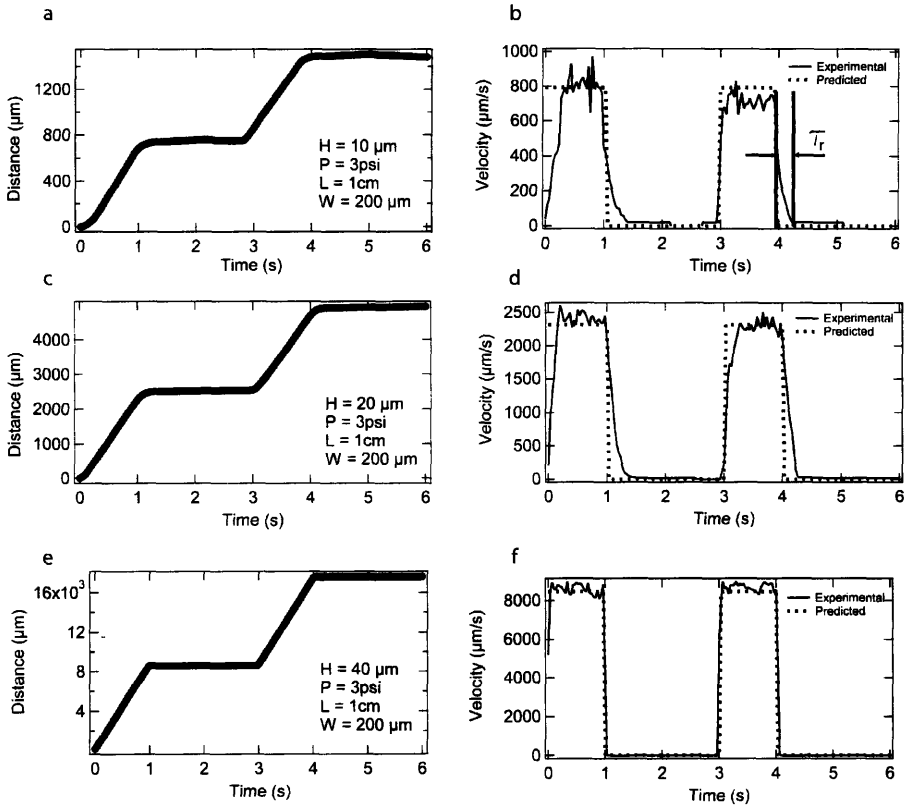

Fig. 6.4: *Tracking of an individual bead in SFL a).c) and e)Plots showing the position in time of a 1.57 μm bead. subjected to a pulsed on-off pressure input profile that is on for a period of 1s and off for a period of 2s. The input pressure is 3psi and the channels used are 200 μm wide and 1cm long. The three plots. a), c) and e) are for channels of heights 10. 20 and 40 μm respectively. b),d) and f)Plots showing the velocity of the beads in a), c) and e) calculated using the central difference method. The dotted lines represent the velocity that is predicted by Equation 6.29. As shown in a), a finite response time is required for the velocity to reach its maximum value in each cycle and to decay from the maximum down to zero. We measure the response time (τ_r) as the time required for the velocity to drop to 1% of its maximum value as shown in b.*

back from atmospheric pressure to the specified input pressure. The three variables to be specified then are the time required to stop the flow ($t_{stop} > \tau_r$), the time required to polymerize particles ($t_{shutter}$) and the time required to flush the particles out (t_{flow}). While $t_{shutter}$ and t_{flow} are easily determined, t_{stop} can be determined only after first estimating τ_r which serves as a lower bound for t_{stop}. We used bead tracking experiments to estimate τ_r as a function of the input pressure and channel geometry. Typical bead tracking experiments that were performed in 10, 20 and 40 μm tall channels are shown in Figure 6.4. A repeating square wave pressure profile comprising two parts - 1s of flow and 2s of stoppage - was applied to the system. In Figures. 6.4a, c and e, we show the position in time of a bead close to the exit of the channel. The bead is shown going through two cycles of stop and flow. The velocity of the bead is the derivative of its position and is shown in Figures. 6.4b, d and f. Also shown in the dotted lines are the predicted maximum velocity, $U(L)$, that one would expect at the exit of a deforming PDMS channel [104].

$$U(L) = \frac{3H^3E}{96W\mu L}\left[\left(1+\frac{PW}{EH}\right)^4 - 1\right] \tag{6.29}$$

A finite response time is required for the bead velocity to attain a steady value after the imposition of an external pressure and for it to drop to zero after the pressure input has been turned off. This finite response is characterized by the curvature of the bead-displacement plots at the junction between the flat and sloped lines in Figures. 6.4a, c and e. The finite response can be seen more clearly in Figures. 6.4b, d and f by measuring the time required for the flow velocity to attain a steady value after it has been turned on or by measuring the time required for the flow velocity to stop after the pressure input has been turned off. For the purpose of this work, response times, (τ_r), were calculated by measuring the time required for bead velocity to fall to 1% of its maximum value.

We first verified the dependence of τ_r on channel height by performing experiments in channels of four different heights 2, 10, 20 and 40 μm with constant width 200 μm and length 1 cm. All experiments were performed at an input pressure of 3 psi. τ_r was calculated for each channel and the results were plotted against channel height. As seen in Figure 6.5a, a power law of -3 is drawn through the experimental data, indicating that the scaling argument in Equation 6.17 compares very well with experiment. As channel height decreases, the sluggishness of the system increases because of the increased resistance to flow that must be overcome to squeeze the fluid out of the channel.

To verify the dependence of response time on channel length, we performed experiments in four channels of length equal to 0.25, 0.5, 1 and 1.2cm, constant width of 200 μm, constant height of 10 μm, all at a pressure of 3 psi. Again, τ_r was calculated for each channel and plotted against channel length. As seen in Figure 6.5b, a power law of 2 is drawn through the experimental data indicating that the scaling argument in Equation 6.17 holds. The resistance to driving a flow also increases with channel length causing larger length channels to show increasing response times.

To verify the dependence of response time on channel width, we performed experiments in four channels of widths 50, 200, 500 and 1000 μm, constant length 1 cm and constant height 20 μm, all at a pressure of 3 psi. The response time is observed to increase linearly with channel width as predicted by Equation 6.17. As width increases, the same deformation produces smaller restoring pressures according to Equation 7.6, resulting in an increased response time.

We also experimentally measured the dependence of τ_r on input pressure as shown in Figure

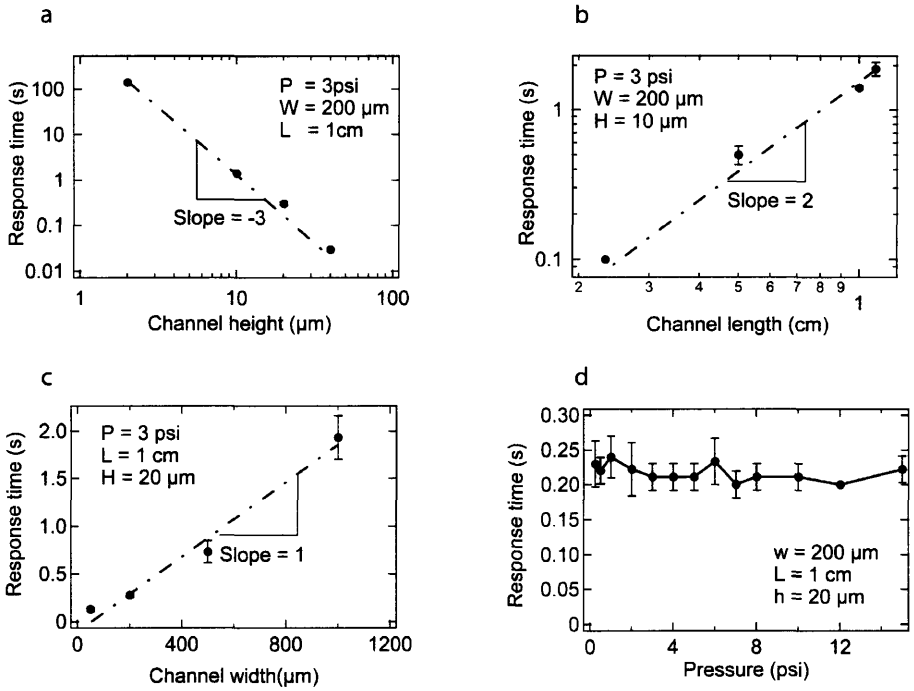

Fig. 6.5: *Plots showing the dependence of τ_r on a)channel height; b)channel length; c)channel width and d)pressure gradient. Dashed lines in a-c) show the power law predicted by Equation 6.17. Our scaling theory predicts that τ_r is invariant with change in pressure.*

6.5d. We see that the response time is invariant to pressure, within the limits that we have tested (up to 15 psi). Larger pressures led to the PDMS-PDMS seal in the device breaking. As predicted by Equation 6.17, this invariance is expected as long as the channel deformation is much smaller than the height of the channel. For the channels used in this experiment (H = 20 μm, W = 200 μm), the pressure at which the channel deformation becomes comparable to channel height ($P \sim EH/W$) is approximately 15 psi.

Increasing pressures cause larger deformations in the channel walls, which in turn increase the elastic driving force that pushes the PDMS back. This increased driving force is counteracted by the fact that a larger volume of fluid must now be driven out. This balance between elastic and viscous forces ensures that response time is independent of pressure for small deformations. Finally, we see that τ_r varies as μ/E. This implies that using less viscous oligomers or making the PDMS devices stiffer, using a higher proportion of curing agent to base for example, will result in smaller response times. In summary, tall channel heights, short channel lengths and channel widths and high pressures (within the limits of mechanical stability) are preferred to obtain rapid dynamic response for device operation in SFL.

6.5 Improved Resolution Compared to CFL

One of the disadvantages of performing photolithography in a flowing stream of monomer is that the structures formed are smeared due to the finite exposure time. For a given resolution, defined as the percent increase in length scale of a particle that can be tolerated, there is an upper limit to the flow velocity that can be used. Increasing the velocity above this limit leads to unacceptable smearing and deformation of the particles formed, while lowering the velocity leads to commensurate decreases in particle throughput. This maximum velocity also decreases with feature size, accentuating the problem of achieving high throughput in CFL.

SFL helps overcome these problems because the oligomer is exposed to light pulses only when it is stationery. To illustrate this advantage, we made particles using the same masks, exposure times (0.05s) and channel heights (10 μm) in both CFL and SFL under conditions that yielded equal particle throughput for both processes (7-30 particles/second depending on the size of the feature size). A comparison of the particles made using SFL versus CFL is shown in Figure 6.6. Shown in the inset of Figures. 6.6a, b and c on the right are the transparency masks used to make the particles.

Concentric square masks of different sizes, where the region between the inner and outer squares was transparent to light were used to make the particles. The dimension described by half the difference between the inner and the outer sides of the concentric squares were 50 μm, 20 μm and 10 μm for the three different particles synthesized. This dimension is referred to as the smallest feature in the particles formed. A 20X objective was used to synthesize all particles in this study leading to a reduction in mask size of ~7.8 times because of a 2.57X lens in the optical train of the microscope($20/2.57 \simeq 7.8$). The smallest features of the particles synthesized were 6 μm(=50/7.8), 2.5 μm (=20/7.8) and 1.25 (=10/7.8) μm which are shown in Figures. 6.6d,f and h respectively. Readily available transparency masks can be printed down to resolutions of $\sim$ 10 μm, where the loss of image quality is already apparent (inset of Figure 6.6c). This imposes a practical limit on the resolution and the feature size of particles that can be made using cheaply available transparency masks in SFL. However, using chrome masks, one may be able to achieve sharp features down to 1 μm. One other factor that must be noted is that hydrogel materials like PEG-DA are not

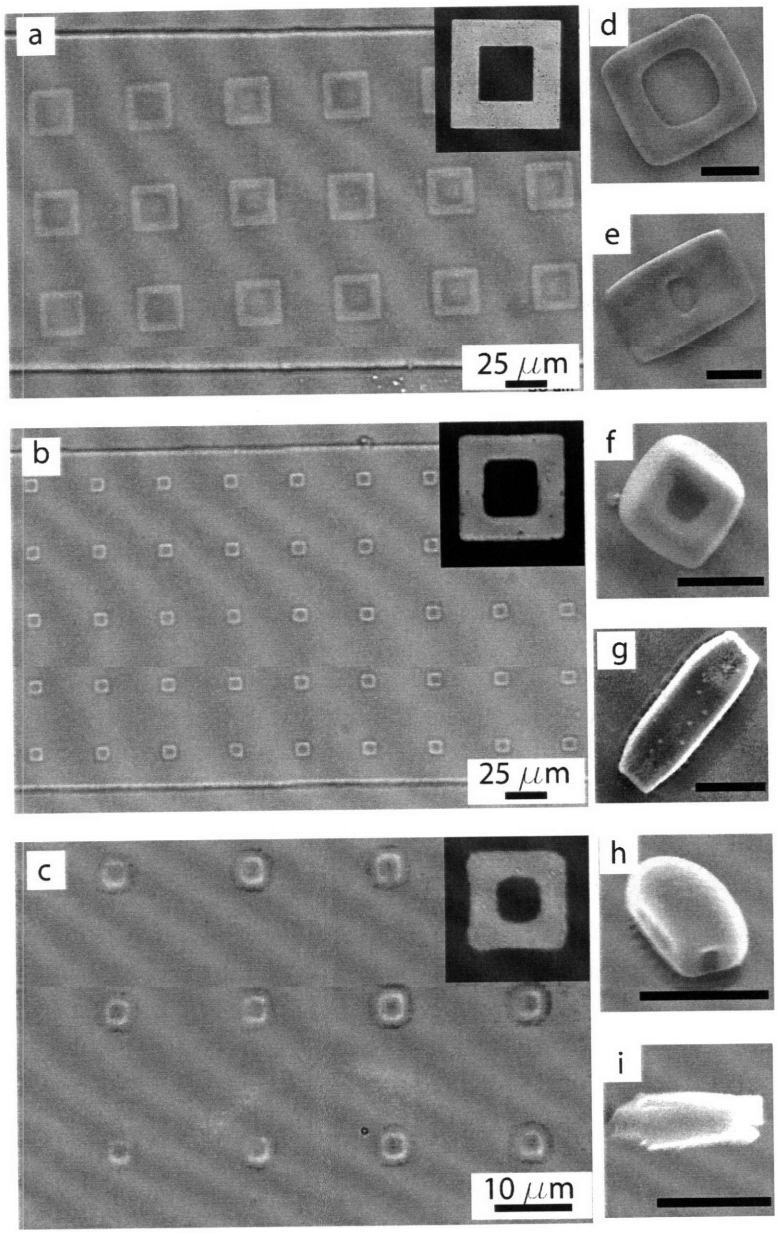

Fig. 6.6: *Particles of three different feature sizes (see definition in text) formed using SFL. All particles were synthesized using a 20X microscope objective and a microchannel that was 200 μm wide, 10 μm tall and 1cm long. In a), b) and c) we show the synthesis, using SFL, of arrays of particles that have feature sizes of 6.25, 2.5 and 1.25 μm respectively. The inset on the top right of a), b) and c) shows the transparency mask that was used to synthesize the particles. In d), f) and h) are SEM images of particles in a), b) and c) respectively. Particles with features down to a micron can be made using SFL. Note that the particles in c) have a high aspect ratio so the particle in h) is on its side. In e), g) and i) we show SEM images of particles made with the same masks using CFL under conditions that yield identical throughput as SFL. The particles are smeared in comparison to the particles formed in SFL and are increasingly deformed as their size decreases. In d-i) the scalebar is 10 μm.*

optimized for use as photoresists. This may impose limitations on the smallest feature size that can be synthesized. We believe that out ability to achieve sharper features is thus limited by the masks and materials we are using as opposed to a fundamental limitation in the process itself.

As seen in Figure 6.6, the particles formed using CFL are blurred beyond recognition even for the largest particles which have a feature size of 6 μm (Figure 6.6e), while those formed using SFL show good resolution at 6 μm and 2.5 μm while the 1.25 μm feature (Figure 6.6h) is visible but not sharp. Considerations of particle uniformity also make SFL more attractive than CFL. In CFL, the deformation of the channels during the formation of particles (Figure 6.1) means that there may be some non-uniformity in the heights of the particles formed because the height of the channel varies with channel length when an external pressure is imposed.

6.6 Increased Throughput

In addition to improved resolution, SFL also provides far greater throughput than CFL. After polymerizing an array of particles, one can flush the particles out at a high velocity, leading to a much greater average flow velocity than in CFL. The maximum throughput (particles/sec) that can be achieved using SFL, T_s, is

$$T_s = \frac{N_p}{t_{stop} + t_{polymerize} + t_{flow}} = \frac{N_p}{\tau_r + \tau_{shutter} + L/v} \tag{6.30}$$

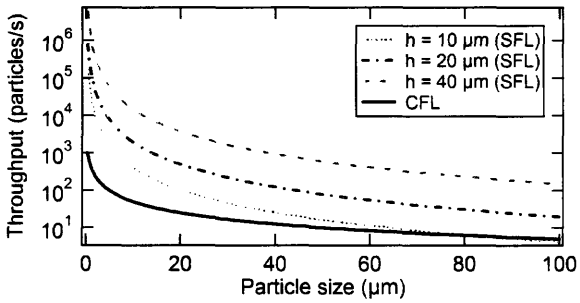

Fig. 6.7: *Particle throughput (particles/sec) as a function of particle size for both CFL and SFL. The curves have been plotted using Equations 7.16 and 7.17. As particle size decreases, SFL offers an increased advantage in throughput over CFL. As channel height increases, SFL throughput increases because of the reduced response time required for the PDMS to equilibrate.*

where N_p is the maximum number of particles that can be polymerized in one exposure and is dependent on the spot size of the objective and the particle size, τ_r is the response time required for the flow to stop, $\tau_{shutter}$ is the time the shutter is left open to polymerize particles, L is the length of the channel full of particles that needs to be flushed out and v is the flow velocity used to flush out the particles. The spot size of the microscope objective used limits the number of particles that can be produced as $N_p \sim D_s^2$ where D_s is the diameter of the spot. For example, we are

currently limited to producing approximately two thousand 10 μm particles per exposure (using a fractional area coverage of 0.2) using a 20X microscope objective that has a spot size one millimeter in diameter. Using the experimentally determined response times, τ_r, for different channel heights, a channel width of 1000 μm and a channel length of 1 cm, the maximum input pressure (P = 15 psi) that safely preserves the stability of seals in the all-PDMS device and an exposure time of 0.05s, we obtained maximum values for T_s that are plotted in Figure 6.7. As channel height decreases, τ_r increases and the velocity that can be achieved using the same pressure decreases, increasing the time required to flow out the particles. The maximum throughput achievable using SFL therefore decreases with a decrease in channel height. In comparison, the maximum throughput achievable using CFL, T_c, is given by

$$T_c = \frac{N_p}{t_{polymerize} + t_{flow}} = \frac{N_p}{\tau_{shutter} + L/v_{max}} \tag{6.31}$$

where all the variables are as defined previously except v_{max} which is the maximum velocity that can be used without compromising on particle resolution and is a function of particle size. For simplicity, we have calculated v_{max} as that velocity which leads to 10% of smearing in the length of the particle parallel to the flow. T_c is also plotted in Figure 6.

As seen in Figure 6.7, SFL can produce orders of magnitude more particles than CFL. The gap between the two processes widens as channel height is increased or particle size is decreased. For example, using only our current simple setup, SFL can produce 3 μm feature particles at the rate of 10^7 per minute in a 40 μm tall channel. This high throughput is achieved by clocking as many as six stop-polymerize-flow cycles in one second. These numbers are much higher than other microfluidic techniques [34–36] that have recently been reported, all of which generate particles at the rate of $10^3 - 10^4$ particles per minute, while not affording the flexibility in particle shape that our process offers. Despite the small spot size of the microscope objective we are using, the throughput also compares well with particle technologies that make use of large area steppers conventionally used for photolithographic applications in the IC industry [108]. Such batch processes are limited to processing one 5" wafer every minute which leads to a throughput of approximately 2.5×10^8 particles ($\sim 3\mu$m in size) per minute. This does not include the time that is required to develop and extract the particles from each individual wafer. Because of the nature of our process, we can perform as many as 300 exposure cycles per minute by rapidly cycling through the stages of stop-polymerize-flow. Particles are then flowed out into a large reservoir where they can be developed and collected in one step at the end. With access to a commercial stepper, we would then be able to achieve a throughput that was at least two orders of magnitude higher than these photolithographic batch processes. Further, our process is unique in allowing us to synthesize particles using materials that cannot be easily spin-coated, enabling the use of a much wider range of materials than traditional photolithographic techniques.

The ability to synthesize large numbers of monodisperse particles in a variety of shapes would help enable fundamental studies in rheology and self-assembly besides being important for the viability of nascent particle-based technologies. [13] The rheology of particle suspensions is very sensitive to particle shape [10] and important in the design of bullet resistant fabrics [109], paints and consumer products. SFL can be used to produce model solutions of precisely defined particles which can be used to characterize the effect of particle shape on rheology. In self-assembly applications, SFL could be use to generate large numbers of complex particles that will serve as building blocks

[12] to induce the assembly of larger structures through Brownian collisions.

6.7 Multi-functional Particles with Sharp Interfaces

One of the unique advantages of flow lithography in microfluidic devices is the ability to exploit laminar flow to polymerize across multiple distinct streams, forming particles with multiple adjacent chemistries [13, 49]. Such particles are finding use in several applications including multiplexed detection [13] and self assembly [49]. When using miscible fluids, the diffusion of species between the streams can deplete the sharpness of the interfaces between adjacent chemistries [110] – an occurrence that is typically undesirable. We demonstrate how SFL can be used to minimize diffusion across streams, improving the sharpness of the interfaces between particles chemistries.

We made tri-functional, striped rods to investigate the interfaces between fluorescent and non-fluorescent particle chemistries when using CFL and SFL (Figure 6.8). We used a channel with three inlets that were connected in parallel to the same pressure source: this eliminates lateral flow and maintains constant stream widths. As such, any 'smearing' of the interfaces between the particle chemistries is expected to result only from diffusion of the fluorescent species between streams.

We made particles that were $\sim 270\mu m$-long, $27\mu m$-wide, and $30\mu m$-deep using an exposure time of $50msec$ in a $40\mu m$-tall channel approximately $200\mu m$ after the stream junction (Figure 6.8a). For particle synthesis using CFL, we chose a flow velocity of $\sim 50\ \mu m/sec$ to limit the expected distortion of the width (during polymerization) to $\sim 10\%$ ($50m/sec \times 0.05sec = 2.5\mu m$) while for SFL, we used a much higher velocity of $\sim 1{,}000\ \mu m/sec$ with a t_{stop} of $50msec$. Because of the small exposure times ($t_{polymerize} = 50msec$) used, the diffusion of the fluorescent species across the interface ($l = \sqrt{Dt_{polymerize}}$) between the streams is small ($\sim 2\mu m$) when compared to the length of the particle given that the diffusivity in such viscous materials is typically on the order of $10^{-10}m^2/s$. [111] This simple analysis does not take into account the instant viscosification of the oligomer during crosslinking that results in even lower diffusivities and sharper interfaces in practice.

After particles were synthesized and rinsed, we took scans of fluorescent intensity along the length of the particles (and entire width) at the fluorescent/non-fluorescent interfaces (Figure 6.8b). As can be seen, the particles made using SFL show a dramatically sharper interface than those using CFL because we were able to use a higher velocity. This difference would be even more dramatic if it was necessary to preserve smaller feature sizes, which would further decrease the velocity for CFL. Therefore, the benefit of using SFL for synthesis of multi-functional particles is threefold, improving (1) throughput, (2) resolution, and (3) sharpness of interfaces.

6.8 Conclusion

In this chapter, we have demonstrated that stop-flow lithography can be used as a high throughput method for the synthesis of polymeric particles and structures down to the colloidal length scale. Operating the process in stop-flow mode is preferable to the previously demonstrated continuous flow lithography (CFL) because both improved resolution and dramatically higher particle throughput are achieved. One of the attractive features of flow lithography is its ability to form free-standing structures in any free-radical polymer precursor material. This enables the fabrication of particles and structures in a diverse range of functionalizable polymers that are not accessible

to traditional photolithographic techniques because they cannot be spin-coated. SFL represents an important step towards performing high resolution photolithography for the formation of non-spherical colloidal structures in a variety of materials. We have also shown in this paper that the synthesis of multifunctional particles with sharp interfaces between the distinct sections can be achieved much more easily using SFL than CFL.

There is further work to be undertaken in order to push the process towards better resolution and higher particle throughput. Sub-micron resolution can be achieved by pushing device height down to a few microns and/or using immersion objectives. Particle throughput is currently limited by the spot size of the microscope objectives that we are using. However, the setup can quite easily be extended to produce orders of magnitude more particles simply by using larger area exposure lamps and microchannels that span larger dimensions. We believe that SFL represents a considerable advance in making flow lithography amenable to the synthesis of a variety of polymeric particles in a simple yet high throughput fashion.

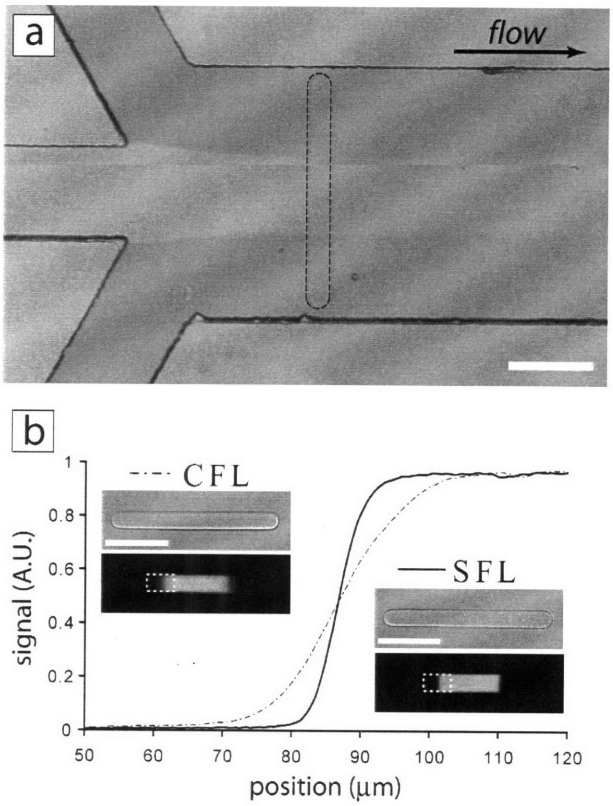

Fig. 6.8: *Interface comparison of multi-functional particles made using CFL and SFL. a)Striped, rod-shaped particles were formed by polymerizing for 0.05s across three adjacent streams in a microfluidic channel (300 μm wide, 40 μm tall) with three inlets (center stream loaded with fluorescent dye) that were connected to a common pressure source to maintain constant stream widths. b)A scan of fluorescent intensity along the particles at a fluorescent/non-fluorescent interface. The inset shows DIC and fluorescence images of particles made using CFL at a flow velocity of ∼50 μm/sec, and SFL with a velocity of ∼1,000 μm/sec with a t_{stop} of 0.05s. Scalebars in b) are 100 μm.*

CHAPTER 7

Modeling of Flow Lithography

7.1 Introduction

The photopolymerization process is central to particle and structure formation in this thesis. While this work has been devoted to using photopolymerization for the formation of free-standing polymeric particles, photopolymerization is routinely used in films and coatings, graphic arts, inks, adhesives, dentistry and semiconductor fabrication [112–114]. Based on the mechanism of photoinitiation, photopolymerization reactions can be broadly divided into free radical and cationic systems. Except for Chapter 2, all the oligomers used in this thesis polymerize through free radical polymerization. In free-radical systems, light-sensitiive photoinitiator molecules present within an oligomeric liquid (typically an acrylate or a methacrylate) react with photons of light to generate free radicals. These radicals initiate the polymerization process, rapidly converting the liquid to a cross-linked solid network. A wide variety of monomers and oligomers can be used to tailor the structure and properties of the cured materials while pigments and other additives may be added to confer color, stability etc. In addition to the advantages of rapid curing, such materials are convenient to use because they do not require the use of organic solvents and can be cured at ambient temperature.

Photolithography [115] which involves the transfer of a geometric shape from a photomask to a substrate through photopolymerization has the further advantage of allowing for the precise definition of shape. This ability to pattern pre-designed shapes is very important in the semiconductor industry where complex two-dimensional patterns are often stacked on top of each other

to create a device. Free radical photopolymerization is now also widely used for the synthesis of cross-linked hydrogels which find applications in tissue engineering, contact lenses and drug delivery systems [116].

As we have seen in this thesis, free radical photopolymerization has recently become the basis of of several new microfluidic approaches for the synthesis of individual polymeric particles on the micron scale [27]. Traditional approaches for particle synthesis such as emulsion and suspension polymerization typically make polymeric particles that are spherical and chemically homogeneous. On the other hand, microfluidic techniques enable the synthesis of large numbers of particles with complex shapes and tunable chemical anisotropy that are important for applications in diagnostics [13], photonic crystals [7] and field-responsive materials [109].

The viability of the flow lithography processes developed in this thesis (Chapters 3,4,5,6) is based on the inhibition of free radical polymerization reactions at the surface of the PDMS devices used. Oxygen diffusing in through the porous PDMS walls is able to inhibit photopolymerization reactions by forming chain terminating peroxide species [55]. The oxygen consumed in these terminating reactions (Table 7.1) is replenished by the oxygen that is constantly diffusing in through the PDMS walls. These competing processes ensure that there is an uncrosslinked, "lubrication layer" close to the walls which enables the particles to flow out without sticking.

Custom-designed polymeric particles generated using flow lithography are expected to find several applications [27] in addition to their demonstrated use for particle diagnostics [13] and self-assembly [49]. This makes it important to model the photopolymerization process involved in the synthesis of such particles. Several groups have developed models of free-radical photopolymerization [55, 117–122]. These models typically describe the curing of a monomer/oligomer coating (usually several millimeters thick) on a solid substrate exposed to UV light. In such a scenario, the oxygen inhibition effect is considered only at the free surface of the film which is exposed to UV light. Here, the polymerization proceeds in a frontal photopolymerization mode (FPP) where the boundary that separates polymerized solid and liquid moves forward in time like a wave front. Important variables to be quantified in such a scenario are the depth of curing and the properties of the cure at surface.

The geometry of the devices used in flow lithography is different from the geometry of a typical coating application. In flow lithography, the oxygen inhibition occurs symmetrically at both the top and bottom walls of the PDMS device (Figure 7.1). The polymerization front then proceeds from the center of the channel outwards in a mode that we call CSFP (Centrally Symmetric Frontal Polymerization). Further, the films we are considering are very thin ($< 50\mu$m) making the oxygen inhibition effect very significant throughout the film. In this chapter, we propose a simple model to predict the variation in the concentration of unconverted oligomer and oxygen dissolved within the oligomer during stop flow lithography (SFL). From these results, we can easily infer the height and cross-linking density of the particles formed. An experimental strategy to verify the model predictions is also described.

7.2 Model Description

The reactions that are commonly used to describe free radical polymerization are shown in Table 7.1. In the first step, UV light incident on the sample photolyzes the initiator molecules to produce radical species through a photocleavage process. For example, using a unimolecular photoinitiator like Darocur 1173 leads to the formation of one radical species per initiated molecule. The cleaved

Reaction	Mechanism Step
$I \xrightarrow{h\nu} 2\dot{R}$	Photolysis
$\dot{R} + M \rightarrow R\dot{M}$	Chain Inititation
$R\dot{M}_n + M \xrightarrow{k_p} R\dot{M}_{n+1}$	Chain Propagation
$R\dot{M}_n + R\dot{M}_m \xrightarrow{k_t} RM_nM_m$	Chain Termination
$R\dot{M}_n + O_2 \xrightarrow{k_o} RM_nOO$	Inhibition

Table 7.1: *Reaction mechanism in free radical polymerization*

photoinitiator molecules reacts with an oligomer (PEG-DA in our case) to initiate the polymerization. In the chain propagation step, a radical species adds on one more oligomer molecule. When two radical species react with each other they terminate to form a longer chain. Molecular oxygen reacts with radical species converting them to peroxide species which do not take further part in the reaction. Each molecule of PEG-DA can form two radical species because of the two acrylate groups on either end. Because of this property, such multifunctional acrylates are ideal for rapid formation of cross-linked networks [63].

The following is a simplified, one-dimensional (z-direction), unsteady state model that describes the variation in concentration of oxygen and unconverted double bonds in the oligomer. Some basic assumptions made in this model are

1. The model does not account for the fact that the multifunctional oligomers used in this study have more than one reactive species (the double bond) in each molecule.

2. The diffusion of oligomeric species and radicals can be neglected because of their large size.

3. The concentrations of radicals, oxygen and monomer are assumed to vary only in the z-direction in the model used to obtain the analytical solution.

4. Non-isothermal effects are neglected because of the high surface area of the system which is presumed to make thermal gradients insignificant.

5. Parameters used in the model are assumed to be invariant with changes in oligomer conversion.

Using Beer's law for the variation of light intensity through the oligomer, we get

$$\frac{\partial I(z)}{\partial z} = -\varepsilon[PI]I(z) \tag{7.1}$$

where ε is the permittivity at 365 nm and $[PI]$ is the concentration of the photoinitiator.

For a non photo-bleaching initiator, the amount of light absorbed(I_a) on a volumetric basis is given by integrating Equation 6.3

$$I_a(mol\ photons/cm^3/s) = \frac{I_0 - I_t}{H} = \frac{I_0}{H}(1 - exp(-\varepsilon[PI]H)) \tag{7.2}$$

For thin films of oligomer, $\varepsilon[PI]H \ll 1$ and only the first term in the Taylor series of the exponent in Equation 7.2 is significant yielding

$$I_a = I_0 \varepsilon[PI] \tag{7.3}$$

The concentration of radicals created by the absorbed light is then given by

$$r_i = \varphi I_a = \varphi I_0 \varepsilon[PI] \tag{7.4}$$

where φ is the quantum yield of formation of initiating radicals. If necessary, the variation in light intensity and hence radical concentration in the z-direction can be taken into account by using Equation 7.2 to calculate $I(z)$. The rate expression in Equation 7.8 would then contain a function of z. An analytical solution in this case too can be calculated by using the FFT method. The rate of radical consumption is given by

$$r_- = k_t[\dot{X}]^2 + k_O[\dot{X}][O_2] \tag{7.5}$$

For thin films exposed to high concentrations of oxygen, we make the further assumption that

$$k_O[\dot{X}][O_2] \gg k_t[\dot{X}]^2 \tag{7.6}$$

This assumption is justified on account of the fact that typical values of k_O are a few orders of magnitude greater than values of k_t [118]. Equating Equations 7.5 and 7.4 using the assumption in Equation 7.6, we get the concentration of radicals to be

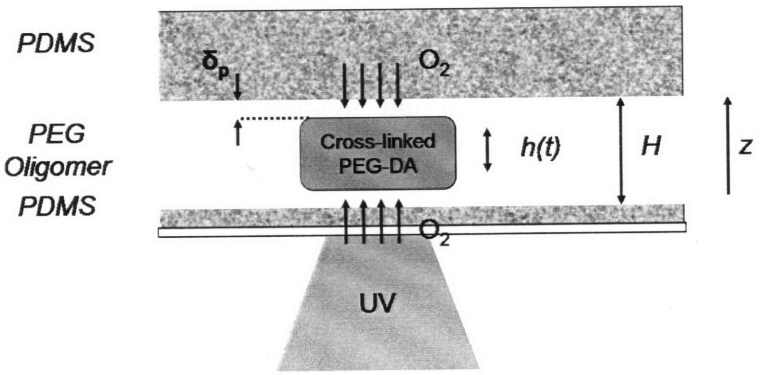

Fig. 7.1: *Cross-section of channel showing a particle formed in flow lithography. A thin layer of oligomer film is sandwiched in an all-PDMS device. Mask-defined UV light is projected through the bottom of the channel. Polymerization proceeds from the center of the channel outwards leaving a thin, uncrosslinked layer of oligomer adjacent to the top and bottom walls of the device. This is caused by Oxygen diffusing through the porous PDMS, inhibiting the reaction to forming non-reactive peroxide species.*

$$[\dot{X}] = \frac{\varphi I_0 \varepsilon [PI]}{k_O [O_2]} \tag{7.7}$$

The equation for oxygen transport inside the oligomer system is given by

$$\frac{\partial [O_2]}{\partial t} = D_O \frac{\partial^2 [O_2]}{\partial z^2} - k_O [O_2][\dot{X}] \tag{7.8}$$

Non-dimensionalizing Equation 7.8 using

$$\tau = t D_O / H^2 \tag{7.9}$$
$$\theta = [O_2]/[O_{2.eqb}] \tag{7.10}$$
$$\eta = z/H \tag{7.11}$$

we get

$$\frac{\partial \theta}{\partial \tau} = \frac{\partial^2 \theta}{\partial \eta^2} - Da \tag{7.12}$$

where the Damköhler number is given by

$$Da = \frac{\varphi I_0 \varepsilon [I] H^2}{[O_{2.eqb}] D_O} \tag{7.13}$$

and the boundary conditions for the equation are given by

$$\begin{aligned} \theta(0, \tau) &= 1 \\ \theta(1, \tau) &= 1 \\ \theta(\eta, 0) &= 1 \end{aligned} \tag{7.14}$$

Here we have used the assumption that the rate of oxygen mass transfer in PDMS is much greater than the rate of diffusion of oxygen inside the oligomer. This assumption is based on the fact that the diffusivity of oxygen in PDMS is two orders of magnitude greater than the diffusivity of oxygen in PEG-DA [123]. Therefore the concentration of oxygen at the interface between the PDMS and the oligomer is always assumed to to be the equilibrium concentration of Oxgyen.

The solution for Equation 7.12 using the boundary conditions in Equation 7.14 is given by

$$\theta = 1 + \sum_{n=1}^{\infty} \frac{Da(1 - (-1)^n)(e^{-n^2 \pi^2 \tau} - 1) sin(n\pi\eta)}{n^3 \pi^3} \tag{7.15}$$

The concentration of unconverted double bonds in the oligomer is given by

$$\frac{dM}{dt} = k_p [M][\dot{X}] \tag{7.16}$$

where $[\dot{X}] = \frac{\varphi I_0 \varepsilon [PI]}{k_O [O_2]}$. Non-dimensionalizing Equation 7.16 using $\xi = [M]/[M_0]$, we get

$$\frac{d\xi}{dt} = k_p \xi \tag{7.17}$$

with the initial condition $\xi(t = 0) = 1$

The solution in Equation 7.15 is then inserted into Equation 7.17 to get the concentration of unconverted double bonds. The multiple parameters in the problem are captured by the dimensionless Damkohler number. Using the values of the parameters shown which are typical to our system (Table 7.2), we calculate a Da of 30. In Figures 7.2 and 7.3, we plot the concentration of oxygen and unconverted oligomer respectively. We find that the oxygen concentration at the center of the channel falls by three orders of magnitude within 1s while the boundary conditions at either end impose equilibrium concentrations of oxygen at the top and bottom walls of the device. The oxygen concentration is symmetric about the center of the channel because the variation in light intensity along the z-direction has not been taken into account. We find that oxygen concentration drops to negative values in the center of the channel for t ¿, 0.5s because of the approximation made in Equation 7.6. This assumption is a poor once once oxygen concentration has dropped drastically and must be altered to obtain a more realistic solution for longer time scales.

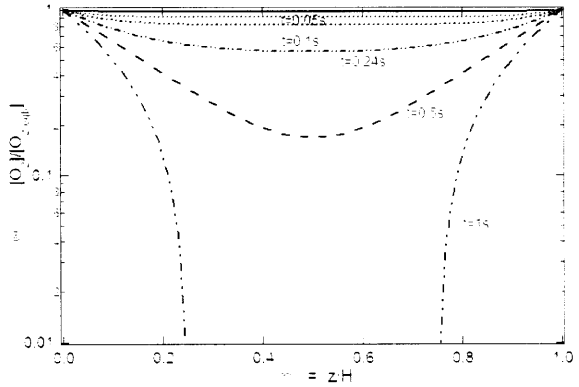

Fig. 7.2: *Plot showing the depletion of oxygen in the oligomer film. Oxygen concentration is non-dimensionalized using the equilibrium concentration of O_2 in PEG-DA. Oxygen concentration falls by an order of magnitude in the center of the channel and is symmetric about the center of the channel.*

In Figure 7.3, we also see that no significant conversion of the oligomer has taken place. Because of the assumption that oxygen inhibition dominates termination (Equation 7.6), we see that oxygen concentrations predicted by the model are too high for any significant conversion to occur. This points to the fact that this model may be overly simplified for the prediction of oligomer conversions. In the next section we use a full solution to the equation to get more realistic predictions of oligomer conversion.

7.2.1 Full Solution

Two key simplifying assumptions were used in the previous section to obtain an analytical solution to the problem. Light intensity was assumed to be constant across the height of the channel and the oxygen inhibition step was assumed to dominate the radical termination step. In this section

we present results that do not make these two assumptions.

In Equation 7.2, we have an expression for the concentration of absorbed photons at a certain location within the channel. We use this to obtain $I(z)$. The second assumption made to simplify the problem in Equation 7.6 becomes invalid when oxygen concentration is depleted below a certain point. Earlier work [55] has shown that oxygen concentration needs to fall by about 300 times its initial value before polymerization can even start. As we approach such concentrations, we need to use Equation 7.5 in order to obtain a more accurate expression that can relate $[\dot{X}]$ and $[O_2]$. Using Equation 7.5 to get an expression for $[\dot{X}]$ however renders Equation 7.12 unsolvable by analytical means. We present results from the numerical integration of the full equation using the parameters in Table 7.2. The parameters reported here are typical values obtained for acrylates [55.121–124].

We find that both the oxygen and monomer concentrations are still symmetrically distributed around the center of the channel. This means that our assumption in the simple model that light intensity does not significantly change through the sample is valid. Oxygen concentration is found to drop dramatically around 0.34s leading to the start of the crosslinking process around 0.4s which is larger than experimentally observed values. The values of the parameters like the diffusion of oxygen in oligomer and rate constants need to be further verified to get time-scales that are observed experimentally. Also because the termination step is now taken into account, we are able to predict some finite conversion of oligomer, unlike the analytical solution which gives zero conversion of oligomer even at 1s. The analytical model must therefore be corrected at the center of the channel to include the termination step in order to give more realistic results.

The conversion of oligomer follows a similar symmetric profile as the oxygen. Particle heights can be extracted from plots of oligomer conversion by fixing a critical conversion fraction at which the gel point is reached. This is illustrated in Figure 7.5 by assuming that a conversion of 10% is required to crosslink the oligomer [63]. Figure 7.5 also clearly shows the presence of an uncrosslinked layer of oligomer on either side of the particle as we would expect. Further investigations are

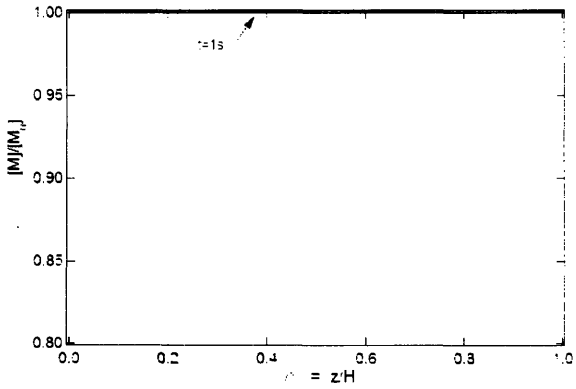

Fig. 7.3: *Plot showing the concentration of unconverted oligomer in time. Oligomer concentration is non-dimensionalized using initial oligomer concentration. The model is unable to predict any changes in oligomer conversion over the time scales of practical interest.*

Parameter	Value	Units	Source
k_p	21.7	$m^3/(\text{mol.s})$	[121]
k_t	2520	$m^3/(\text{mol.s})$	[121]
k_O	5×10^4	$m^3/(\text{mol.s})$	[55]
D_O	5×10^{-11}	m^2/s	[123]
H	20	μm	Measured
I_0	1.5×10^{-2}	$\text{E}/(m^2.\text{s})$	Measured
$[PI]$	388	mol/m^3	Measured
ε	1.6	$m^3/(mol.m)$	[124]
$[O_{2.eqb}]$	1.5	mol/m^3	[122]
φ	0.6	-	[124]

Table 7.2: *Table showing the values of typical parameters used to perform numerical integration. These values were obtained from different sources in the literature as indicated in the right most column.*

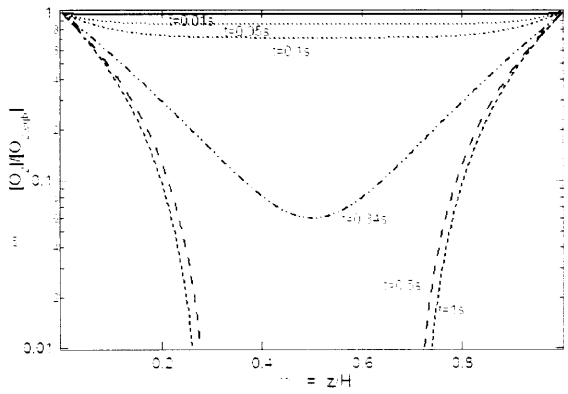

Fig. 7.4: *Oxygen concentration vs. time and space for the conditions shown in Table 7.2. The concentration is plotted against non-dimensional channel height over two decades and falls rapidly close to the center of the channel while being at equilibrium at $\eta = 0$ and $\eta = 1$ which correspond to the bottom and top walls respectively. Oxygen concentration is not symmetric about the center because of the reduction in light intensity across the channel height.*

required to probe the effect of channel height and light intensity on the thickness of this layer.

7.3 Proposed Experimental Study

The results obtained from the models in the previous sections need to be compared with experiment. From the model data in Figure 7.5, we can extract data on particle heights at different values of exposure time, light intensity, channel height and photoinitiator concentration. These can then be compared with experiments performed under the same conditions. Since only average double bond conversions for each particle (this is something that varies with the z-dimension) can be extracted using FTIR spectroscopy, we cannot easily compare the model-predicted and experimental values of double bond conversion. Once detailed experimental results are available, the accuracy of the model be judged.

7.4 Conclusion

In this chapter, we developed a simple model to predict the concentration of unconverted oligomer and the concentration of oxygen dissolved in the oligomer during the process of exposure to UV light in flow lithography. This one-dimensional model assumes no variation in parameters with conversion, uniform temperatures and is based on a simplified mechanism of free radical polymerization. Even so, the model is able to qualitatively predict behavior that has been experimentally observed. For instance, the presence of an oxygen inhibition layer that permits the flowing out of the particles is clearly seen in the model. Only further comparison of experimental results with the

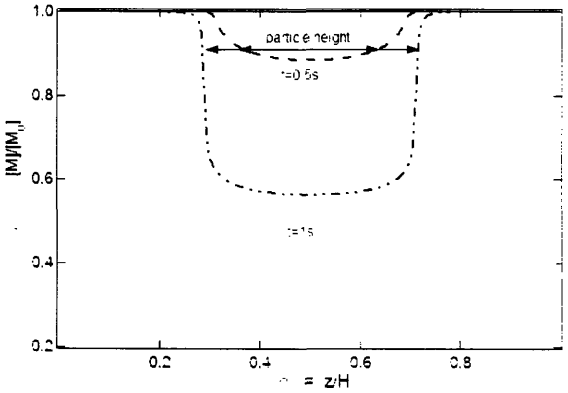

Fig. 7.5: *Unconverted oligomer concentration vs.time and space for the conditions shown in Table 7.2. Significant conversion of oligomer (> 5%) is observed only for t > 0.3s. Oligomer conversion is higher close to the center of the channel. Particle height increases with time as more and more oligomer is converted. Results show how oxygen inhibition leads to the formation of a thin, uncrosslinked layer of oligomer on either side of the particle.*

model will allow us to judge its accuracy. Ultimately, we would like to use such a model to tune the height and crosslinking density of particles formed using SFL in a convenient fashion.

CHAPTER 8

Conclusions and Outlook

In this thesis, three new microfluidic approaches to particle and structure synthesis have been discussed. The primary focus of the thesis was the development of the flow lithography techniques, CFL [38] and SFL [94], for the synthesis of micron sized polymeric particles in any 2-D extruded shape. Besides the flow lithography techniques, two other methods were also presented - a 2-phase approach [34] to form a limited class of non-spherical particles and a phase-mask based approach to form patterned hydrogel structures (Chapter 5).

8.1 Two Phase Method

In Chapter 2, a method to produce plugs and disks by confining and then freezing photopolymer droplets formed at a T-junction was described. The work marked the first step towards synthesizing complex morphologies in a microfluidic device. Up unto this point, all microfluidic methods in the literature had demonstrated the controlled synthesis of spherical polymeric particles. Our work demonstrated that the geometric confinement of droplets in a microfluidic device could be exploited to form shapes that are elementary deformations of spheres - disks and plugs. This method also has the advantage of consuming all the polymer precursor used to form particles. At the same time that our work [34] appeared, another very similar paper, that used a flow focusing geometry to form non-spherical polymeric microparticles, was published [35]. The group of Kumacheva has followed up this paper with several others that describe the formation of complex morphologies using droplet-based microfluidic devices [36, 125].

8.1.1 Characterization of Droplet Formation

In our work, a phase diagram approach was used to characterize the different phases seen in our device. Plug length was also plotted as a function of continuous phase flow rates for different dispersed phase flow rates. After this work was published, there has been much more detailed analysis into the problem of droplet formation in a microfluidic device. It has been shown for example that droplets breakoff not so much because of the effect of shearing forces at a T-junction but because of geometric confinement effects [50]. This analysis applies to low Capillary numbers and a more general analysis that can predict the effect of changes in viscosities of the fluid as well as flow rates is still awaited. Another aspect that deserves some analysis is the oscillation in droplet sizes that is seen at low values of the continuous flow rates. This affected our ability to synthesize monodisperse long plugs and could possibly be caused by the continual deformation and relaxation of the PDMS device.

8.1.2 Future Work

While we used an optical adhesive (NOA 60) to form particles, any photopolymerizable material may equally be used. Acrylate materials are very suitable for such applications because of their high reactivity and their ability to be functionalized with diverse biological and chemical species. They have been extensively used in more recent work, including our own, on particle formation in microfluidic devices. One aspect that was overlooked in our work is that the exposure dose given to the particles can be altered to form ellipsoids with varying eccentricity. This provides another convenient tool to tune particle morphology. Another aspect that deserves some attention is the quest to reduce the size of the particles formed down to the colloidal scale. Because of the nature of our technique, geometric confinement at the colloidal scale is then necessary to form non-spherical particles. While the width of channels can be reduced down to only 10 μm easily, using current techniques, the height can be quite easily reduced down to 1 μm. Caution must be taken to ensure that the device is tightly sealed, when such low heights are used, because of the large pressures required to drive flows ($\Delta P \propto H^{-3}$). Finally, the process could be scaled up by massively increasing the number of T-junctions in one device. Care must be taken to ensure that the conditions at each T-junction are equalized so that the particles formed are monodisperse.

8.2 Flow Lithography

The flow lithography techniques that we have developed are unique in their ability to combine the best attributes of two techniques - photolithography and microfluidics. Photolithography offers precise shape control but is traditionally thought of as a low throughput, batch process. On the other hand, microfluidic particle syntheses form particles in a continuous fashion but lead to only a limited number of morphologies. By successfully combining photolithography and microfluidics, flow lithography has introduced a new paradigm for particle synthesis. The central idea enabling flow lithography is the oxygen-induced inhibition of free-radical crosslinking reactions near PDMS device walls. This allows for particles to be flowed out immediately after forming. This chance discovery has demonstrated yet another advantage of performing microfluidic processing in PDMS devices, adding to the already long list of PDMS's favorable properties.

Flow lithography permits the formation of particles and structures in bio-compatible hydrogel polymers that are typically not amenable to being spin-coated. In fact, any material that can

undergo free radical polymerization can be used to form free-standing particles in flow lithography. While this is a fairly large class of materials - comprised mainly of acrylates and methacrylates - the idea of using an inhibition layer close to the walls of a device to form and flow particles is a fairly general one. One could therefore envisage using other polymer chemistries that were suitably inhibited at device walls to form and flow structures/particles made of materials other than free radical polymer precursors.

8.2.1 Future Work - Morphology

While we have explored various 2-D extruded shapes (Chapter 3) and some classes of 3-D shapes (Chapter 5), other classes of shapes could also potentially be achieved using flow lithography. Using grayscale masks or the deformability of the PDMS elastomer, for example, one could achieve some three dimensionality in the shapes formed. Another way to achieve limited three dimensionality would be to build devices that have non-rectangular cross-sections and then polymerize particles in them.

8.2.2 Future Work - Applications and Throughput

Like with all microfluidic processes, throughput is an area where flow lithography falls short when compared to bulk processing techniques like emulsion polymerization. The control over particle morphology and anisotropy that flow lithography offers is unrivalled. But what is the future of such processes for industrial applications? For one, it seems that techniques like SFL will well serve niche applications such as particle diagnostics [13] or hydrogel particle based sensors [126] where the ability to create complex morphologies or create monodisperse bead solutions adds tremendous value to the final product. Other potential application areas include designer paints, contact lenses and field-responsive fabrics.

One can think of this thesis as a progression of ideas in terms of scale-up. The two-phase approach can be thought of as a 1-D approach where particles are synthesized one at a time. The flow lithography techniques permit the synthesis of 2-D arrays of particles with each exposure. The phase mask based particle synthesis technique could potentially synthesize 3-D blocks of particles because of its ability to form stacks of particles on top of each other. Providing this sort of a 3-dimensional approach to particle synthesis will allow microfluidic techniques to compare with traditional 3-dimensional techniques like emulsion polymerization. The way forward in terms of increasing throughput is to use much larger area lamps and larger area microfluidic devices. Standard photolithographic steppers, for example, polymerize across an area several inches in diameter. If we used such a stepper with a PDMS device several inches in width, we could dramatically scale up particle throughput. One must note that there are also restrictions on the aspect ratio of PDMS devices. A rule of thumb is that the width of the device should not be larger than 30 times the height of the device. Therefore to construct a wide PDMS device, one must provide supporting posts or simply have rows of millimeter wide channels running parallel to each other.

Increasing the throughput and complexity of multifunctional particles is another area that deserves attention. Because we are co-flowing streams in a side-by-side fashion, flow lithography techniques are limited to synthesizing only one row of such multifunctional particles at a time. Further, only two different functionalities can be adjacent to each other. Some possible solutions to this challenge are

- To make an array of Janus particles that contain only two functionalities, we can flow two streams of oligomer on top of each other. At the micro-scale, the competition between viscous forces and gravitational forces dictate when fluids will flow on top of each other as opposed to a side-by-side configuration [127].

- For particles with multiple (> 2) functionalities, one way to achieve higher throughput would be to flow streams of particles in parallel to each other in a repeating fashion. Stream widths could be adjusted precisely by tuning the surface chemistry of the PDMS walls for example. By defining the mask such that arrays of structures were aligned with the streams, one could achieve higher throughput.

8.2.3 Future Work - Resolution

While SFL has achieved particles down to 1 μm in size, particles down to 400 nm can theoretically be formed using 365 nm UV light. Such particles would show significant Brownian motion and be useful for studies on self-assembly and rheology to give two examples. However, significant challenges remain in synthesizing sub-micron particles. Some issues that need to be addressed are:

- Transparency masks can be cheaply printed down to a resolution of 10 μm, where the loss of image quality is already apparent. Chrome or other high quality masks masks must be used to obtain shapes with smaller features.

- The spot size of a microscope objective decreases with increase in magnification. While a 100X objective can potentially be used to make nano-sized particles, an array measuring only $\sim 100\mu m$ in size can be created with each exposure. Ideally, we would like to use low magnification objectives and high resolution masks to get around this problem.

- The acrylates that we have been using so far are not optimized for high resolution particle synthesis. Further investigation into materials that yield higher resolution structures is necessary

8.3 Modeling Flow Lithography

The oxygen inhibition effect that permits flow lithography was also modeled using a very simple reaction mechanism. The parameters used were not assumed to be functions of conversion while changes in temperature were neglected. An analytical expression for oxygen concentration was then found by assuming light intensity within the thin film to be constant and by assuming that the oxygen inhibition step was dominant over the radical termination step. A more general model that did not make the last two assumptions was also proposed and solved by numerical integration techniques. The more general model showed the presence of an oxygen inhibition layer and predicted the rapid depletion of oxygen concentration at the center of the channel. Further experimental work is required to test the predictions of the model.

Appendix A

Tips and Tricks

In this appendix, various experimental protocols and guidelines that have not been mentioned in the main section of the thesis are described.

A.1 Ferrofluid Synthesis

This method to synthesize ferrofluid is based on the French patents FR 2461521 and FR 2662539 and is commonly referred to in the literature as Massart's technique. The protocol described below yields 20 ml of concentrated ferrofluid (> 50 g/ml).

1. Take 400 ml of 0.75M NaOH in a 2L beaker and heat to 100°C. Keep stirring and maintain at 100°C

2. Prepare a mixture of 40 ml $FeCl_3$ (1M) and 10 ml $FeCl_2$ (2M in 2M HCl). This step requires 12g of solid NaOH to be dispersed in 400 ml of H_2O. The weight of $FeCl_3$ (MW 270.3) is 10.81g and is dispersed in 35 ml of H_2O. The weight of $FeCl_2$ is 3.98g and is dispersed in 8 ml of 2M HCl.

3. Add the above mixture drop by drop to the heated base for 5 minutes.

4. Keep at 100°C for 10 minutes and then cool to room temperature.

5. Get rid of the supernatant using a magnetic decanter (there is one in the Hatton lab).
6. Add 200 ml of H_2O and agitate for 10 minutes. Use the magnetic decanter to get rid of the supernatant.
7. Repeat the above step twice.
8. Add 200 ml of HNO_3 (1M) and stir for 10 minutes. Repeat step 5. Note that you will need 1.2 l of 1M HNO_3. Add 108 ml of 70% HNO_3 to 1092 ml of water to make this solution.
9. Repeat step 8 twice.
10. Now, add 200 ml of H_2O and stir for 5 minutes. Then, add 200 ml H_2O and stir for 5 minutes. then add 200 ml HNO_3 (1M) and repeat step 5.
11. Repeat step 10 thrice.
12. Centrifuge at 2000 rpm for 1 hour and eliminate the supernatant.
13. Disperse 3g of the sedimented gel in 10 ml of final solution.
14. (Note: At this point you have a ferrofluid that is not yet stabilized with protective groups) Take the solution from the previous step and make it up to 300 ml. Stir at 90 °C for 30 minutes using 11.5g of Sodium Citrate.
15. Cool the precipitate down. wash with acetone and re-suspend in H_2O.
16. Centrifuge at 15000 rpm for 2 hours.
17. Disperse the precipitate in 20 ml of H_2O to make a 15 volume percentage ferrofluid at pH 7.

A.1.1 Measuring the Concentration of Iron in Ferrofluid

After making the ferrofluid it is essential to characterize it by calculating the concentration of iron. This protocol describes how this measurement is done.

1. Dilute the ferrofluid till its concentration is approximately 0.5 weight % (soln. 1). Prepare 2 more solutions of 1% (soln. 2) and 1.5% (soln. 3) weight percentage
2. Take three 25 ml bottom and add 100 μl of ferrofluid to each flask
3. Add 400, 800 and 1200 μl of 37 % of HCl to flask 1, 2 and 3 respectively.
4. Heat with an air gun until you see the solution boiling and then let cool to room temperature.
5. Prepare a tyron (4,5-dihydroxy, 1,3-benze disulfonic acid, disodium salt monohydrate) solution of concentration 83g/L.
6. Add 400, 800 and 1200 μl of tyron solution to the flasks 1,2 and 3 respectively.
7. Add 3,6 and 9 ml of 4N NaOH to flasks 1, 2 and 3 respectively.
8. Add DI H_2O to bring all 3 solutions to 25 ml and mix.

9. Add 1 ml of each of these to a glass vial and add 4 ml of H_2O.

10. Measure the absorbance of this solution at 480 nm. Accept only those values that are less than 0.5 to avoid saturation effects. Dilute with more water till the absorbance is below this value

11. Calculate the weight concentration of iron by using the formula

$$\text{concentration of } Fe_3O_4 \text{ (g/ml)x} = \text{Total dilution} \times \frac{A}{39986} \times \frac{231.52}{162.15} \times \frac{1}{3} \tag{A.1}$$

12. For example in the above steps, a dilution of 25 × 5 was done. Further, the ferrofluid itself was diluted at the very beginning of the experiment. The factor of 39986 is a calibration factor, 231.52 is the molecular weight of Fe_3O_4 and 162.15 is the molecular weight of $FeCl_3$ while the 1/3 factor takes into account the fact that iron is trivalent (Fe^{+3}).

A.2 Liposome Preparation Techniques

Several methods exist to synthesize liposomes. Some of the methods that I have implemented in our laboratory are described below.

A.2.1 Using a Roughened Teflon Disk

This method uses a Teflon disk roughened with emery paper to make phospholipids vesicles [128]. A circular Teflon disk is roughened with emery paper to form tiny grooves oriented in one direction. The disk is then thoroughly cleaned by washing in detergent, tap water, distilled water and chloroform. It is preheated to 40C in an oven. 50L of 10mg/mL DMPC in chloroform-methanol(2:1) is then added to the warm disk with a needle and quickly spread over the surface. The solvent evaporated immediately to leave the small amount of lipid as a thin film over the whole surface. The film of lipid was then evacuated to remove the last traces of solvent. The Teflon disk and lipid film were prehydrated at 40C in a loosely Parafilm-sealed beaker with water-saturated argon. This allows the closely stacked lamellae to swell and hydrate as much as possible prior to the addition of bulk water. Final hydration of the lipid was accomplished by the addition of distilled water at 30-35C; the beaker was left covered in the oven to allow the lipid to hydrate undisturbed.

A new simplified version of this method [129] is as follows. A lipid film is obtained on a roughened Teflon piece by evaporating a lipid-cloroform:methanol(2:1) mixture. The disk is then further dried in a vacuum oven to remove the last traces of the solvent. The disk is then placed in a 200mOsm solution of sucrose and allowed to hydrate.

A.2.2 Rapid Preparation (Method of Moscho et al.)

This method is used to prepare giant unilamellar vesicles (GUVs) in a fast manner [130]. Lipids were dissolved in choloroform (0.1M) and 20 μl of this solution was added to a 50 mL round-bottom flask containing 980 μl of chloroform and 100-200 L of methanol. The aqueous phase (7ml of distilled water or buffer) was then carefully added along the flask walls. Liposomes were formed in distilled water. Molecules to be entrapped in the vesicles were added to the buffer solution prior to the evaporation of the organic solvent. The organic solvent was removed in a rotary evaporator (Buchi

R-124) under reduced pressure (Cole-Parmer aspirator pump, final pressure 10 mm Hg (1.3kPa)) at 40C and 40 rpm. As a consequence of the different boiling points of choloroform (61°C at 100kPa) and methanol (64C at 100kPa) they observed two major boiling events. After evaporation for 2 minutes, an opalescent fluid was obtained with a volume of approximately 6.5ml. The resulting aqueous solution contained GUVs in high concentration.

A.2.3 From Chloroform-Methanol in a Round Bottom Flask

The protocol described in Akashi et al. [131]was slightly modified to obtain a higher yield. Lipids were each dissolved at 7.5 mg/ml in chloroform/methanol (2:1 by volume) and stored under a blanket of argon at -25°C. 80 μl of the solution (0.6 mg lipid) in a 10 ml glass test tube (ID 1.5 cm) was dried at 45C with a rotary evaporator to form a thin lipid film on the bottom surface (2-3 cm high). The tube was subsequently placed in vacuo for >6 h to remove the last trace of the organic solvent. The completely dried lipid film was then prehydrated at 45°C with water-saturated N_2 for 30-60 s until the film became transparent. Five milliliters of an aqueous solution containing 0.1 M sucrose and appropriate salts, which had been N_2-purged, was added gently to the tube. The tube was sealed under argon and incubated at 37°C for 2 hours and then gently rocked to disperse the lipid film uniformly in the solution. After further overnight incubation at room temperature (22-24°C), we found, in successful cases, an almost transparent bulky white cloud floating in the middle of the solution, which contained giant liposomes. Otherwise, the solution contained only small particles at the top.

A.3 Ferrofluids and Liposomes

Liposomes containing the citrate-coated fluid described earlier were also prepared. These liposomes deform in the presence of an external magnetic field changing their shape depending on the direction of the field. The method to prepare magnetoliposomes is as follows:

1. Take 2 mg of lipid (DMPC or DOPC) and add to an eppendorf tube containing 10 μl of citrate-coated ferrofluid. Vortex mix this solution.
2. Take a clean petri dish and smear the mixture with a gloved finger on its surface.
3. Hydrate this petri dish in a saturate water bath at 45 °C for one hour.
4. Add 1 ml of water and observe the formation of lipid.

Note that the addition of water is a key step in this process.

A.4 T-junction Experiments

In this section, I describe some important details of various experiments performed with T-junctions.

A.4.1 Connectors and Tubing for NOA 60 Experiments

As alluded to in the previous section, smaller diameter glass syringes (Hamilton) are suitable when low flow rates are desired. I first tried using a cemented 50 μl glass syringe (80500, Hamilton)

but found I could not suck in the NOA 60 because it was too viscous for the needle used. I then switched to Teflon Luer-lock syringes (TLL) which were capable of sucking in the NOA 60. The connectors used in serial were syringe-P658-P692-0.02" diameter tubing-20RW connectors. The P658 and P692 connectors were obtained from Upchurch Scientific while the 20 RW stainless steel connectors were 0.375-0.5" in length and were obtained from New England Small Tubes.

A.4.2 Preparing the T-junction

For any microfluidic experiment, especially those involving multiple flows, it is important to avoid letting air enter the system at all costs. In T-junction experiments, the continuous phase must *always* be flowed into the channel first. Only when the continuous phase fluid has flowed all the way through the T-junction and out of the inlet port for the dispersed phase, should the dispersed phase connector or pipette tip be inserted in. This is to prevent any air from entering the system . When air is present, experimental readings of flow rates and pressure are unreliable because of the compressibility of air.

A.4.3 Unsteady State Flows using Syringe Pumps

The flow profile provided by syringe pumps is unsteady for two reasons. The first being the compression of fluid in the tubing external to the device due to the displacement driven flow. The second reason is that the stepper motor inside the syringe pump leads to an oscillatory profile at very low flow rates. A third cause of unsteady flows in a microfluidic device is the deformation of the PDMS itself (Chapter 5).

The first mentioned problem of compression of fluid in the tubing can be solved by reverting to compressed air driven flows. If syringe pumps are essential for a certain experiment, then the syringe must be carefully chosen in order to minimize the effect of the stepper motor. Typically low volume (50 μl) glass syringes (Hamilton) are good for low flow rates down to 0.03 μl/min. I found that using the 50 and 100 μl syringes for the dispersed and continuous phase considerably reduced oscillations in plug length that were seen while using 1ml syringes from Becton Dickinson. Further, 'wetting' effects that I saw with larger syringes disappeared when using the small volume glass syringes. Also 'wetting' was seen when flow rates greater than 0.1 μl/min were used.

A.4.4 Surface Tension Values for NOA 60 Emulsions

For NOA 60 droplets in water, $\gamma = 12.28 \pm 0.05$mN/m. For NOA 60 droplets in water containing 1% SDS, $\gamma = 6.65 \pm 0.01$mN/m

A.4.5 Making Plugs using 2-Phase Approach

The polymerization conditions under which plug are made is critical to the process. I used light intensities of 100% with the field stop open ($\sim$ 10%) and the aperture stop open ($\sim$ 10%). The conditions under which I made plugs successfully were $Q_d = 0.05$ μl/min and $Q_c = 0.2$-0.3 μl/min

A.4.6 Making Discs using 2-phase Approach

The channel geometry we have used is shown in Figure 2.1. As seen, disks are polymerized in the wider 200 μm section of the channel. To make the process smooth and avoid blockages, this section

should be fairly short.

A.4.7 Breaking off Ferrofluid Droplets at a T-junction

The objective in such experiments was to breakoff droplets of ferrofluid (typically EMG 905 or EMG 909) in water containing SDS (1%) using syringe pump driven flows. These ferrofluids are mineral oil based. Even after sonicating the ferrofluid, filtering it using a 0.2 μm filter, cleaning all the devices thoroughly, the ferrofluid would flow smoothly for 5-10 minutes before aggregation and blockages would occur in the channel carrying the dispersed phase. Plasma treating the channel (or not) or soaking the channel in mineral oil did not solve the problem either. I never got to the bottom of this problem but my guess is that some interactions between the PDMS and the ferrofluid were causing it.

I found that a good system to make ferrofluid droplets is to use the citrate coated ferrofluid whose synthesis is already described as the dispersed phase. Droplets of this ferrofluid can be formed using mineral oil containing Span 80 as the continuous phase (08/27/04). The devices in this case were made by first plasma treating a PDMS device to a PDMS-coated glass slide and then baking the device for 4 hours at 120°C to make it hydrophobic.

A.4.8 Making Emulsion Droplets of PEG

After experimenting with several systems, I found that the best way to make emulsion droplets of PEG based systems is to dissolve PEG-DA (400) in water at concentrations of 50% or less and then make emulsion droplets of such materials in mineral oil containing 2-3% of the surfactant ABIL EM 90.

A.4.9 Collecting Particles

Once polymeric particles have been formed using any of the techniques described in the thesis, isolating them is the next challenge. Collecting large numbers of particles needs some care. One particular challenge is that particles get stuck easily to the bottom of eppendorf tubes when they are spun down using a centrifuge. The sticking problem can be improved by adding a small quantity of surfactant (0.1% Tween 20) so that the particles don't stick to each other.

A.5 UV Light System

1. Look into buying an Excimer Lamp - these give high light intensities at a desired wavelength.

A.6 Flow Lithography - The Oxygen Inhibition effect

In this section, I will talk about some topics related to the inhibition of free radical polymerization caused by oxygen with respect to experiments that we have performed.

A.6.1 Testing the Oxygen Inhibition Theory

A control experiment was performed in an oxygen-free enviroment to test the oxygen inhibition theory. The details are as follows:

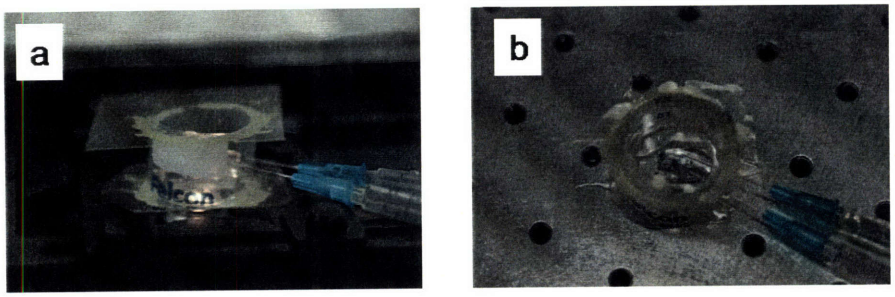

Fig. A.1: *Experimental apparatus showing the oxygen-free chamber used to perform flow lithography. a)Side view showing the two pots for entry of argon and oligomer. b)Top view showing how tubing is connected into the device*

1. Use a 43 × 50 mm glass slide and spin-coat PDMS on it and cure it. Cut the slide to fit into the microscope slider.

2. Seal a channel to it using a sacrificial layer of PDMS

3. Place a ring of a sawed off piece of of a Falcon tube on the glass slide and seal it with epoxy. The Falcon tube has 3 holes drilled into it using a hammer and a 24G luer needle. Hole 1 - Argon inlet. Hole 2 - Oligomer inlet. Hole 3 - Air outlet.

4. Cover the plastic ring with another 43 × 50 mm glass slide and seal with epoxy.

5. Connect two luer needles into the hole. One needle is connected to tubing and a connector and is used to supply oligomer. Check that particles flow after forming before the next step.

6. Purge the system for 30 minutes by connecting an Argon cylinder through hole 1 using a luer needle and a 1 ml syringe as seen in Figure A.1

7. Now check that the particles have stopped flowing and stick to the walls upon forming.

8. Purge with air for 30 minutes again and then check that the particles start flowing again.

A.6.2 Effect of Plasma Treatment

Plasma treating the channels and the PDMS-coated slides that they are sealed to typically results in the sticking of particles to the top and bottom walls of the device. This is obviously undesirable and we avoid this by placing a protective strip of PDMS on the channel and on the area of the PDMS-coated slide that lies beneath the channel. We could potentially utilize this phenomenon to tune the oxygen inhibition effect. However, plasma treatment is unpredictable in its effect so further investigation would be required to see if this is possible.

A.6.3 Making Particles in Low Height Channels

As the height of the channel is decrease, the oxygen inhibition effect becomes more prominent making it more difficult to make particles. For example using PEG-DA 400 and 5% Darocur 1173 as photoinitiator, it is impossible to polymerize particles into a 2 μm tall channel. There are some ways to try and get around this situation.

A.6.4 Strategies to Mitigate the Oxygen Inhibition Effect

I tried to use oxygen scavengers to see if they would negate the oxygen inhibition effect. A 55 mM solution of $NaIO_4$ in water was added to PEG-DA (400) but this did not help prevent the inhibition.

1. Soak the channel in photoinitiator solution for 30 minutes. A 10 % solution (w/v) of HPK in 70% ethanol was recommended by Greg Randall. Rinse and sonicate the channel in water for 20s and repeat this step two more times. Then soak in water for 30 minutes and dry (11/16/05). We have found that this technique helps to overcome the oxygen inhibition effect by possibly increasing the local radical concentrations because photoinitiator molecules can leach back into the oligomer as they get depleted. I did this in a 2 μm tall channel and was able to polymerize objects in 0.25-0.5s.

2. Another solution is to use mixtures of thiols and acrylates. Thiols are able to participate in crosslinking reactions even after forming peroxy species. An example of such a mixture is PETTA + PEG-DA along with photoinitiator. Some work needs to be done in optimizing thiol chemistry for this process to prevent sticking of the particles. I found that using thiols sped up efficiency of polymerization but the cross-linked structures seemed to dissipate soon after formation. The same was the case with NOA 60 when it was used to make particles in flow lithography mode.

A.7 Imaging Tips

A.7.1 Interesting Colloidal Structures

Often times, I noticed that after particles were mixed with ethanol and dried, interesting fractal or colloidal crystal structures were obtained. These structures were caused by ethanol evaporating from a solution of uncross-linked oligomer.

A.7.2 DIC Images of Particles

Differential Interference Contrast provides a route to images with much improved contrast over ordinary brightfield images. There are three components to implementing DIC in our Axiovert 200 - DIC analyzer, DIC prism/polarizer and DIC condenser. To get good DIC images, do the following:

1. First ensure that the DIC analyzer is inserted using the 3-slot slider that is beneath the filter cube holder on the Axiovert 200.

2. Make sure that the DIC prism for the 20X or the 40X is inserted underneath the objective.

3. Make sure that the DIC condenser above the sample is in place.

4. Tune the DIC prism below the objective by winding the metallic knob attached to it such that the image is at its least brightness.

5. Adjust the condenser screws above the sample such that the image hexagon is clearly in place and centered.

6. Reduce the light intensity in the circular slider below the condenser to a low value and increase the light intensity provided by the HAL lamp before taking an image.

A.8 Miscellaneous - Flow Lithography

A.8.1 Making Amphiphilic Particles

When flowing immiscible phases through the PDMS device, first always flow the hydrophilic phase. Only after this phase has wetted the walls for at least 10 minutes should the hydrophobic phase be flowed. Because the hydrophobic phase naturally tends to wet the channel walls, this step ensures that we can get parallel coflow without the hydrophilic phase deattaching from the walls.

A.8.2 Some Properties of PEG-DA

These are some fairly random properties of PEG-DA that I have noted over the past couple of years. Since we use this material often, I thought it would be useful for others to know.

1. A dye that dissolves in PEG-DA is Coomassie Blue R-250. Nile Red does *not* dissolve in PEG-DA.

2. Methacrylate monomers take an order of magnitude more time to polymerize when compared to acrylate monomers. Even when mixed in small quantities with acrylates, they tend to slow down crosslinking reactions.

3. A chemistry that swells at low pH is PEG-DA + Acrylic Acid.

4. A chemistry that swells at high pH is PEG-DA + Acrylamide.

Oligomer	Density(g/ml)	Viscosity (mPa.s)	Refractive Index	Surface Tension (mN/m)
PEG-DA (200)	1.122	25	1.4639	41.3
PEG-DA (400)	1.117	56	1.4655	42.6
PEG-DA (700)	1.117	90	1.4676	43.7

Table A.1: *Table listing some key properties of PEG-DA oligomers of different molecular weights*

A.8.3 Importance of the Field Stop Plane

One conjugate focal plane to the sample plane is located in the field stop of the microscope. However, the exact location of this plane is crucial. While the two slider bars with adjustable aperture sizes have been designed to have the aperture exactly at the field stop, it is not the same with the longer slider bar (with 3 holes) that we use for the circular masks. In this case it is essential to a)find the field stop plane by changing where the mask is located or b)make an adjustment for this fact while forming particles by focusing either below or above the center plane of the channel as required.

A.8.4 Spot Size of Microscope Objectives

Upon completely opening the field stop of the Zeiss Axiovert 200, the size of the spot that can be polymerized is 1400 μm with a 20X and 700μm with a 40X. The size of the spot is presumed to be 2.8mm with a 10X and 5.6mm with a 5X.

A.8.5 Making Magnetic Polymer Particles

Flow lithography provides a convenient route to the synthesis of non-spherical magnetic particles. One way to implement this is to add the citrate-coated ferrofluid to an oligomer mix and then cross-link it. Only dilute solutions of ferrofluid-oligomer mix can be made in order to prevent aggregation of the ferrofluid. Once this solution is made, we also observe that there are problems getting particles to flow out of the microfluidic device. I suspect that one of the reasons this may be happening is that the presence of Fe^{+3} ions counteracts the oxygen inhibition effect. There is some evidence to show that iron is able to react with unreactive peroxide species and convert them back to reactive radical species.

A.9 Stop-Flow Lithography

A.9.1 Getting Perfectly Stopped Flow

It is difficult to get a flow that is completely stopped in SFL. The low velocities obtained are typically enough to obtain good resolution. To get as good stoppage as possible, the following must be done:

1. The pipette tip inserted into the inlet should be bent such that the gravitational head is minimal.

2. The reservoir should be large and filled with liquid to avoid surface effects driving the flow

Despite the above precautions, a very small flow is always seen - possibly because of the permeation of oligomer into the PDMS.

A.10 3-d Structures with a Phase Mask

In this section, various tips pertaining to experiments with 3-d structures are described.

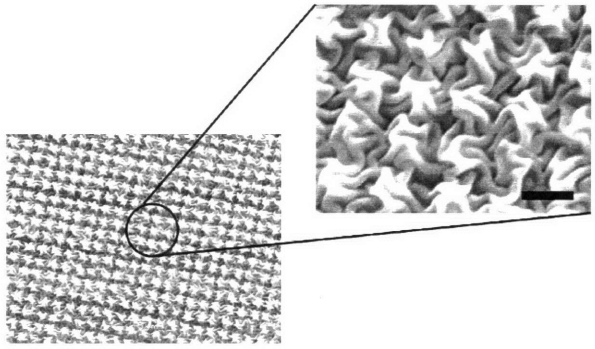

Fig. A.2: *An image showing a shrunk PEG-DA (400) structure developed in ethanol. The inset shows a magnified view of the structure and the scalebar in the inset is 1 μm.*

A.10.1 Using the Microscope

1. Do not use the microscope objectives to make structures. The converging properties of microscope objectives make the light highly uncollimated.

2. When using a collimating tube attached to the microscope, insert the tube into a slot where an objective has been removed. Then stick the mask on top of the tube so that it is in conformal contact with the device. Inserting the mask in the field-stop plane yields no defined structure formation.

3. It is important to have a thin layer of PDMS on top of the phase mask in order to prevent the oligomer from entering the interstitial spaces in the phase mask.

4. We found that 390 nm laser light worked best for the synthesis of 3-d structures.

A.10.2 Shrinking of Structures

Often, when structures were formed using insufficient exposure times, significant shrinkage was seen on developing them. While such structures assume exotic shapes as seen in Figure A.2, these cannot be controlled easily and are typically undesirable.

A.10.3 3-d phase Masks

All the work reported in Chapter 6 was performed with 2-d phase masks. Such masks are easier to model and hence were preferred. Another category of phase masks is 3-d phase masks whose effect is difficult to model. While interesting structures were obtained with such masks, they were not chosen for further studies because of the problems associated with modeling the interference of light through them.

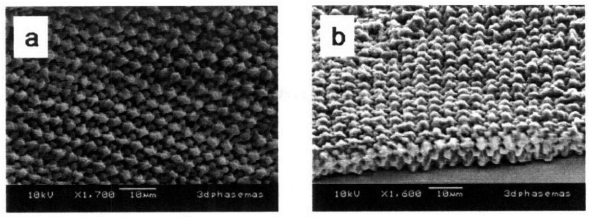

Fig. A.3: *SEM images of structure obtained using a 3-d phase mask. a)Top view of the structure. b)Cross-sectional view of the structure.*

Bibliography

[1] Todd M. Squires and Stephen R. Quake. Microfluidics: Fluid physics at the nanoliter scale. *Reviews of Modern Physics*, 77(3):977, 2005.

[2] Howard A. Stone, Abraham D. Stroock, and Armand Ajdari. Microfluidics. *Annu. Rev. Fluid Mech.*, 36:381–411, 2004.

[3] A. Gunther and K. F. Jensen. Multiphase microfluidics: from flow characteristics to chemical and materials synthesis. *Lab On A Chip*, 6(12):1487–1503, 2006.

[4] Jong Wook Hong and Stephen R Quake. Integrated nanoliter systems. *Nat. Biotech.*, 21(10):1179–1183, 2003.

[5] Dieter Urban and Koichi Takamura, editors. *Polymer Dispersions and Their Industrial Applications*. Wiley-VCH, Weinheim, Germany, 2002.

[6] H. Kawaguchi. Functional polymer microspheres. *Progress In Polymer Science*, 25(8):1171–1210, 2000.

[7] Yu Lu, Yadong Yin, and Younan Xia. Three-dimensional photonic crystals with non-spherical colloids as building blocks. *Adv. Mater.*, 13(6):415–420, 2001.

[8] W.B. Russel, D.A. Saville, and W.R. Schowalter. *Colloidal Dispersions*. Cambridge University Press, 1st edition, 1989.

[9] R. Haghgooie, C. Li, and P.S. Doyle. Experimental study of structure and dynamics in a monolayer of paramagnetic colloids confined by parallel hard walls. *Langmuir*, 22(8):3601–3605, 2006.

[10] S. C. Tsai, D. Botts, and J. Plouff. Effects of particle properties on the rheology of concentrated noncolloidal suspensions. *J. Rheol.*, 36:1291–1305, 1991.

[11] Sharon C. Glotzer, Michael J. Solomon, and N. A. Kotov. Self-assembly: From nanoscale to microscale colloids. *AIChE J.*, 50(12):2978–2985, 2004.

[12] Sharon C. Glotzer. Some assembly required. *Science*, 306:419–420, 2004.

[13] Daniel C. Pregibon, Mehmet Toner, and Patrick S. Doyle. Multifunctional particles for high throughput biomolecule analysis. *Science*, 315:1393, 2007.

[14] Julie A. Champion and Samir Mitragotri. Role of target geometry in phagocytosis. *PNAS*, 103(13):4930–4934, 2006.

[15] M. Okubo, T. Fujibayashi, and A. Terada. Synthesis of micron-sized, monodisperse polymer particles of disc-like and polyhedral shapes by seeded dispersion polymerization. *Colloid. Polym. Sci.*, 283:793–798, 2005.

[16] Jason P. Rolland, Benjamin W. Maynor, Larken E. Euliss, Ansley E. Exner, Ginger M. Denison, and Joseph M. DeSimone. Direct fabrication and harvesting of monodisperse, shape-specific nanobiomaterials. *JACS*, 127:10096–10100, 2005.

[17] Peng Jiang, Jane F. Bertone, and Vicki L. Colvin. A lost-wax approach to monodisperse colloids and their crystals. *Science*, 291:453–457, 2001.

[18] Adeline Perro, Stephane Reculusa, Serge Ravaine, Elodie Bourgeat-Lami, and Etienne Duguet. Design and synthesis of janus micro- and nanoparticles. *J. Mater. Chem.*, 15:3745–3760, 2005.

[19] L. Hong, S. Jiang, and S. Granick. Simple method to produce janus colloidal particles in large quantity. *Langmuir*, 22(23):9495–9499, 2006.

[20] Edwin Snoeks, Alfons von Blaaderen, Teun van Dillen, Carlos M. van Kats, Mark L. Brongersma, and Albert Polman. Collidal ellipsoids with continuously variable shape. *Adv. Mater.*, 12:1511–1514, 2000.

[21] Jeffrey R. Millman, Ketan H. Bhatt, Briang G. Prevo, and Orlin D. Velev. Anisotropic particle synthesis in dielectrophoretically controlled microdroplet reactors. *Nat. Mater.*, 4:98–102, 2005.

[22] Kyung-Ho Roh, David C. Martin, and Jerg Lahann. Biphasic janus particles with nanoscale anisotropy. *Nat. Mater.*, 4:759–763, 2005.

[23] Marcin Fialkowski, Agniezska Bitner, and Bartosz A. Grzybowski. Self-assembly of polymeric microspheres of complex internal structures. *Nat. Mater.*, 4:93–97, 2005.

[24] J.-H. Jang, C.K. Ullal, S.E. Kooi, C.Y. Koh, and E.L. Thomas. Shape control of multivalent 3d colloidal particles via interference lithography. *Nano Letters*, 7(3):647–651, 2007.

[25] A. B. D. Brown, C. G. Smith, and A. R. Rennie. Fabricating colloidal particles with photolithography and their interactions at an air-water interface. *Phys. Rev. E.*, 62:951–960, 2000.

[26] Ned Bowden, Andreas Terfort, Jeff Carbeck, and George M. Whitesides. Self-assembly of mesoscale objects into ordered two-dimensional arrays. *Science*, 276:233–235, 1997.

[27] Jeremy L. Steinbacher and D. Tyler McQuade. Polymer chemistry in flow: New polymers, beads, capsules, and fibers. *J. Polym. Sci., Part A: Polym. Chem.*, 44:6505–6657, 2006.

[28] J. C. McDonald, D. C. Duffy, J. R. Anderson, D. T. Chiu, H. K. Wu, O. J. A. Schueller, and G. M. Whitesides. Fabrication of microfluidic systems in poly(dimethylsiloxane). *Electrophoresis*, 21(1):27–40, 2000.

[29] Todd Thorsen, Richard W. Roberts, Frances H. Arnold, and Stephen R. Quake. Dynamic pattern formation in a vesicle-generating microfluidic device. *Phys. Rev. Lett.*, 86(18):4163–4166, 2001.

[30] F. Caruso and M.and Mohwald H. Lichtenfeld, H.and Giersig. Electrostatic self-assembly of silica nanoparticle-polyelectrolyte multilayers on polystyrene latex particles. *J. Amer. Chem. Soc.*, 120:8523–8524, 1998.

[31] Takasi Nisisako, Toru Torii, and Toshiro Higuchi. Novel microreactors for functional polymer beads. *Chem. Eng. J.*, 101:23–29, 2004.

[32] Gi-Ra Yi, Todd Thorsen, Vinothan N. Manoharan, Moon-Ja Hwang, Seog-Jin Jeon, David J. Pine, Stephen R. Quake, and Seung-Man Yang. Generation of uniform colloidal assemblies in soft microfluidic devices. *Adv. Mater.*, 15(15):1300–1304, 2003.

[33] Wonje Jeong, Jeongyun Kim, Sunjeong Kim, Sanghon Lee, Glennys Mensing, and David J. Beebe. Hydrodynamic microfabrication *via* "on the fly" photopolymerization of microscale fibers and tubes. *Lab Chip*, 4:576–580, 2004.

[34] Dhananjay Dendukuri, Kim Tsoi, T. Alan Hatton, and Patrick S. Doyle. Controlled synthesis of nonspherical microparticles using microfluidics. *Langmuir*, 21:2113–2116, 2005.

[35] Shengqing Xu, Zhihong Nie, Minseok Seo, Patrick Lewis, Eugenia Kumacheva, Howard A. Stone, Piotr Garstecki, Douglas B. Weibel, Irina Gitlin, and George M. Whitesides. Generation of monodisperse particles by using microfluidics: control over size, shape and composition. *Angew. Chem. Int. Ed.*, 44:724–728, 2005.

[36] Zhihong Nie, Shengqing Xu, Minseok Seo, Patrick C. Lewis, and Eugenia Kumacheva. Polymer particles with various shapes and morphologies produced in continuous microfluidic reactors. *J. Am. Chem. Soc.*, 127(22):8058 –8063, 2005.

[37] Anand Bala Subramaniam, Manouk Abkarian, and Howard A. Stone. Controlled assembly of jammed colloidal shells on fluid droplets. *Nat. Mater.*, 4(7):553–556, 2005.

[38] Dhananjay Dendukuri, Daniel C. Pregibon, Jesse Collins, T. Alan Hatton, and Patrick S. Doyle. Controlled synthesis of nonspherical microparticles using microfluidics. *Nat. Mater.*, 5:365–369, 2006.

[39] Takasi Nisisako, Toru Torii, Takanori Takahashi, and Yoichi Takizawa. Synthesis of monodisperse bicolored janus particles with electrical anisotropy using a microfluidic co-flow system. *Adv. Mater.*, 18:1152–1156, 2006.

[40] Mathieu Joanicot and Armand Ajdari. Droplet control for microfluidics. *Science*, 309(5736):887–888, 2005.

[41] T. Kawakatsu, Y. Kikuchi, and M. Nakajima. Regular-sized cell creation in microchannel emulsification by visual microprocessing method. *J. Am. Oil Chem. Soc.*, 74:317–321, 1997.

[42] Shelley L. Anna, Nathalie Bontoux, and Howard A. Stone. Formation of dispersions using "flow focusing" in microchannels. *Appl. Phys. Lett.*, 82(3):364–366, 2003.

[43] B. Zheng, L.S. Roach, and R.F. Ismagilov. Screening of protein crystallization conditions on a microfluidic chip using nanoliter-size droplets. *Journal of the American Chemical Society*, 125(37):11170–11171, 2003.

[44] V. Taly, B. T. Kelly, and A. D. Griffiths. Droplets as microreactors for high-throughput biology. *Chembiochem*, 8(3):263–272, 2007.

[45] Shinji Sugiura, Mitsutoshi Nakajima, Jihong Tong, Hiroshi Nabetani, and Minoru Seki. Preparation of monodispersed solid lipid microspheres using a microchannel emulsification technique. *J. Colloid Interface Sci.*, 227:95–103, 2000.

[46] S. Sugiura, M. Nakajima, and M. Seki. Preparation of monodispersed polymeric microspheres over 50 μm employing microchannel emulsification. *Industrial & Engineering Chemistry Research*. 41(16):4043–4047, 2002.

[47] Takasi Nisisako, Toru Torii, and Toshiro Higuchi. Droplet formation in a microchannel network. *Lab Chip*, 2:24–26, 2002.

[48] J. Christopher Love, Daniel B. Wolfe, Heiko O. Jacobs, and George M. Whitesides. Microscope projection photolithograpy for rapid prototyping of masters with micron-scale features for use in soft lithography. *Langmuir*, 17:6005–6012, 2001.

[49] Dhananjay Dendukuri, T. Alan Hatton, and Patrick S. Doyle. Synthesis and self-assembly of amphiphilic polymeric microparticles. *Langmuir*, 23:4669–4674, 2007.

[50] Garstecki P., Fuerstman M.J., Stone HA, and Whitesides G.M. Formation of droplets and bubbles in a microfluidic t-junction-scaling and mechanism of break-up. *Lab Chip*, 6:437–446, 2006.

[51] J. Bico and D. Quere. Self-propelling slugs. *J. Fluid Mech.*, 467:101–127, 2002.

[52] http://www.norlandprod.com.

[53] Remi Dreyfus, Patrick Tabeling, and Herve Willaime. Ordered and disordered patterns in two-phase flows in microchannels. *Phys. Rev. Lett.*, 90:144505, 2004.

[54] Alexander Rezvin, Ryan J. Russell, Vamsi K. Yadavalli, Won-Gun Koh, Curt Deister, David D. Hile, Michael B. Mellott, and Michael V. Pishko. Fabrication of poly(ethylene glycol) hydrogel microstructures using photolithography. *Langmuir*, 17:5440–5447, 2001.

[55] Christian Decker and Aubrey D. Jenkins. Kinetic approach of O_2 inhibition in ultraviolet- and laser-induced polymerizations. *Macromolecules*, 18:1241–1244, 1985.

[56] M. Zrinyi. Intelligent polymer gels controlled by magnetic fields. *Colloid. Polym. Sci.*, 278:98–103, 2000.

[57] SungRak Kim, HyunJik Oh, Ju Yeol Baek, HyugHan Kim, WooSeung Kim, and SangHoon Lee. Hydrodynamic fabrication of polymeric barcoded strips as components for parallel bioanalysis and programmable microactuation. *Lab Chip*, 5:1168–1172, 2005.

[58] Nancy H. Finkel, Xinhui Lou, Cuiying Wang, and Lin He. Barcoding the microworld. *Anal. Chem.*, 76:352A–359A, 2004.

[59] Greg C. Randall and Patrick S. Doyle. Permeation driven flow in in poly(dimethylsiloxane) microfluidic devices. *P.N.A.S.*, 102(31):10812–10818, 2005.

[60] T.C. Merkel, V.I. Bondar, K. Nagai, B.D. Freeman, and I. Pinnau. Gas sorption, diffusion, and permeation in poly(dimethylsiloxane). *J. Polym. Sci. B*, 38:415–434, 2000.

[61] Eugene Hecht and Alfred Zajac. *Optics*. Addison Wesley Publishing Company, New York, USA, 1997.

[62] Michael B. Mellott, Katherine Searcy, and Micheal V. Pishko. Release of protein from highly cross-linked hydrogels of poly(ethyleneglycol) diacrylate fabricated by uv polymerization. *Biomaterials*, 22:929–941, 2000.

[63] Ewa Andrzejewska. Photopolymerization kinetics of multifunctional monomers. *Prog. Polym. Sci.*, 26:605–665, 2001.

[64] T. Randolph, K. Anseth, J. L. Owens, and C. Lengsfeld. Preparation and use of photopolymerized microparticles. *US Patent*, 6864301, 2005.

[65] C. K. Ullal, M. Maldovan, E. L. Thomas, G. Chen, Y.-J. Han, and S Yang. Photonic crystals through holographic lithography: Simple cubic, diamond-like, and gyroid-like structures. *Appl. Phys. Lett.*, 84:5434–5436, 2004.

[66] Jacob N. Israelachvili. *Intermolecular and Surface Forces*. Academic Press, Orlando, Florida 32887, 1st edition, 1985.

[67] J. Atencia and D. J. Beebe. Controlled microfluidic interfaces. *Nature*, 437:648–655, 2005.

[68] Mariana Surmeian, Maxim N. Slyadnev, Hideaki Hisamoto, Akihide Hibara, Kenji Uchiyama, and Takehiko Kitamori. Three-layer flow membrane system on a microchip for investigation of molecular transport. *Anal. Chem.*, 74:2014 -2020, 2002.

[69] L. Dong, A.K. Agarwal, D.J. Beebe, and H. Jiang. Adaptive liquid microlenses activated by stimuli-responsive hydrogels. *Nature*, 442:551–554, 2006.

[70] Bin Zhao, Neil O. L. Viernes, Jeffrey S. Moore, and David J. Beebe. Control and applications of immiscible liquids in microchannels. *Anal. Chem.*, 124:5284–5285, 2002.

[71] R. Jenks G. Zabow, F. Assi and M. Prentiss. Guided microfluidics by electromagnetic capillary focusing. *Appl. Phys. Lett.*, 80:1483–1485, 2002.

[72] W. Engl, K. Ohata, P. Guillot, A. Colin, and P. Panizza. Selection of two-phase flow patterns at a simple junction in microfluidic devices. *Phys. Rev. Lett.*, 96:134505, 2006.

[73] Pierre Guillot and Annie Colin. Stability of parallel flows in a microchannel after a t-junction. *Phys. Rev. E.*, 72:066301, 2005.

[74] Michael B. Mellott, Katherine Searcy, and Micheal V. Pishko. Release of protein from highly cross-linked hydrogels of poly(ethyleneglycol) diacrylate fabricated by uv polymerization. *Biomaterials*, 22:929–941, 2001.

[75] Bin Zhao, Jeffrey S. Moore, and David J. Beebe. Surface-directed liquid flow inside microchannels. *Science*, 291:1023–1026, 2001.

[76] Ajit Jillavenkatesa, Stanley J. Dapkunas, and Lin-Sien H. Lum. Particle size characterization. Technical Report 960, NIST, 2001. According to the standards of the National Institute of Standards and Technology (NIST), a particle distribution can be considered monodisperse if at least 90% of the distribution lies within 5% of the median size.

[77] C. Casagrande, P. Fabre, E. Raphael, and M. Veyssie. Janus beads: Realization and behaviour at water/oil interfaces. *Europhys. Lett.* 9:251–255, 1989.

[78] Bernard P. Binks. Particles as surfactants-similarities and differences. *Curr. Opin. Coll. Int. Sci.*, 7:21–41, 2002.

[79] Ravi S. Kane, Shuichi Takayama, Emanuele Ostuni, Donald E. Ingber, and George M. Whitesides. Patterning proteins and cells using soft lithography. *Biomaterials*, 20(23-24), 1999.

[80] Ali Khademhosseini, Robert Langer, Jeffrey Borenstein, and Joseph P. Vacanti. Tissue engineering special feature: Microscale technologies for tissue engineering and biology. *PNAS*. 103(8):2480–2487, 2006.

[81] Fabrizio Gelain, Daniele Bottai, Angleo Vescovi, and Shuguang Zhang. Designer self-assembling peptide nanofiber scaffolds for adult mouse neural stem cell 3-dimensional cultures. *PLoS ONE*, 1(1): e119. doi:10.1371/journal.pone.0000119, 2006.

[82] Christopher J. Bettinger, Eli J. Weinberg, Katherine M. Kulig, Joseph P. Vacanti, Yadong Wang, Jeffrey T. Borenstein, and Robert Langer. Three-dimensional microfluidic tissue-engineering scaffolds using a flexible biodegradable polymer. *Adv. Mater.*, 18:169–174, 2006.

[83] Dimitri A. Parthenopoulos and Peter M. Rentzepis. Three-dimensional optical storage memory. *Science*, 245(4920):843–845, 1989.

[84] J.A. Burdick, A. Khademhosseini, and R. Langer. Fabrication of gradient hydrogels using a microfluidics photopolymerization process. *Langmuir*, 20(13):5153–5156, 2004.

[85] Edwin L. Thomas, David B. Alward, David J. Kinning, David C. Martin, Dale L. Handlin, and Lewis J. Fetters. Ordered bicontinuous double-diamond structure of star block copolymers: a new equilibrium microdomain morphology. *Macromolecules*, 19(8):2197–2202, 1986.

[86] Shuguang Zhang. Fabrication of novel biomaterials through molecular self-assembly. *PNAS*, 21:1171–1178, 2003.

[87] A. D. Dinsmore, A. G. Yodh, and D. J. Pine. Phase diagrams of nearly-hard-sphere binary colloids. *Phys. Rev. E*, 52(4):4045–4057, 1995.

[88] Chihchen Chen, Danny Hirdes, and Albert Folch. Gray-scale photolithography using microfluidic photomasks. *PNAS*, 100:1499–1504, 2003.

[89] Gregory M. Gratson, Mingjie Xu, and Jennifer A. Lewis. Direct writing of three-dimensional webs. *Nature*, 428:386–386, 2004.

[90] Yuk Kee Cheung, Brian M. Gillette, Ming Zhong, Sharmilee Ramcharan, and Samuel K. Sia. Direct patterning of composite biocompatible microstructures using microfluidics. *Lab Chip*, 7:574–579, 2007.

[91] S. Kawata, H.-B. Sun, T. Tanaka, and K Takada. Finer features for functional microdevices. *Nature*, 412:697–698, 2001.

[92] Seokwoo Jeon, Jang-Ung Park, Ray Cirelli, Shu Yang, Carla E. Heitzman, Paul V. Braun, Paul J. A. Kenis, and John A. Rogers. Fabricating complex three-dimensional nanostructures with high-resolution conformable phase masks. *PNAS*, 101(34):12428–12433, 2004.

[93] J.-H. Jang, C.K. Ullal, T. Gorishnyy, V.V. Tsukruk, and E.L. Thomas. Mechanically tunable three-dimensional elastomeric network/air structures via interference lithography. *Nano Letters*, 6(4):740–743, 2006.

[94] Dhananjay Dendukuri, Shelley S.Gu, Daniel C. Pregibon, T. Alan Hatton, and Patrick S. Doyle. Stop flow lithography in a microfluidic device. *Lab Chip*, 2007.

[95] David J. Beebe, Jeffrey S. Moore, Joseph M. Bauer, Qing Yu, Robin H. Liu, Chelladurai Devadoss, and Byung-Ho Jo. Functional hydrogel structures for autonomous flow control inside microfluidic channels. *Nature*, 404:588–590, 2000.

[96] S. Yang, J. Ford, C. Ruengruglikit, Q. R. Huang, and J. Aizenberg. Synthesis of photoacid crosslinkable hydrogels for the fabrication of soft, biomimetic microlens arrays. *J. Materials Chem.*, 15(39):4200–4202, 2005.

[97] J.-H. Jang, C.K. Ullal, S.E. Kooi, C.Y. Koh, and E.L. Thomas. Shape control of multivalent 3d colloidal particles via interference lithography. *Nano Letters*, 7(3):647–651, 2007.

[98] Robert Langer and David A. Tirrell. Designing materials for biology and medicine. *Nature*, 428:487–492, 2004.

[99] K. Nakagawa, M. Taguchi, and T. Ema. Fabrication of 64m dram with i-line phase-shift lithography. *IEDM Tech. Dig.*, 1990:817–820.

[100] M.A. Unger, H.P. Chou, T. Thorsen, Scherer A., and Quake S.R. Monolithic microfabricated valves and pumps by multilayer soft lithography. *Science*, 288:113–116, 2000.

[101] A.Y. Fu, H.P. Chou, C. Spence, F.H. Arnold, and Quake S.R. An integrated microfabricated cell sorter. *Anal. Chem.*, 74:2451–2457, 2002.

[102] Kazuo Hosokawa, Kotaro Hanada, and Ryutaro Maeda. A polydimethylsiloxane (pdms) deformable diffraction grating for monitoring local pressure in microfluidic devices. *J. Micromech. Microeng.*, 12:1–6, 2002.

[103] E. Delamarche, H. Schmid, B. Michel, and H. Biebuyck. Stability of molded pdms structures. *Adv. Mater.*, 9:741–746, 1997.

[104] Thomas Gervais, Jamil El-Ali, Axel Gunther, and Klavs F. Jensen. Flow-induced deformation of shallow microfluidic channels. *Lab Chip*, 6:500–507, 2006.

[105] Thomas Gervais. *Mass Transfer and Structural Analysis of Microfluidic Sensors*. PhD thesis, Massachusetts Institute of Technology, 2005.

[106] J. Skotheim and L. Mahadevan. Soft lubrication. *Phys. Rev. Lett.*, 92:245509, 2004.

[107] C. Fütterer, N. Minc, V. Bormuth, J.-H. Codarbox, P. Laval, J. Rossier, and J.-L. Viovy. Injection and flow control system for microchannels. *Lab Chip*, 4:351, 2004.

[108] C.J. Hernandez and T.G. Mason. Colloidal alphabet soup: Monodisperse dispersions of shape-designed lithoparticles. *Journal of Physical Chemistry C*, 111(12):4477–4480, 2007.

[109] Young S. Lee, Eric D. Wetzel, and Norman J. Wagner. The ballistic impact characteristics of kevlar woven fabrics impregnated with a colloidal shear thickening fluid. *J. Mat. Sci.*, 38:2825–2833, 2003.

[110] R.F. Ismagilov, A.D. Stroock, P.J.A. Kenis, G.Whitesides, and H.A.Stone. Experimental and theoretical scaling laws for transverse diffusive broadening in two-phase laminar flows in microchannels. *Appl. Phys. Lett.*, 76:2376–2378, 2000.

[111] Jelica Strauch, James McDonald, Bogdan E. Chapman, Philip W. Kuchel, Brian S. Hawkett, G. Evan Roberts, Matthew P. Tonge, and Robert G. Gilbert 1. Diffusion coefficients of the monomer and oligomers in hydroxyethyl methacrylate. *J. Polym. Sci., Part A: Polym. Chem.*, 41:2491–2501, 2003.

[112] C. Decker. The use of UV irradiation in polymerization. *Polymer Int.*, 45(2):133–141, 1998.

[113] Jean-Pierre Fouassier. *Photoinitiation, Photopolymerization, and Photocuring: Fundamentals and Applications*. Hanser Gardner Pubns, July 1995.

[114] Ying Cai and Julie L.P. Jessop. In *Mark's Encyclopedia of Polymer Science and Technology*, volume 10, chapter Photopolymerization,Free Radical, pages 807–837. John Wiley & Sons, Inc, 2003.

[115] Masud Mansuripur. Projection photolithography. *Optics and Photonics News*, 11:36–40, 2000.

[116] KT Nguyen and JL West. Photopolymerizable hydrogels for tissue engineering applications. *Biomaterials*, 23.

[117] Allison K. O'Brien and Christopher N. Bowman. Impact of oxygen on photopolymerization kinetics and polymer structure. *Macromolecules*, 39(7):2501–2506, 2006.

[118] Allison K. O'Brien and Christopher N. Bowman. Modeling the effect of oxygen on photopolymerization kinetics. *Macromol. Theory Simul.*, 15:176–182, 2006.

[119] Joao T. Cabral and Jack F. Douglas. Propagating waves of network formation induced by light. *Polymer*, 46:4230–4241, 2005.

[120] J.T. Cabral, S.D. Hudson, C. Harrison, and J.F. Douglas. Frontal photopolymerization for microfluidic applications. *Langmuir*, 20(23):10020–10029, 2004.

[121] Seda Kizilel, Vctor H. Prez-Luna, and Fouad Teymour. Mathematical model for surface-initiated photopolymerization of poly(ethylene glycol) diacrylate. *Macromol. Theory Simul.*, 15:686–700, 2006.

[122] Michael D. Goodner and Christopher N. Bowman. Development of a comprehensive free radical photopolymerization model incorporating heat and mass transfer effects in thick films. *Chem. Eng. Sci.*, 57, 2002.

[123] H. Lin and B.D. Freeman. Gas permeation and diffusion in cross-linked poly(ethylene glycol diacrylate). *Macromolecules*, 39(10):3568–3580, 2006.

[124] L Lecamp, P. Lebaudy, B. Youssef, and C. Bunel. Influence of uv radiation wavelength on conversion and temperature distribution profiles within dimethacrylate thick material during photopolymerization. *Polymer*, 42:8541–8547, 2001.

[125] M. Seo, Zhihong Nie, Shengqing Xu, Michelle Mok, Patrick C. Lewis, Robert Graham, and Eugenia Kumacheva. Continuous microfluidic reactors for polymer particles. *Langmuir*, 21(25):11614–11622, 2005.

[126] H. J. van der Linden, S. Herber, W. Olthuis, and P. Bergveld. Stimulus-sensitive hydrogels and their applications in chemical (micro)analysis. *Analyst*, 128(4):325–331, 2003.

[127] S. K. Yoon, M. Mitchell, E. R. Choban, and P. J. A. Kenis. Gravity-induced reorientation of the interface between two liquids of different densities flowing laminarly through a microchannel. *Lab On A Chip*, 5(11):1259–1263, 2005.

[128] D. Needham and E. Evans. Structure and mechanical properties of giant lipid (dmpc) vesicle bilayers from 20 degrees c below to 10 degrees c above the liquid crystal-crystalline phase transition at 24 degrees c. *Biochemistry*, 27:8261–8269, 1988.

[129] W. Rawicz, K. C. Olbrich, T. McIntosh, D. Needham, and E. Evans. Effect of chain length and unsaturation on elasticity of lipid bilayers. *Biophys. J.*, 79(1):328–339, 2000.

[130] Alexander Moscho, Owe Orwar, Daniel T. Chiu, Biren P. Modi, and Richard N. Zare. Rapid preparation of giant unilamellarvesicles. *PNAS*, 93(21):11443–11447, 1996.

[131] K Akashi, H Miyata, H Itoh, and Jr Kinosita, K. Preparation of giant liposomes in physiological conditions and their characterization under an optical microscope. *Biophys. J.*, 71(6):3242–3250, 1996.